Fibrillar Aβ triggers microglial proteome alterations and dysfunction in Alzheimer mouse models

Laura Sebastian Monasor[1,10]*, Stephan A. Müller[1]*, Alessio Colombo[1], Jasmin König[1,2], Stefan Roth[3], Arthur Liesz[3,4], Anna Berghofer[5], Takashi Saito[6,7], Takaomi C. Saido[6], Jochen Herms[1,4,8], Michael Willem[9], Christian Haass[1,4,9], Stefan F. Lichtenthaler[1,4,5#] & Sabina Tahirovic[1#]

[1] German Center for Neurodegenerative Diseases (DZNE) Munich, 81377 Munich, Germany

[2] Faculty of Chemistry, Technical University of Munich, Garching, Germany

[3] Institute for Stroke and Dementia Research (ISD), Ludwig-Maximilians Universität München, 81377 Munich, Germany

[4] Munich Cluster for Systems Neurology (SyNergy), Munich, Germany

[5] Neuroproteomics, School of Medicine, Klinikum Rechts der Isar, Technical University of Munich, Munich, Germany

[6] Laboratory for Proteolytic Neuroscience, RIKEN Center for Brain Science Institute, Wako, Saitama 351-0198, Japan

[7] Department of Neurocognitive Science, Nagoya City University Graduate School of Medical Science, Nagoya, Aichi 467-8601, Japan

[8] Center for Neuropathology and Prion Research, Ludwig-Maximilians-Universität München, 81377 Munich, Germany

[9] Biomedical Center (BMC), Ludwig-Maximilians Universität München, 81377 Munich, Germany

[10] Graduate School of Systemic Neuroscience, Ludwig-Maximilians-University Munich, Munich, Germany.

*Contributed equally

#Correspondence: Sabina.Tahirovic@dzne.de and Stefan.Lichtenthaler@dzne.de

Running title:

Microglial proteomic signatures of AD

Keywords: Alzheimer's disease / microglia / proteomic signatures / neuroinflammation / phagocytosis

Abstract

Microglial dysfunction is a key pathological feature of Alzheimer´s disease (AD), but little is known about proteome-wide changes in microglia during the course of AD pathogenesis and their functional consequences. Here, we performed an in-depth and time-resolved proteomic characterization of microglia in two mouse models of amyloid β (Aβ) pathology, the overexpression APPPS1 and the knock-in APP-NL-G-F (APP-KI) model. We identified a large panel of Microglial Aβ Response Proteins (MARPs) that reflect a heterogeneity of microglial alterations during early, middle and advanced stages of Aβ deposition. Although both mouse models display severe microglial alterations at late stages of amyloid pathology, MARP signatures occur earlier in the APPPS1 mice. Strikingly, the kinetic differences in proteomic profiles correlated with the presence of fibrillar Aβ, rather than dystrophic neurites, suggesting that fibrillar Aβ aggregates are the main drivers of the AD-associated microglial phenotype and the observed functional decline. The identified microglial proteomic fingerprints of AD provide a valuable resource for functional studies of novel molecular targets and potential biomarkers for monitoring AD progression or therapeutic efficacy.

Introduction

Microglia play fundamental roles in a variety of neurodegenerative diseases, including AD (McQuade and Blurton-Jones, 2019). Changes in brain immunity, together with extracellular Aβ deposition and neurofibrillary tangles, are major pathological culprits in AD (Gjoneska et al., 2015; Guillot-Sestier and Town, 2013; Holtzman et al., 2011; Shi and Holtzman, 2018). The importance of microglia in AD pathogenesis is well illustrated by the increasing number of identified AD risk genes which are expressed in microglia and have functions in brain immunity (Cuyvers and Sleegers, 2016; Guerreiro et al., 2013; Jansen et al., 2019; Jonsson et al., 2013; Karch and Goate, 2015; Lambert et al., 2009; Naj et al., 2011; Sims et al., 2017). For example, the triggering receptor expressed on myeloid cells 2 (*Trem2*) and apolipoprotein E (*ApoE*) are major genetic risk factors for sporadic AD that are expressed by plaque-associated microglia and involved in Aβ clearance (Bradshaw et al., 2013; Castellano et al., 2011; Kleinberger et al., 2014; Parhizkar et al., 2019; Reddy et al., 2009; Wang et al., 2015). It has also been shown that microglial phagocytosis decays over the course of AD (Hickman et al., 2008; Koellhoffer et al., 2017; Orre et al., 2014a; Solito and Sastre, 2012; Zuroff et al., 2017). Along these lines, Aβ clearance was found reduced in sporadic AD and it is assumed to be a key factor in the pathogenesis (Mawuenyega et al., 2010; Saido, 1998; Wildsmith et al., 2013). Importantly, Aβ clearance defects in AD microglia are reversible (Daria et al., 2017) and enhancing microglial phagocytic function has been explored as a therapeutic approach since substantial reduction of Aβ burden appears to correlate with cognitive benefits (Bacskai et al., 2001; Bard et al., 2000; Bohrmann et al., 2012; Janus et al., 2000; Lathuiliere et al., 2016; Morgan et al., 2000; Nicoll et al., 2006; Nicoll et al., 2003; Schenk et al., 1999; Schilling et al., 2018; Sevigny et al., 2016; Wilcock et al., 2004). However, when and how microglia change along AD progression is still not clear. Thus, understanding molecular alterations of microglia at different stages of AD is crucial and a pre-requisite for developing safe and efficacious therapy.

Transcriptional expression profiles for microglia were previously revealed under physiological, neurodegenerative or neuroinflammatory conditions (Butovsky et al., 2014; Galatro et al., 2017; Gosselin et al., 2017; Gotzl et al., 2019; Grabert et al., 2016; Holtman et al., 2015; Kamphuis et al., 2016; Krasemann et al., 2017; Mazaheri et al., 2017; Orre et al., 2014a; Orre et al., 2014b; Wang et al., 2015; Yin et al., 2017). Transcriptional signatures were also recently reported at single-cell resolution, demonstrating regional and functional heterogeneity of brain myeloid cells (Hammond et al., 2019; Jordao et al., 2019; Keren-Shaul et al., 2017; Mathys et al., 2017; Sala Frigerio et al., 2019). In neurodegenerative mouse models, two major profiles have been proposed along the spectrum of

microglial alterations. One is the homeostatic microglial signature that occurs under physiological conditions and is characterized by the expression of several genes, including *P2ry12*, *Tmem119* and *Cx3cr1*. The other key signatures, referred to as disease-associated microglia (DAM), microglial neurodegenerative phenotype (MGnD) or activated response microglia (ARM) are observed under neurodegenerative conditions (Keren-Shaul et al., 2017; Krasemann et al., 2017; Sala Frigerio et al., 2019) and characterized by increased expression of *ApoE*, *Trem2*, *Cd68*, *Clec7a* and *Itgax* (*Cd11c)*, among others. These changes were quantified using RNA transcripts, but transcript levels do not necessarily reflect protein levels which ultimately control cell function (Bottcher et al., 2019; Mrdjen et al., 2018; Sharma et al., 2015). Importantly, a recent study postulated that transcriptomic profiles of microglia from another AD mouse model (5xFAD) do not correlate well with proteomic changes (Rangaraju et al., 2018), suggesting the existence of additional translational or post-translational regulation mechanisms in AD microglia. Additionally, little is known about Aβ-associated changes in the microglial proteome in a time-resolved manner, or which proteome alterations underscore microglial dysfunction. Accordingly, we analyzed the microglial proteome at distinct stages of Aβ pathology in two commonly used mouse models of amyloidosis; the APPPS1 (Radde et al., 2006), and the APP-KI mice (Saito et al., 2014). In contrast to the APPPS1 mouse model that overexpresses mutated human amyloid precursor protein (APP) and presenilin-1 (PS1), the APP-KI model bears endogenous levels of APP with a humanized Aβ sequence containing three AD mutations (NL-G-F), and has no alterations of PS1 (Radde et al., 2006; Saito et al., 2014).

Our study determines the proteome of microglia from APPPS1 and APP-KI mice in a time resolved manner, starting from pre-deposition to early, middle and advanced stages of amyloid deposition and reveals a panel of MARPs that progressively change throughout Aβ accumulation. Although both mouse models display severe microglial alterations at late stages of Aβ pathology, the occurrence of MARP signatures differs and appears earlier in the APPPS1 mice. Strikingly, the kinetic differences in proteomic profiles correlated with the presence of fibrillar Aβ, rather than dystrophic neurites, suggesting that fibrillar Aβ aggregates are the main drivers of the AD-associated microglial phenotype and corresponding functional decline. The time-resolved microglial profiles may serve as benchmark proteomic signatures for investigating novel microglial targets or monitoring the efficacy of future pre-clinical studies aiming at microglial repair.

Results

APPPS1 microglia develop an AD-associated proteomic signatures earlier compared to the APP-KI microglia

To facilitate proteomic analysis, we first optimized the microglial isolation procedure. CD11b positive microglia were isolated from mouse cerebrum using MACS technology. The purity of the CD11b-enriched fraction was controlled by fluorescence activated cell sorting (FACS), revealing that a 97% of isolated cells were CD11b positive (Suppl. Fig 1A). Of note, only 0.49% of CD11b positive cells were detected in the CD11b-depleted fraction (Suppl. Fig 1B), demonstrating high isolation efficiency. Next, we optimized the data acquisition method for microglial proteome analysis (Suppl. Fig 2A; Suppl. Table 1). Recently, it was shown that Data Independent Acquisition (DIA) for label-free quantification (LFQ) of proteins identifies and quantifies consistently more peptides and proteins across multiple samples, compared to Data Dependent Acquisition (DDA) (Bruderer et al., 2015). Thus, we first evaluated the performance of DDA *vs.* DIA (Suppl. Table 2) using microglial lysates from WT and APPPS1 mice. DDA identified 53912 peptides on average compared to 74281 peptides identified by DIA, representing a 37.8% increase in detection by DIA method (Suppl. Table 2). Overall, the main advantage of DIA was the improved consistency of protein quantifications among the replicates and the identification of proteins with lower abundance, leading to 29% increase of relatively quantified proteins from 4412 with DDA to 5699 with DIA (Suppl. Table 2; Suppl. Fig 2B and C). We therefore selected DIA for further proteomic characterization of APPPS1 and APP-KI microglia. Notably, we also detected a consistent relative quantification of proteins with an overlap of 93.5% between the two mouse models (Suppl. Fig 2D), supporting our selection of DIA as a robust method for microglial proteomic analysis.

Amyloid plaque deposits appear at similar ages (between 6-8 weeks) in APPPS1 and APP-KI mouse models (Radde et al., 2006; Saito et al., 2014). To reveal the dynamics of microglial proteomic alterations across different amyloid stages, we analyzed microglia from 1, 3, 6 and 12 month old APPPS1 and APP-KI mice and their corresponding age-matched wild-type (WT) mice (Suppl. Fig 2A). For our proteomic analysis, we have set as a threshold a log2 fold change larger than 0.5 or smaller than -0.5 compared to the WT with a p-value less than 0.05, and significance after False Discovery Rate (FDR) correction. No data imputation was performed.

According to Aβ burden in both mouse models, we refer to one month of age as a pre-deposition stage, and to 3, 6 and 12 months of age as early, middle and advanced stages of amyloid pathology, respectively (Suppl. Fig 3). At the pre-deposition stage (1 month), microglial proteomes

of APPPS1 and APP-KI mice did not show significant alterations compared to WT (Fig 1A and B), demonstrating that microglia are not affected prior to development of Aβ pathology. At 3 months of age, microglia in APPPS1 mice already displayed a significant up-regulation of 332 proteins and down-regulation of 678 proteins, compared to WT microglia (Fig 1C; Suppl. Table 3A). In contrast, APP-KI microglia were hardly affected at 3 months of age (Fig 1D; Suppl. Table 3B), which is particularly surprising because both mouse models show comparable amyloid burden at this stage (Suppl. Fig 3). At 6 months of age, microglia in APPPS1 mice displayed 309 up-regulated and 261 down-regulated proteins, compared to WT microglia (Fig 1E; Suppl. Table 3A). In contrast to 3 months of age (Fig 1D), APP-KI mice at 6 months of age displayed a substantial alteration of their microglial proteome, illustrated by 140 up-regulated and 151 down-regulated proteins (Fig 1F; Suppl. Table 3B). Still, microglial alterations in 6 month old APP-KI mice were less pronounced compared to the proteome of APPPS1 mice (Fig 1E and F). Noteworthy, by 12 months of age, APPPS1 microglia revealed a significant up-regulation of 776 proteins and down-regulation of 633 proteins, while APP-KI microglia displayed 704 up-regulated and 666 down-regulated proteins (Fig 1G and H; Suppl. Table 3A and B). This indicates comparable changes in APPPS1 and APP-KI mice at advanced stages of Aβ pathology. Overall, our data show that amyloid plaque accumulation triggers microglial progression towards an AD-associated phenotype in both mouse models, but that response dynamics are different in APPPS1 and APP-KI microglia.

Identification of MARPs as signatures of early, middle and advanced amyloid stages

Next, we determined protein alterations that first appear in early, middle or advanced stages of Aβ deposition and remain altered thought all analyzed stages, thus following amyloid accumulation. To this end, we selected the APPPS1 mouse model as a reference since it displays earlier changes and thus provides a better time resolution of protein alterations to amyloid response, compared to the APP-KI model (Fig 2A). Correspondingly, we defined early (proteins changed at 3, 6, and 12 months), middle (proteins changed only at 6 and 12 months) and advanced (proteins changed only at 12 months) MARPs. Only proteins with a consistent quantification in all samples of an age group were used for relative quantification. Furthermore, in order to determine robust and model-independent Aβ-triggered microglial alterations, we only selected MARPs that were altered with a significantly changed abundance in both mouse models (even if in APP-KI microglia changes appear later). This analysis identified 90 early, 176 middle, and 435 advanced MARPs (Suppl. Fig 4A). The most strongly regulated MARPs with early, middle and advanced response are displayed in corresponding

heatmaps (Fig 2B-D). In addition, we compared MARP signatures with the previously delineated RNA signatures of 5xFAD mice (Keren-Shaul et al., 2017) to visualize the overlap, as well as differences, between proteomic and transcriptomic microglial profiles.

Early MARPs included several of the previously identified transcriptional DAM markers (Keren-Shaul et al., 2017) such as ITGAX (CD11c), APOE, CLEC7a, LGALS3 (Galectin-3) and CD68, which were found with an increased abundance (Fig 2B). Moreover, proteins involved in antigen presentation such as CD74, H2-D1, TAP2, TAPBP and H2-K1 were revealed as up-regulated early MARPs. In addition, we discovered prominent changes in interferon signaling represented by the up-regulation of early MARPs, including MNDA, OAS1A, IFIT3, ISG15, GVIN1, STAT1 and 2 (Fig 2B). Even though early MARPs were mainly up-regulated, we also identified early MARPs with a decreased abundance, including KRAS, a protein involved in cell proliferation and the endocytosis regulator EHD2 among others (Fig 2B). A gene ontology (GO) cluster enrichment analysis of early MARPs revealed that up-regulated proteins were enriched for immune and viral response, interferon beta and cytokine response, antigen processing and presentation as well as biotic and lipid response (Fig 3A; Suppl. Fig 5A und D). Thus, these processes represent first molecular alterations that progressively follow Aβ plaque pathology.

The middle MARPs included the up-regulated proteins FABP3, FABP5, CD63, TREM2, MIF and GUSB (Fig 2C), demonstrating a progressive conversion of the microglial proteome towards a disease state that accompanies Aβ accumulation. Importantly, middle MARPs also reveal down-regulation of the proposed homeostatic markers such as CX3CR1, TMEM119 and P2RY12 (Fig 2C). Among the down-regulated middle MARPs, we identified additional chemotaxis and cell migration related proteins like SYK, FER, CX3CL1, and BIN2 (Fig 2C; Suppl. Table 4), underscoring a loss of key homeostatic functions of microglia throughout AD progression.

Advanced MARPs represent proteins that were only altered upon extensive amyloid pathology and show a high correlation between the two models (Suppl. Fig 4B). This group included up-regulation of proteins involved in calcium ion binding such as NCAN, MYO5A, HPCAL4, TTYH1 and GCA and down-regulation of proteins that play a role in the endocytosis/lysosomal system such as TFEB, TFE3 and BIN1 (Fig 2D; Suppl. Table 4). In addition, different G protein-coupled receptor signaling proteins, including GNG2, GNG5 and GNG10, also displayed a decreased abundance (Fig 2D).

A GO cluster enrichment analysis of middle and advanced MARPs identified down-regulation of biological processes including cell motility, migration and chemotaxis, as well as cell development

and proliferation (Fig 3B and C; Suppl. Fig 5B, C, E and F). Conversely, we found an up-regulation of protein glycosylation and carbohydrate metabolism (Fig 3C; Suppl. Fig 5E and F). Additionally, alterations in ion transport processes involving ion homeostasis and pH regulation were also detected (Fig 3C). These findings indicate that after an initial inflammatory response, several cellular processes related to chemotaxis and phagocytosis are progressively dysregulated upon increased Aβ deposition.

Importantly, our proteomic analysis also detected alterations in proteins related to different genetic risk factors of AD (Karch and Goate, 2015), including significantly increased levels of APOE, TREM2, and INPP5D, and decreased levels of PLCG2, ABI3, and BIN1 in both mouse models (Suppl. Table 5A and B).

The overlap of consistently quantified proteins and a previously published transcriptome study (Keren-Shaul et al., 2017) was 38.4%, whereas 2152 and 2841 gene products were only quantified on protein and transcript level, respectively (Suppl. Fig 4C). Single cell transcriptomics (Keren-Shaul et al., 2017) has demonstrated a similar regulation of a number of early MARPs while we found less overlap for middle and advanced MARPs (Fig 2B-D). We also identified proteins with an inverse regulation compared to transcriptomic signatures such as the early MARP RPL38, middle MARPs MCM3 and GFPT1 or advanced MARPs CDC88A, GALNT2, EIF4B and CHMP6 (Fig 2B-D; Suppl. Table 4). Furthermore, the advanced MARP HEXB showed a consistent up-regulation in our proteomic analysis, despite being previously anticipated as a homeostatic gene (Suppl. Table 4).

Overall, our study presents a robust and reliable method to track microglial proteome and provides a resource that maps changes in brain immunity during different phases of Aβ accumulation.

Proteomic changes are detected in plaque-associated microglia

Next, we validated proteomic changes by western blot analysis using isolated microglia from 12 month old APPPS1 and APP-KI mice. This analysis confirmed the pronounced increase of the early MARPs APOE and CD68, the middle MARPs TREM2 and FABP5, as well as reduced levels of the middle MARP CSF1R (Suppl. Fig 4D) in both transgenic mouse models compared to WT mice. Furthermore, proteomic changes were also validated by immunohistochemistry in order to visualize spatial distribution of altered microglial proteins in APPPS1 and APP-KI mice. Immunohistological analysis of 3 month old APPPS1 mice already revealed increased immunoreactivity of selected MARPs such as CLEC7a (Fig 4), TREM2 (Suppl. Fig 6) and APOE (Suppl. Fig 7) that mark initial stages of microglial activation in AD. This increase was detected in IBA1 positive microglia that were clustering around amyloid plaques, but not in microglia further away from plaques and was – in

agreement with our proteomic data – less pronounced in 3 month old APP-KI mice. Accordingly, at 12 months, both APPPS1 and APP-KI mice showed a similar increase in the levels of selected MARPs such as CLEC7a (Fig 5) and decreased levels of TMEM119 (Fig 6) compared to the WT mice, once again in microglia surrounding amyloid plaques. Taken together, we validated selected microglial proteomic alterations from our dataset by applying biochemical and immunohistochemical methods. In addition, we confirmed the kinetic differences in AD-associated proteomic signatures of APPPS1 and APP-KI microglia. Our data suggest that interaction between microglia and Aβ is likely triggering the proteomic changes as they could be observed in plaque-associated microglial population.

APPPS1 and APP-KI mice show similar dynamics of amyloid plaque deposition, but differ in plaque fibrillization

The magnitude of proteomic microglial changes was found to correlate with Aβ plaque accumulation throughout disease progression. However, the appearance of MARP signatures differed between the models and occurred earlier in the APPPS1 mice (Fig 1C and D; Fig 2A) despite the comparable plaque load observed in both mouse models (Suppl. Fig 3). Thus, it appears possible that the nature of amyloid plaques is different between the APPPS1 and APP-KI mice. To examine this, we analyzed amyloid plaques in 3, 6 and 12 month old APPPS1 and APP-KI mice by immunohistochemistry. We used the anti-Aβ antibody NAB228 (Abner et al., 2018) to detect amyloid plaques, and Thiazine red to visualize fibrillar amyloid plaque cores (Daria et al., 2017) (Fig 7A). In agreement with amyloid plaque pathology reported in this model (Radde et al., 2006), APPPS1 mice contained fibrillar amyloid plaque cores already at 3 months of age. In contrast, fibrillar Aβ was barely detectable in APP-KI mice at 3 months of age (Fig 7A). The amount of fibrillar Aβ in APP-KI mice increased at 6 and 12 months, but overall still remained lower compared to the APPPS1 mice. This result was also confirmed by biochemical analysis in which fibrillar Aβ was specifically detected via immunoblot of the insoluble brain fraction (Fig 7B). Therefore, we excluded differences in the detection and binding properties of Thiazine red to be the underlying cause for the observed reduction in the levels of fibrillar Aβ in APP-KI mice. Taken together, although immunohistochemistry revealed comparable Aβ plaque coverage in APPPS1 and APP-KI mice, the amount of fibrillar Aβ was significantly lower in APP-KI mice.

Microglial recruitment is triggered by fibrillar Aβ and not by dystrophic neurites

To determine what triggers microglial reactivity in AD, we first quantified microglial recruitment to Aβ plaques in both mouse models. This analysis was done at the early pathological stage (3 months), where we identified prominent differences in the proteome regulation (Fig 1C and D; Fig 2A) as well as in the amount of fibrillar Aβ (Fig 7A and B) between the two AD mouse models. Immunohistochemical analysis revealed IBA1 positive, amoeboid microglia recruited to large, Thiazine red positive, fibrillar Aβ plaque cores in APPPS1 mice. Of note, we observed intracellular fibrillar Aβ in APPPS1 microglia in close contact to the plaque core (Fig 8A) as previously reported (Bolmont et al., 2008). Despite the significantly smaller fibrillar Aβ plaque core in APP-KI mice, we could observe IBA1 positive microglia polarized towards the fibrillar Aβ, rather than to the surrounding non-fibrillar Aβ positive material (Fig 8A). Quantification analysis revealed increased clustering of IBA1 positive microglia around Aβ plaques in APPPS1 compared to the APP-KI mice (Fig 8B), which display overall larger Aβ plaque size (Fig 8C). Likewise, we observed increased CD68 immunoreactivity around Aβ plaques in the APPPS1 compared to the APP-KI mice (Fig 8D and E). However, CD68 signal per individual microglial cell in the plaque vicinity was similar in both models (Fig 8F), suggesting that differences in AD-associated microglial proteins are due to the number of recruited microglia rather than differences in their individual CD68 protein levels.

Besides Aβ, microglial recruitment has also been associated with neuritic damage (dystrophic neurites) (Hemonnot et al., 2019). Accordingly, we analyzed dystrophic neurite pathology in 3 month old APPPS1 and APP-KI mice, using an antibody against APP that accumulates in these structures (Cummings et al., 1992; Sadleir et al., 2016). As previously reported (Radde et al., 2006), amyloid plaques in the APPPS1 mice were surrounded by prominent dystrophic neurites (Fig 8G). Interestingly, despite the reduced load of fibrillar Aβ, we readily detected dystrophic neurites in the APP-KI mice (Fig 8G). Moreover, our quantification analysis revealed a trend towards an increased dystrophic neurite area in the APP-KI compared to the APPPS1 mice (Fig 8H). Therefore, the differences in early microglial recruitment to APPPS1 plaques and the consecutive proteomic changes are less likely to be triggered by dystrophic neurites.

Altogether, we hypothesize that microglial recruitment is primarily triggered by the fibrillar Aβ content of amyloid plaques which drives the acquisition of MARP signatures.

Phagocytic impairments correlate with the occurrence of MARP signatures

The differences observed in the dynamics of microglial response to amyloid in the APPPS1 and the APP-KI mice prompted us to examine the association between microglial phagocytic function and the appearance of MARP signatures. To this end, we assessed the phagocytic capacity of microglia from 3 and 6 month old APPPS1 and APP-KI mice compared to the corresponding age-matched WT microglia using the *E.coli*-pHrodo uptake assay (Gotzl et al., 2019; Kleinberger et al., 2014). We already detected phagocytic dysfunction in 3 month old APPPS1 microglia, which was reflected by a prominent decrease in the amount of intracellular *E.coli* particles (Fig 8I; Suppl. Fig 8A) and a reduced number of CD11b positive cells that were capable of *E.coli* uptake (Fig 8J; Suppl. Fig 8B). Notably, APPPS1 phagocytic impairment did not change further in 6 month old microglia, suggesting that microglial functional deficits, as measured by the *E.coli* uptake assay, were fully established already at 3 months of age and characterized by early MARPs. In contrast, APP-KI microglia remained functional at 3 months, but at 6 months displayed similar impairments as seen in APPPS1 microglia (Fig 8I and J). Overall, we observed different kinetics of microglial dysfunction among mouse models which correlate with the appearance of MARPs and, in turn, with the presence fibrillar Aβ.

Discussion

This study presents an in-depth and time-resolved proteome of microglia isolated across different stages of Aβ accumulation in the APPPS1 and APP-KI mouse models, resulting in the identification of early, middle, and advanced MARPs. Importantly, we demonstrated that the structure of amyloid plaques (fibrillar *versus* non-fibrillar) is a major determinant driving the molecular alterations of microglia. Key microglial signatures encompass proteins with a central function in microglial biology and AD pathogenesis. Moreover, our functional analysis shows that early MARP signatures already reflect microglial phagocytic dysfunction.

To achieve robust and reproducible relative quantification of microglial proteins from single mice, we improved the yield of acutely isolated microglia to an average of $2x10^6$ cells per mouse brain, compared to recently published protocols (Flowers et al., 2017; Rangaraju et al., 2018). Next, by establishing the more sensitive DIA method for protein quantification, we improved the number of consistently identified proteins by 29.3% and obtained on average 5699 (APPPS1) and 5698 (APP-KI) relatively quantified proteins. Notably, our analysis enhanced the detection of low abundance proteins and does not require data imputation. The advancement to previous studies (Rangaraju et al., 2018; Sharma et al., 2015) is also exemplified by quantification of membrane proteins, including well

known microglial homeostatic markers TMEM119 or P2RY12. We also measured alterations in proteins that were postulated to be only altered at the transcriptional level in AD microglia (Rangaraju et al., 2018), including up-regulation of middle MARPs FABP3, FABP5, MIF and PLP2. In summary, our study achieved a major improvement in quantitative proteomic analysis of rodent microglia (Flowers et al., 2017; Rangaraju et al., 2018; Thygesen et al., 2018). This methodological advance enabled us to map microglial changes across diverse stages of Aβ pathology in two widely explored pre-clinical models of amyloidosis. Generated proteomic profiles characterize microglia under diseased conditions and can be used as a resource to track changes upon microglial therapeutic modification, such as Aβ immunotherapy. Such studies would facilitate discovery of clinically relevant molecular alterations that are necessary for microglial functional repair, monitoring disease progression and therapeutic efficacy.

The TREM2/APOE axis plays a key role in the regulation of the microglial transcriptional program and guides the homeostatic/DAM signature switch (Jay et al., 2017; Keren-Shaul et al., 2017; Krasemann et al., 2017). Our time-resolved proteomic analysis observed major rearrangements of the microglial proteomic landscape in both APPPS1 and APP-KI mice and revealed a partial overlap between MARPs and transcriptional profiles of DAM and homeostatic microglia (Keren-Shaul et al., 2017), but also identified additional microglial marker proteins throughout different stages of Aβ deposition.

Early MARPs include proteins of the interferon response, which is consistent with the recently identified interferon-responsive microglial sub-population in AD mice (Sala Frigerio et al., 2019). Numerous up-regulated early MARPs, including CD74, CTSZ, HEXA, CTSH, GLB1, CD68, NPC2, CLN3 and PI4K2A, reflect alterations in endo-lysosomal homeostasis as an early pathological insult in AD microglia (Van Acker et al., 2019). Additionally, factors of the fatty acid and cholesterol metabolism are altered throughout all pathological phases. Up-regulated are the early (APOE, ACACA, and SOAT1) middle (FABP3, FABP5, NCEH1, APOD, AACS, ACOX3, HACD2) and advanced MARPs (ACOT11, ACSBG1, ECHS1, ELOVL1, and FASN) and down-regulated are several middle and advanced MARPs (NAAA, FAM213B, HPGD, HPGDS, and PRKAB1), linking microglial lipid dyshomeostasis and AD pathology.

An inflammatory response in AD is suggested by the significant up-regulation of early MARPs LGALS3 and its binding protein (LGALS3BP). Recent findings suggested that the LGALS3/TREM2 signalling pathway, that acts as an inflammatory regulator of amyloid plaque formation, may also be of relevance for AD pathology in humans (Boza-Serrano et al., 2019). Further evidence that some of

366 the presented proteomic alterations of rodent microglia may be relevant for human disease is given by
367 the detection of up-regulated early/middle microglial MARPs, including CD68, TREM2 and ITGAX
368 in microglia surrounding amyloid plaques in postmortem AD brains (Hopperton et al., 2018). As
369 microglia emerge as a promising therapeutic target in AD, additional MARP signatures should be
370 validated in human tissue. In particular, early MARPs that are strongly increased in both AD mouse
371 models may serve as a resource to identify novel AD biomarkers and more specific microglial positron
372 emission tomography (PET) tracers that are urgently needed to monitor microglial reactivity *in vivo*
373 (Edison et al., 2018; Hemonnot et al., 2019). Middle and late MARPs reveal a decrease of microglial
374 homeostatic functions affecting chemotaxis, cell migration and phagocytosis (e.g., CX3CR1, SYK,
375 P2RY12, BIN2, TFEB and TFE3) and thus mark AD progression.

376 It is still being discussed which is the main trigger for microglial recruitment to amyloid
377 plaques and their molecular switch from a homeostatic to a neurodegenerative phenotype (Hemonnot
378 et al., 2019; Jung et al., 2015; Krasemann et al., 2017). Our study proposes that microglial recruitment
379 to Aβ deposits and their corresponding disease-associated proteomic alterations are triggered by
380 fibrillar Aβ, rather than by dystrophic neurites. We observed more diffuse amyloid plaque
381 morphology with less fibrillar Aβ and prominent neuritic dystrophies in the APP-KI mice. Similar
382 plaque morphology, with less fibrillar Aβ, is also observed in AD mice deficient for TREM2 or APOE
383 that also have less microglial cells recruited to amyloid plaques and display prominent neuritic
384 dystrophies (Parhizkar et al., 2019; Sala Frigerio et al., 2019; Ulrich et al., 2018; Wang et al., 2015;
385 Yuan et al., 2016). APOE may have a dual role and control the transcriptional/translational response
386 of microglia to amyloid as well as amyloid plaque compactness that directs microglial recruitment
387 and thus creates a regulatory feedback-loop. These findings are also strengthened by the relevance of
388 *ApoE* and *Trem2* as genetic risk factors of AD (Karch and Goate, 2015). Fibrillar Aβ as the trigger
389 for microglial recruitment is also supported by the human pathology where neuritic plaques in AD
390 brains were found surrounded by microglia. In contrast, microglial clustering was not detected at
391 diffuse plaques lacking fibrillar Aβ core (D'Andrea et al., 2004).

392 Although DAM signatures have been suggested as a protective response, there is still a lack of
393 direct experimental evidence linking specific transcriptomic or proteomic profiles to improved
394 microglial function. Importantly, our study demonstrates a functional link between proteomic changes
395 and reduced phagocytosis by AD microglia. APPPS1 microglia start acquiring early MARPs at the
396 age of 3 months, which is already accompanied by reduced phagocytic function. In contrast, less
397 altered proteomic signatures of 3 month old APP-KI microglia correlated with preserved phagocytic

function. Pronounced MARP signatures that appeared later in APP-KI microglia (6 months) were subsequently in accordance with phagocytic impairments. Therefore, differences in plaque fibrillization in both mouse models did not only affect microglial recruitment and activation, but also the phagocytic function of microglia.

Reduced phagocytosis of AD microglia might be related to observed proteomic alterations in lysosomal proteins or cell receptors. TREM2, which was found to be increased in both mouse models, plays an important role in phagocytosis as mutations of TREM2 related to AD and FTLD impair phagocytic activity of microglia (Kleinberger et al., 2014). However, up-regulation of the TREM2/APOE axis involves up-regulation of many lysosomal proteins (e.g., cathepsins or CD68) that are part of MARPs and altered in APPPS1 and APP-KI microglia. This may reflect a compensatory mechanism initiated as a response of microglia to Aβ accumulation in order to enhance phagocytic function. Eventually this frustrated microglial response fails to translate into improved Aβ clearance capability.

Phagocytosis might also be altered through differential regulation of toll like receptors (TLR). Among the TLRs, TLR2, an Aβ binding receptor (Liu et al., 2012; McDonald et al., 2016), showed the strongest increase with age while TLR9 was significantly reduced in APPPS1 and APP-KI mice. Along these lines, TLR2 deficiency reduced the inflammatory response of microglia to Aβ42, but increased Aβ phagocytosis in cultured microglia (Liu et al., 2012) while TLR9 is associated with improved Aβ clearance (Scholtzova et al., 2009). Thus, differential regulation of TLRs might contribute to the reduced phagocytic activity of aged APPPS1 microglia (Daria et al., 2017).

Additionally, many purinergic receptors (e.g., P2RX7, P2RY12 or P2RY13), which are important regulators of chemotaxis, phagocytosis, membrane polarization, and inflammatory signaling and thus emerged as possible microglial targets in AD (Calovi et al., 2019; Hemonnot et al., 2019), were found to be down-regulated in both AD mouse models. P2RY12 is regarded as a marker for ramified non-inflammatory microglia (Mildner et al., 2017) that is reduced in response to Aβ plaques and therefore represents a homeostatic microglial marker (Keren-Shaul et al., 2017; Krasemann et al., 2017). In contrast, P2RX4, a purinergic receptor that is likely to be involved in shifting microglia towards a pro-inflammatory phenotype (Calovi et al., 2019) or myelin phagocytosis (Zabala et al., 2018) had an increased abundance in both AD models. Taken together, our data emphasize alterations of purinergic receptor signaling in AD microglia that may regulate a morphological change towards amoeboid microglia with reduced motility and increased pro-inflammatory activity.

Our study confirms that both mouse models are valuable tools for studying Aβ–induced pathological changes of microglia that are remarkably comparable at advanced stages of amyloidosis. However, the observed differences in the dynamics of early, middle and late MARPs in APPPS1 and APP-KI mice should be considered for the design of pre-clinical studies of microglial repair and will require different time windows for microglial modulation.

In conclusion, we tracked pathological alterations of microglia in two AD mouse models using a proteomic approach. Our work demonstrates that microglial alterations are triggered as a response to Aβ deposition as pre-deposition stages do not reveal proteomic alterations. The conversion to MARPs is supported by changes in TREM2-APOE regulation mechanism. AD microglia display pronounced interferon stimulation, increased antigen presentation, alterations in cell surface receptors, lipid homeostasis and metabolism. Those proteomic changes in microglia occur as a response to fibrillar Aβ and are reflected in amoeboid microglial morphology and impaired phagocytic capacity. Finally, our proteomic dataset serves a valuable research resource providing information on microglial alterations over different stages of Aβ deposition that can be used to monitor therapeutic efficacy of microglial repair strategies.

Materials and Methods

Animals

Male and female mice of the hemizygous APPPS1 mouse line overexpressing human $APP_{KM670/671NL}$ and $PS1_{L166P}$ under the control of the Thy-1 promoter (Radde et al., 2006), homozygous $App^{NL\text{-}G\text{-}F}$ mouse line (Saito et al., 2014) and the C57BL/6J (WT) line were used in this study. Mice were group housed under specific pathogen-free conditions. Mice had access to water and standard mouse chow (Ssniff® Ms-H, Ssniff Spezialdiäten GmbH, Soest, Germany) *ad libitum* and were kept under a 12/12 h light-dark cycle in IVC System Typ II L-cages (528 cm^2) equipped with solid floors and a layer of bedding. All animal experiments were performed in compliance with the German animal welfare law and have been approved by the government of Upper Bavaria.

Isolation of primary microglia

Primary microglia were isolated from mouse brains (cerebrum) using MACS Technology (Miltenyi Biotec) according to manufacturer´s instructions and as previously described (Daria et al., 2017). Briefly, olfactory bulb, brain stem and cerebellum were removed and the remaining tissue (cerebrum) was freed from meninges and dissociated by enzymatic digestion using a Neural Tissue Dissociation

Kit P (Miltenyi Biotec). Subsequently, mechanical dissociation was performed by using 3 fire-polished glass Pasteur pipettes of decreasing diameter. CD11b positive microglia were magnetically labelled using CD11b MicroBeads, loaded onto a MACS LS Column (Miltenyi Biotec) and subjected to magnetic separation, resulting in CD11b-enriched (microglia-enriched) and CD11b-depleted (microglia-depleted) fractions. Obtained microglia-enriched pellets were either washed twice with HBSS (Gibco) supplemented with 7 mM HEPES, frozen in liquid nitrogen and stored at -80°C for biochemical or mass spectrometry analysis or resuspended in microglial culturing media and used for phagocytosis assay as described below.

Sample preparation for mass spectrometry

Microglia-enriched pellets were lysed in 200 µL of STET lysis buffer (50 mM Tris, 150 mM NaCl, 2 mM EDTA, 1% Triton, pH 7.5) at 4°C with intermediate vortexing. The samples were centrifuged for 5 min at 16000 x g at 4°C to remove cell debris and undissolved material. The supernatant was transferred to a LoBind tube (Eppendorf) and the protein concentration estimated using the Pierce 660 nm protein assay (ThermoFisher Scientific). A protein amount of 15 µg was subjected to tryptic protein digestion applying the the filter aided sample preparation protocol (FASP) (Wisniewski et al., 2009) using Vivacon spin filters with a 30 kDa cut-off (Sartorius). Briefly, proteins were reduced with 20 mM dithiothreitol and free cystein residues were alkylated with 50 mM iodoacetamide (Sigma Aldrich). After the urea washing steps, proteins were digested with 0.3 µg LysC (Promega) for 16 h at 37°C followed by a second digestion step with 0.15 µg trypsin (Promega) for 4 h at 37°C. The peptides were eluted into collection tubes and acidified with formic acid (Sigma Aldrich). Afterwards, proteolytic peptides were desalted by stop and go extraction (STAGE) with self-packed C18 tips (Empore C18 SPE, 3M) (Rappsilber et al., 2003). After vacuum centrifugation, peptides were dissolved in 20 µL 0.1% formic acid (Biosolve) and indexed retention time peptides were added (iRT Kit, Biognosys).

Liquid chromatography – tandem mass spectrometry analysis

For LFQ of proteins, peptides were analyzed on an Easy nLC 1000 or 1200 nanoHPLC (Thermo Scientific) which was coupled online via a Nanospray Flex Ion Source (Thermo Sientific) equipped with a PRSO-V1 column oven (Sonation) to a Q-Exactive HF mass spectrometer (Thermo Scientific). An amount of 1.3 µg of peptides was separated on in-house packed C18 columns (30 cm x 75 µm ID, ReproSil-Pur 120 C18-AQ, 1.9 µm, Dr. Maisch GmbH) using a binary gradient of water (A) and

acetonitrile (B) supplemented with 0.1% formic acid (0 min., 2% B; 3:30 min., 5% B; 137:30 min., 25% B; 168:30 min., 35% B; 182:30 min., 60% B) at 50°C column temperature.

For DDA, full MS scans were acquired at a resolution of 120000 (m/z range: 300-1400; AGC target: 3E+6). The 15 most intense peptide ions per full MS scan were selected for peptide fragmentation (resolution: 15000; isolation width: 1.6 m/z; AGC target: 1E+5; NCE: 26%). A dynamic exclusion of 120 s was used for peptide fragmentation.

For DIA, one scan cycle included a full MS scan (m/z range: 300-1400; resolution: 120000; AGC target: 5E+6 ions) and 25 MS/MS scans covering a range of 300-1400 m/z with consecutive m/z windows (resolution: 30000; AGC target: 3E+6 ions; Suppl. Table 1). The maximum ion trapping time was set to "auto". A stepped normalized collision energy of 26% ± 2.6% was used for fragmentation.

Microglia from APPPS1 mice were analyzed using DDA and DIA for method establishement. Microglia from APPPS1 and APP-KI mice were compared using DIA as it outperformed DDA.

Mass spectrometric LFQ and data analysis

For data acquired with DDA, the data was analyzed with the software Maxquant (maxquant.org, Max-Planck Institute Munich) version 1.6.1.0 (Cox et al., 2014). The MS data was searched against a reviewed canonical fasta database of *Mus musculus* from UniProt (download: November the 1st 2017, 16843 entries) supplemented with the sequence of human APP with the Swedish mutant and the iRT peptides. Trypsin was defined as a protease. Two missed cleavages were allowed for the database search. The option first search was used to recalibrate the peptide masses within a window of 20 ppm. For the main search peptide and peptide fragment mass tolerances were set to 4.5 and 20 ppm, respectively. Carbamidomethylation of cysteine was defined as static modification. Acetylation of the protein N-term as well as oxidation of methionine was set as variable modification. The FDR for both peptides and proteins was set to 1%. The "match between runs" option was enabled with a matching window of 1.5 min. LFQ of proteins required at least one ratio count of unique peptides. Only unique peptides were used for quantification. Normalization of LFQ intensities was performed separately for the age groups because LC-MS/MS data was acquired in different batches.

A spectral library was generated in Spectronaut (version 12.0.20491.11, Biognosys) (Bruderer et al., 2015) using the search results of Maxquant of the APPPS1 dataset. The library includes 122542 precursor ions from 91349 peptides, which represent 6223 protein groups. The DIA datasets of both mouse models were analyzed with this spectral library (version 12.0.20491.14.21367) with standard

settings. Briefly, the FDR of protein and peptide identifications was set to 1%. LFQ of proteins was performed on peptide fragment ions and required at least one quantified peptide per protein. Protein quantification was performed on maximum three peptides per protein group. The data of APPPS1 microglia was organized in age dependent fractions to enable separate normalization of the data. All LC-MS/MS runs of the APP-KI dataset were normalized against each other because all samples were analyzed in randomized order in one batch.

The protein LFQ reports of Maxquant and Spectronaut were further processed in Perseus (Tyanova et al., 2016). The protein LFQ intensities were log2 transformed and log2 fold changes were calculated between transgenic and wild type samples separately for the different age groups and mouse models. Only proteins with a consistent quantification in all samples of an age group were considered for statistical testing. A two-sided Student's t-test was applied to evaluate the significance of proteins with changed abundance. Additionally, a permutation based FDR estimation was used (Tusher et al., 2001). A log2 fold change larger than 0.5, or smaller than -0.5, a p-value less than 0.05, and significant regulation after FDR filtering were defined as regulation thresholds. The same thresholds were used for the comparison with transcriptomics data.

Gene ontology enrichment analysis was performed with the web-tool DAVID (version 6.8) (Huang da et al., 2009a, b) using GO_FAT terms. Up- and down-regulated early, middle and advanced MARPs were clustered separately for biological process, cellular component, and molecular function with all 5500 proteins, consistently quantified in APPPS1 and APP-KI microglia, as a customized background. A medium classification stringency was applied. An enrichment score of 1.3 was defined as threshold for cluster enrichment.

Biochemical characterization of brain tissue and isolated microglia

RIPA lysates were prepared from brain hemispheres, centrifuged at 100000 x g (60 min at 4°C) and the remaining pellet was homogenized in 0.5 mL 70% formic acid. The formic acid fraction was neutralized with 20 x 1 M Tris-HCl buffer at pH 9.5 and used for Aβ analysis. For Aβ detection, proteins were separated on Tris-Tricine (10-20%, Thermo Fisher Scientific) gels, transferred to nitrocellulose membranes (0.1 µm, GE Healthcare) which were boiled for 5 min in PBS and subsequently incubated with the blocking solution containing 0.2% I-Block (Thermo Fisher Scientific) and 0.1% Tween 20 (Merck) in PBS for 1 hour, followed by overnight incubation with rabbit polyclonal 3552 antibody (1:2000, (Yamasaki et al., 2006)). Antibody detection was performed

using the corresponding anti-HRP conjugated secondary antibody (Santa Cruz) and chemiluminescence detection reagent ECL (Thermo Fisher Scientific).

Microglia-enriched pellets were resuspended in 100 µL of STET lysis buffer (composition as described above for mass spectrometry, supplemented with proteinase and phosphatase inhibitors), kept on ice for 20 min and then sonicated for 4 cycles of 30 seconds. Cell lysates were then centrifugated at 9600 x g (5 min. at 4°C) and pellets discarded. Protein concentration was quantified using Bradford assay (Biorad) according to manufacturer instructions. 10 µg per sample using two independent microglial lysates per genotype were loaded on a bis-tris acrylamide gel (8% or 12%) and subsequently blotted onto either a PVDF or nitrocellulose membrane (Millipore) using the following antibodies: TREM2 (1:10, clone 5F4,(Xiang et al., 2016)); APOE (1:1000, AB947 Millipore); CD68 (1:1000, MCA1957GA, AbDserotec); CSF1R (1:1000, 3152, Cell Signaling) and FABP5 (1:400, AF1476, R&DSystems). Blots were developed using horseradish peroxidase-conjugated secondary antibodies (Promega) and the ECL chemiluminescence system (Amersham) or SuperSignal™ West Pico PLUS (Thermo Scientific). An antibody against GAPDH (1:2000, ab8245, Abcam) was used as loading control.

Immunohistochemistry

3 and 12 month old mice from the APPPS1 and APP-KI transgenic lines were anesthetized i.p. with a mixture of Ketamine (400 mg/kg) and Xylazine (27 mg/kg) and transcardially perfused with cold 0.1M PBS for 5 minutes followed by 4% Paraformaldehyde (PFA) in 0.1 M PBS for 15 minutes. Brains were isolated and postfixed for 20 minutes in 4% PFA in 0.1 M PBS and transferred to 30% sucrose in 0.1 M PBS for cryopreservation. Brains were embedded in optimal cutting temperature compound (O.C.T./ Tissue-Tek, Sakura), frozen on dry ice and kept at -80°C until sectioning. 30 µm coronal brain sections were cut using a cryostat (CryoSTAR NX70, Thermo Scientific) and placed in 0.1 M PBS until staining. Alternatively, sections were kept in anti-freezing solution (30% Glycerol, 30% Ethylenglycol, 10% 0.25 M PO_4 buffer, pH 7.2-7.4 and 30% dH_2O) at -20°C and briefly washed in 0.1M PBS before staining. Briefly, free-floating sections were permeabilized with 0.5% Triton-PBS (PBS-T) for 30 min, blocked either in 5% normal Goat Serum or 5% Donkey Serum in PBS-T for 1 hour and incubated overnight at 4°C in blocking solution with the following primary antibodies: IBA1 (1:500, 019-19741,Wako), IBA1 (1:500, ab5076, Abcam) NAB228 (1:2000, sc-32277, Santa Cruz), CD68 (1:500, MCA1957GA, AbDserotec), TREM2 (1:50, AF1729, R&DSystems), APP-Y188 (1:2000, ab32136, Abcam), CLEC7a (1:50, mabg-mdect, Invivogen), TMEM119 (1:200,

ab209064, Abcam), APOE-biotinilated (HJ6.3, 1:100, (Kim et al., 2012)) and 3552 (1:5000, (Yamasaki et al., 2006)). After primary antibody incubation, brain sections were washed 3 times with PBS-T and incubated with appropriate fluorophore-conjugated or streptavidine-fluorophore conjugated (for APOE biotinylated antibody) secondary antibodies (1:500, Life Technologies) together with nuclear stain Hoechst 33342 (1:2000, H3570,ThermoFisher), for two hours at room temperature (RT). Fibrillar dense core plaques were stained with Thiazine red (Sigma Aldrich, 2 µM solution in PBS) for 20 min in the dark at RT (after secondary antibody staining). Sections were subsequently washed three times with PBS-T mounted onto glass slides (Thermo Scientific), dried in the dark for at least 30 min, mounted using Gel Aqua Mount media (Sigma Aldrich) and analyzed by confocal microscopy.

Image acquisition, analysis and quantifications

3 month old APPPS1 and APP-KI mice were used for the analysis of dystrophic neurites, microglial recruitment to amyloid plaques and CD68 coverage area. All quantification analysis included 3 mice per genotype. 30 z-stack images (~10 µm thick) of single cortical plaques were acquired per experiment using a confocal microscope (63X water objective with 2x digital zoom, 600 Hz, Leica TCS SP5 II) from 6 brain slices (5 plaques per slice) for the microglial recruitment and dystrophic neurite analysis, or from 3 brain slices (10 plaques per slice) for CD68 coverage area analysis. Microscopy acquisition settings were kept constant within the same experiment. Maximal intensity projection pictures from every z-stack were created using ImageJ software and for every image, a defined region of interest (ROI) was manually drawn around every plaque (including microglia recruited -in contact- to the plaque). APP (Y188 antibody) and CD68 coverage area were quantified using the "Threshold" and "Analyze Particles" (inclusion size of 1-Infinity) functions from ImageJ software (NIH) within the ROI. The area covered by CD68 was normalized to the total Aβ plaque area (NAB228 antibody) or was divided by the number of microglia (IBA1 positive cells) recruited to the plaque within the ROI. The absolute values of area covered by neuritic dystrophies or Aβ plaques are represented in square micrometers (µm²). Microglial recruitment to plaques was quantified by counting the number of microglia (IBA1 positive cells) around amyloid plaques through the z-stack images within the defined ROI using the cell counter function of ImageJ software. Number of microglial cells at amyloid plaques was normalized to the area covered by Aβ (NAB228 antibody) and expressed as number of microglial cells per µm² of Aβ plaque.

Representative images from microglial recruitment analysis (IBA1 positive cells and CD68 coverage) were taken using the confocal microscope (63X water objective with 2x digital zoom, 400 Hz, Leica TCS SP5 II). Representative picture of microglia polarized towards amyloid cores was taken using a 63X confocal water objective with 3x digital zoom.

For immunohistological validation of the proteome analysis and amyloid pathology, representative pictures in similar regions were taken by confocal microscopy using the same settings for all three different genotypes (WT, APPPS1 and APP-KI). Low magnification pictures were taken with 20X dry confocal objective with 2x digital zoom and higher magnification ones with 63X confocal water objective with 3x digital zoom. Images of Aβ pathology (NAB228 antibody) were taken with a tile scan system covering similar brain regions (10X confocal dry objective). Representative images of Aβ composition (NAB228, ThR and IBA1) were taken with a confocal 20X dry objective.

Microglial phagocytosis of E.coli particles

Microglial phagocytosis was performed similarly as previously described (Kleinberger et al., 2014). Microglia isolated from 3 or 6 month old APPPS1, APP-KI and WT mice were plated onto 24 well plate at a density of $2x10^5$ cells per well and cultured for 24 hours in a humidified 5% CO_2 incubator at 36.5°C in DMEM/F12 media (Invitrogen) supplemented with 10% heat inactivated FCS (Sigma), 1% Penicillin-Streptomycin (Invitrogen) and 10 ng/mL GM-CSF (R&DSystems). After 24 hours, plating media were replaced with fresh media. After 5 days in culture, microglia were incubated with 50 µL of *E.coli* particle suspension (pHrodo™ Green *E.coli* BioParticles™, P35366, Invitrogen™) for 60 min. Cytochalasin D (CytoD, 10 µM, from10 mM stock in DMSO) was used as phagocytosis inhibitor and added 30 min prior to addition of bacterial particles. Bacteria suspension excess was washed 4 times with PBS (on ice) and microglia that were attached to the plate were incubated with CD11b-APC-Cy7 antibody (1:200, clone M1/70, 557657, BD) in FACS buffer (PBS supplemented with 2mM EDTA and 1% FBS) for 30 min at 4°C. Microglia were then washed twice with PBS, scraped off the wells in FACS buffer and analyzed by flow cytometry. For the analysis of 3 month old mice, 3 independent experiments were performed per genotype, and each experiment included a minimum of 3 technical replicates with the exception of CytoD condition (2 technical replicates). For the analysis of 6 month old mice, 2 independent experiments were performed per genotype, and each experiment included a minimum of 4 technical replicates with the exception of CytoD condition (2 technical replicates).

FACS analysis

For the microglial isolation quality control, around 12000 cells from a CD11b-enriched and CD11b-depleted fractions were stained in suspension with CD11b-APC-Cy7 antibody (1:200, clone M1/70, 557657, BD) in FACS buffer for 30 minutes at 4°C. After several washes with PBS, microglia were resuspended in FACS buffer for analysis. Propidium Iodide (PI) staining was done 10 minutes prior FACS analysis. Flow cytometric data was acquired on a BD FACSverse flow cytometer by gating according to single stained and unstained samples and analyzed using FlowJo software (Treestar). Mean fluorescent intensity (MFI) is represented as the geometric mean of the according fluorochrome.

Statistical analysis

The data are presented as mean ± standard deviation of the mean (± SD) from 3 independent experiments with the exception of the phagocytic assay in 6 month old mice (Fig 8) were 2 independent experiments were performed. For the microglial recruitment and analysis of dystrophic neurites, statistical significance (P value) was calculated using the unpaired two-tailed Student's *t*-test. Phagocytic assay was analyzed by the Dunnett's multiple comparison test of the Two-way ANOVA. Both statistical analysis were performed in GraphPad Prism. P value of <0.05 was considered to be statistically significant (*; $P < 0.05$, **; $P < 0.01$ and ***; $P < 0.001$, n.s. = not significant).

Data Availability

The mass spectrometry proteomics data have been deposited to the ProteomeXchange Consortium via the PRIDE partner repository (Perez-Riverol et al., 2019) with the dataset identifier PXD016075.

Acknowledgements

We thank Allison Morningstar and Matthias Prestel for critically reading the manuscript. The authors are grateful to Mathias Jucker (Hertie-Institute for Clinical Brain Research, University of Tübingen, Germany) for providing the APPPS1 mice and David Holtzman (Washington University School of Medicine, St Louis, Missouri, USA) for providing the ApoE antibody. We thank Haike Hampel for excellent technical assistance. Funds have been provided by the Alzheimer Forschung Initiative e.V. This work was also supported by the Deutsche Forschungsgemeinschaft (German Research Foundation) within the framework of the Munich Cluster for Systems Neurology (EXC 2145 SyNergy), the European Research Council (ERC-StG 802305) and the Vascular Dementia Research

Foundation. C.H. is supported by a Koselleck Project of the DFG (HA1737/16-1) and the Helmholtz-Gemeinschaft (Zukunftsthema "Immunology and Inflammation" (ZT-0027)).

Author Contributions

S.T. and S.F.L. designed and supervised the study. S.T., S.F.L., S.A.M., L.S.M. wrote the manuscript with input of all co-authors. L.S.M. performed animal experiments including microglial isolation, target validation and functional studies. A.C. assisted in isolation of primary microglia. S.A.M., J.K., and A.B. performed the proteomic analysis. S.R., L.S.M. and A.L. performed FACS analysis. T.S. and T.C.S. provided the APP-KI mouse model. J.H. contributed to amyloid plaque analysis. L.S.M., M.W., and C.H. contributed to biochemical analysis. Correspondence and requests for materials should be addressed to S.T. or S.F. L.

Competing Interests

C.H. collaborates with Denali Therapeutics, participated on one advisory board meeting of Biogen, and received a speaker honorarium from Novartis and Roche. C.H. is chief advisor of ISAR Bioscience. All other authors declare that they have no competing interests.

References

Abner, E.L., Neltner, J.H., Jicha, G.A., Patel, E., Anderson, S.L., Wilcock, D.M., Van Eldik, L.J., and Nelson, P.T. (2018). Diffuse Amyloid-beta Plaques, Neurofibrillary Tangles, and the Impact of APOE in Elderly Persons' Brains Lacking Neuritic Amyloid Plaques. Journal of Alzheimer's disease : JAD *64*, 1307-1324. doi: 10.3233/JAD-180514.

Bacskai, B.J., Kajdasz, S.T., Christie, R.H., Carter, C., Games, D., Seubert, P., Schenk, D., and Hyman, B.T. (2001). Imaging of amyloid-beta deposits in brains of living mice permits direct observation of clearance of plaques with immunotherapy. Nature medicine *7*, 369-372. doi: 10.1038/85525.

Bard, F., Cannon, C., Barbour, R., Burke, R.L., Games, D., Grajeda, H., Guido, T., Hu, K., Huang, J., Johnson-Wood, K., *et al.* (2000). Peripherally administered antibodies against amyloid beta-peptide enter the central nervous system and reduce pathology in a mouse model of Alzheimer disease. Nature medicine *6*, 916-919. doi: 10.1038/78682.

Bohrmann, B., Baumann, K., Benz, J., Gerber, F., Huber, W., Knoflach, F., Messer, J., Oroszlan, K., Rauchenberger, R., Richter, W.F., *et al.* (2012). Gantenerumab: a novel human anti-Abeta antibody demonstrates sustained cerebral amyloid-beta binding and elicits cell-mediated removal of human amyloid-beta. Journal of Alzheimer's disease : JAD *28*, 49-69. doi: 10.3233/JAD-2011-110977.

Bolmont, T., Haiss, F., Eicke, D., Radde, R., Mathis, C.A., Klunk, W.E., Kohsaka, S., Jucker, M., and Calhoun, M.E. (2008). Dynamics of the microglial/amyloid interaction indicate a role in plaque maintenance. The Journal of neuroscience : the official journal of the Society for Neuroscience *28*, 4283-4292. doi: 10.1523/JNEUROSCI.4814-07.2008.

Bottcher, C., Schlickeiser, S., Sneeboer, M.A.M., Kunkel, D., Knop, A., Paza, E., Fidzinski, P., Kraus, L., Snijders, G.J.L., Kahn, R.S., *et al.* (2019). Human microglia regional heterogeneity and phenotypes determined by multiplexed single-cell mass cytometry. Nature neuroscience *22*, 78-90. doi: 10.1038/s41593-018-0290-2.

Boza-Serrano, A., Ruiz, R., Sanchez-Varo, R., Garcia-Revilla, J., Yang, Y., Jimenez-Ferrer, I., Paulus, A., Wennstrom, M., Vilalta, A., Allendorf, D., *et al.* (2019). Galectin-3, a novel endogenous TREM2 ligand, detrimentally regulates inflammatory response in Alzheimer's disease. Acta neuropathologica *138*, 251-273. doi: 10.1007/s00401-019-02013-z.

Bradshaw, E.M., Chibnik, L.B., Keenan, B.T., Ottoboni, L., Raj, T., Tang, A., Rosenkrantz, L.L., Imboywa, S., Lee, M., Von Korff, A., *et al.* (2013). CD33 Alzheimer's disease locus: altered monocyte function and amyloid biology. Nature neuroscience *16*, 848-850. doi: 10.1038/nn.3435.

Bruderer, R., Bernhardt, O.M., Gandhi, T., Miladinovic, S.M., Cheng, L.Y., Messner, S., Ehrenberger, T., Zanotelli, V., Butscheid, Y., Escher, C., *et al.* (2015). Extending the limits of quantitative proteome profiling with data-independent acquisition and application to acetaminophen-treated three-dimensional liver microtissues. Molecular & cellular proteomics : MCP *14*, 1400-1410. doi: 10.1074/mcp.M114.044305.

Butovsky, O., Jedrychowski, M.P., Moore, C.S., Cialic, R., Lanser, A.J., Gabriely, G., Koeglsperger, T., Dake, B., Wu, P.M., Doykan, C.E., *et al.* (2014). Identification of a unique TGF-beta-dependent molecular and functional signature in microglia. Nature neuroscience *17*, 131-143. doi: 10.1038/nn.3599.

Calovi, S., Mut-Arbona, P., and Sperlagh, B. (2019). Microglia and the Purinergic Signaling System. Neuroscience *405*, 137-147. doi: 10.1016/j.neuroscience.2018.12.021.

Castellano, J.M., Kim, J., Stewart, F.R., Jiang, H., DeMattos, R.B., Patterson, B.W., Fagan, A.M., Morris, J.C., Mawuenyega, K.G., Cruchaga, C., *et al.* (2011). Human apoE isoforms differentially regulate brain amyloid-beta peptide clearance. Sci Transl Med *3*, 89ra57. doi: 10.1126/scitranslmed.3002156.

748 Cox, J., Hein, M.Y., Luber, C.A., Paron, I., Nagaraj, N., and Mann, M. (2014). Accurate proteome-
749 wide label-free quantification by delayed normalization and maximal peptide ratio extraction, termed
750 MaxLFQ. Molecular & cellular proteomics : MCP *13*, 2513-2526. doi: 10.1074/mcp.M113.031591.
751 Cummings, B.J., Su, J.H., Geddes, J.W., Van Nostrand, W.E., Wagner, S.L., Cunningham, D.D., and
752 Cotman, C.W. (1992). Aggregation of the amyloid precursor protein within degenerating neurons and
753 dystrophic neurites in Alzheimer's disease. Neuroscience *48*, 763-777. doi: 10.1016/0306-
754 4522(92)90265-4.
755 Cuyvers, E., and Sleegers, K. (2016). Genetic variations underlying Alzheimer's disease: evidence
756 from genome-wide association studies and beyond. Lancet Neurol *15*, 857-868. doi: 10.1016/S1474-
757 4422(16)00127-7.
758 D'Andrea, M.R., Cole, G.M., and Ard, M.D. (2004). The microglial phagocytic role with specific
759 plaque types in the Alzheimer disease brain. Neurobiology of aging *25*, 675-683. doi:
760 10.1016/j.neurobiolaging.2003.12.026.
761 Daria, A., Colombo, A., Llovera, G., Hampel, H., Willem, M., Liesz, A., Haass, C., and Tahirovic, S.
762 (2017). Young microglia restore amyloid plaque clearance of aged microglia. The EMBO journal *36*,
763 583-603. doi: 10.15252/embj.201694591.
764 Edison, P., Donat, C.K., and Sastre, M. (2018). In vivo Imaging of Glial Activation in Alzheimer's
765 Disease. Front Neurol *9*, 625. doi: 10.3389/fneur.2018.00625.
766 Flowers, A., Bell-Temin, H., Jalloh, A., Stevens, S.M., Jr., and Bickford, P.C. (2017). Proteomic
767 anaysis of aged microglia: shifts in transcription, bioenergetics, and nutrient response. J
768 Neuroinflammation *14*, 96. doi: 10.1186/s12974-017-0840-7.
769 Galatro, T.F., Holtman, I.R., Lerario, A.M., Vainchtein, I.D., Brouwer, N., Sola, P.R., Veras, M.M.,
770 Pereira, T.F., Leite, R.E.P., Moller, T., *et al.* (2017). Transcriptomic analysis of purified human
771 cortical microglia reveals age-associated changes. Nature neuroscience *20*, 1162-1171. doi:
772 10.1038/nn.4597.
773 Gjoneska, E., Pfenning, A.R., Mathys, H., Quon, G., Kundaje, A., Tsai, L.H., and Kellis, M. (2015).
774 Conserved epigenomic signals in mice and humans reveal immune basis of Alzheimer's disease.
775 Nature *518*, 365-369. doi: 10.1038/nature14252.
776 Gosselin, D., Skola, D., Coufal, N.G., Holtman, I.R., Schlachetzki, J.C.M., Sajti, E., Jaeger, B.N.,
777 O'Connor, C., Fitzpatrick, C., Pasillas, M.P., *et al.* (2017). An environment-dependent transcriptional
778 network specifies human microglia identity. Science. doi: 10.1126/science.aal3222.
779 Gotzl, J.K., Brendel, M., Werner, G., Parhizkar, S., Sebastian Monasor, L., Kleinberger, G., Colombo,
780 A.V., Deussing, M., Wagner, M., Winkelmann, J., *et al.* (2019). Opposite microglial activation stages
781 upon loss of PGRN or TREM2 result in reduced cerebral glucose metabolism. EMBO molecular
782 medicine *11*. doi: 10.15252/emmm.201809711.
783 Grabert, K., Michoel, T., Karavolos, M.H., Clohisey, S., Baillie, J.K., Stevens, M.P., Freeman, T.C.,
784 Summers, K.M., and McColl, B.W. (2016). Microglial brain region-dependent diversity and selective
785 regional sensitivities to aging. Nature neuroscience *19*, 504-516. doi: 10.1038/nn.4222.
786 Guerreiro, R., Wojtas, A., Bras, J., Carrasquillo, M., Rogaeva, E., Majounie, E., Cruchaga, C., Sassi,
787 C., Kauwe, J.S., Younkin, S., *et al.* (2013). TREM2 variants in Alzheimer's disease. N Engl J Med
788 *368*, 117-127. doi: 10.1056/NEJMoa1211851.
789 Guillot-Sestier, M.V., and Town, T. (2013). Innate immunity in Alzheimer's disease: a complex affair.
790 CNS Neurol Disord Drug Targets *12*, 593-607. doi:
791 Hammond, T.R., Dufort, C., Dissing-Olesen, L., Giera, S., Young, A., Wysoker, A., Walker, A.J.,
792 Gergits, F., Segel, M., Nemesh, J., *et al.* (2019). Single-Cell RNA Sequencing of Microglia throughout
793 the Mouse Lifespan and in the Injured Brain Reveals Complex Cell-State Changes. Immunity *50*, 253-
794 271 e256. doi: 10.1016/j.immuni.2018.11.004.

795 Hemonnot, A.L., Hua, J., Ulmann, L., and Hirbec, H. (2019). Microglia in Alzheimer Disease: Well-
796 Known Targets and New Opportunities. Front Aging Neurosci *11*, 233. doi:
797 10.3389/fnagi.2019.00233.
798 Hickman, S.E., Allison, E.K., and El Khoury, J. (2008). Microglial dysfunction and defective beta-
799 amyloid clearance pathways in aging Alzheimer's disease mice. The Journal of neuroscience : the
800 official journal of the Society for Neuroscience *28*, 8354-8360. doi: 10.1523/JNEUROSCI.0616-
801 08.2008.
802 Holtman, I.R., Raj, D.D., Miller, J.A., Schaafsma, W., Yin, Z., Brouwer, N., Wes, P.D., Moller, T.,
803 Orre, M., Kamphuis, W., *et al.* (2015). Induction of a common microglia gene expression signature
804 by aging and neurodegenerative conditions: a co-expression meta-analysis. Acta neuropathologica
805 communications *3*, 31. doi: 10.1186/s40478-015-0203-5.
806 Holtzman, D.M., Morris, J.C., and Goate, A.M. (2011). Alzheimer's disease: the challenge of the
807 second century. Sci Transl Med *3*, 77sr71. doi: 10.1126/scitranslmed.3002369.
808 Hopperton, K.E., Mohammad, D., Trepanier, M.O., Giuliano, V., and Bazinet, R.P. (2018). Markers
809 of microglia in post-mortem brain samples from patients with Alzheimer's disease: a systematic
810 review. Molecular psychiatry *23*, 177-198. doi: 10.1038/mp.2017.246.
811 Huang da, W., Sherman, B.T., and Lempicki, R.A. (2009a). Bioinformatics enrichment tools: paths
812 toward the comprehensive functional analysis of large gene lists. Nucleic Acids Res *37*, 1-13. doi:
813 10.1093/nar/gkn923.
814 Huang da, W., Sherman, B.T., and Lempicki, R.A. (2009b). Systematic and integrative analysis of
815 large gene lists using DAVID bioinformatics resources. Nature protocols *4*, 44-57. doi:
816 10.1038/nprot.2008.211.
817 Jansen, I.E., Savage, J.E., Watanabe, K., Bryois, J., Williams, D.M., Steinberg, S., Sealock, J.,
818 Karlsson, I.K., Hagg, S., Athanasiu, L., *et al.* (2019). Genome-wide meta-analysis identifies new loci
819 and functional pathways influencing Alzheimer's disease risk. Nat Genet. doi: 10.1038/s41588-018-
820 0311-9.
821 Janus, C., Pearson, J., McLaurin, J., Mathews, P.M., Jiang, Y., Schmidt, S.D., Chishti, M.A., Horne,
822 P., Heslin, D., French, J., *et al.* (2000). A beta peptide immunization reduces behavioural impairment
823 and plaques in a model of Alzheimer's disease. Nature *408*, 979-982. doi: 10.1038/35050110.
824 Jay, T.R., Hirsch, A.M., Broihier, M.L., Miller, C.M., Neilson, L.E., Ransohoff, R.M., Lamb, B.T.,
825 and Landreth, G.E. (2017). Disease Progression-Dependent Effects of TREM2 Deficiency in a Mouse
826 Model of Alzheimer's Disease. The Journal of neuroscience : the official journal of the Society for
827 Neuroscience *37*, 637-647. doi: 10.1523/JNEUROSCI.2110-16.2016.
828 Jonsson, T., Stefansson, H., Steinberg, S., Jonsdottir, I., Jonsson, P.V., Snaedal, J., Bjornsson, S.,
829 Huttenlocher, J., Levey, A.I., Lah, J.J., *et al.* (2013). Variant of TREM2 associated with the risk of
830 Alzheimer's disease. N Engl J Med *368*, 107-116. doi: 10.1056/NEJMoa1211103.
831 Jordao, M.J.C., Sankowski, R., Brendecke, S.M., Sagar, Locatelli, G., Tai, Y.H., Tay, T.L., Schramm,
832 E., Armbruster, S., Hagemeyer, N., *et al.* (2019). Single-cell profiling identifies myeloid cell subsets
833 with distinct fates during neuroinflammation. Science *363*. doi: 10.1126/science.aat7554.
834 Jung, C.K., Keppler, K., Steinbach, S., Blazquez-Llorca, L., and Herms, J. (2015). Fibrillar amyloid
835 plaque formation precedes microglial activation. PloS one *10*, e0119768. doi:
836 10.1371/journal.pone.0119768.
837 Kamphuis, W., Kooijman, L., Schetters, S., Orre, M., and Hol, E.M. (2016). Transcriptional profiling
838 of CD11c-positive microglia accumulating around amyloid plaques in a mouse model for Alzheimer's
839 disease. Biochimica et biophysica acta *1862*, 1847-1860. doi: 10.1016/j.bbadis.2016.07.007.
840 Karch, C.M., and Goate, A.M. (2015). Alzheimer's disease risk genes and mechanisms of disease
841 pathogenesis. Biol Psychiatry *77*, 43-51. doi: 10.1016/j.biopsych.2014.05.006.

Keren-Shaul, H., Spinrad, A., Weiner, A., Matcovitch-Natan, O., Dvir-Szternfeld, R., Ulland, T.K., David, E., Baruch, K., Lara-Astaiso, D., Toth, B., *et al.* (2017). A Unique Microglia Type Associated with Restricting Development of Alzheimer's Disease. Cell *169*, 1276-1290 e1217. doi: 10.1016/j.cell.2017.05.018.

Kim, J., Eltorai, A.E., Jiang, H., Liao, F., Verghese, P.B., Kim, J., Stewart, F.R., Basak, J.M., and Holtzman, D.M. (2012). Anti-apoE immunotherapy inhibits amyloid accumulation in a transgenic mouse model of Abeta amyloidosis. J Exp Med *209*, 2149-2156. doi: 10.1084/jem.20121274.

Kleinberger, G., Yamanishi, Y., Suarez-Calvet, M., Czirr, E., Lohmann, E., Cuyvers, E., Struyfs, H., Pettkus, N., Wenninger-Weinzierl, A., Mazaheri, F., *et al.* (2014). TREM2 mutations implicated in neurodegeneration impair cell surface transport and phagocytosis. Sci Transl Med *6*, 243ra286. doi: 10.1126/scitranslmed.3009093.

Koellhoffer, E.C., McCullough, L.D., and Ritzel, R.M. (2017). Old Maids: Aging and Its Impact on Microglia Function. Int J Mol Sci *18*. doi: 10.3390/ijms18040769.

Krasemann, S., Madore, C., Cialic, R., Baufeld, C., Calcagno, N., El Fatimy, R., Beckers, L., O'Loughlin, E., Xu, Y., Fanek, Z., *et al.* (2017). The TREM2-APOE Pathway Drives the Transcriptional Phenotype of Dysfunctional Microglia in Neurodegenerative Diseases. Immunity *47*, 566-581 e569. doi: 10.1016/j.immuni.2017.08.008.

Lambert, J.C., Heath, S., Even, G., Campion, D., Sleegers, K., Hiltunen, M., Combarros, O., Zelenika, D., Bullido, M.J., Tavernier, B., *et al.* (2009). Genome-wide association study identifies variants at CLU and CR1 associated with Alzheimer's disease. Nat Genet *41*, 1094-1099. doi: 10.1038/ng.439.

Lathuiliere, A., Laversenne, V., Astolfo, A., Kopetzki, E., Jacobsen, H., Stampanoni, M., Bohrmann, B., Schneider, B.L., and Aebischer, P. (2016). A subcutaneous cellular implant for passive immunization against amyloid-beta reduces brain amyloid and tau pathologies. Brain : a journal of neurology *139*, 1587-1604. doi: 10.1093/brain/aww036.

Liu, S., Liu, Y., Hao, W., Wolf, L., Kiliaan, A.J., Penke, B., Rube, C.E., Walter, J., Heneka, M.T., Hartmann, T., *et al.* (2012). TLR2 is a primary receptor for Alzheimer's amyloid beta peptide to trigger neuroinflammatory activation. J Immunol *188*, 1098-1107. doi: 10.4049/jimmunol.1101121.

Mathys, H., Adaikkan, C., Gao, F., Young, J.Z., Manet, E., Hemberg, M., De Jager, P.L., Ransohoff, R.M., Regev, A., and Tsai, L.H. (2017). Temporal Tracking of Microglia Activation in Neurodegeneration at Single-Cell Resolution. Cell reports *21*, 366-380. doi: 10.1016/j.celrep.2017.09.039.

Mawuenyega, K.G., Sigurdson, W., Ovod, V., Munsell, L., Kasten, T., Morris, J.C., Yarasheski, K.E., and Bateman, R.J. (2010). Decreased clearance of CNS beta-amyloid in Alzheimer's disease. Science *330*, 1774. doi: 10.1126/science.1197623.

Mazaheri, F., Snaidero, N., Kleinberger, G., Madore, C., Daria, A., Werner, G., Krasemann, S., Capell, A., Trumbach, D., Wurst, W., *et al.* (2017). TREM2 deficiency impairs chemotaxis and microglial responses to neuronal injury. EMBO reports. doi: 10.15252/embr.201743922.

McDonald, C.L., Hennessy, E., Rubio-Araiz, A., Keogh, B., McCormack, W., McGuirk, P., Reilly, M., and Lynch, M.A. (2016). Inhibiting TLR2 activation attenuates amyloid accumulation and glial activation in a mouse model of Alzheimer's disease. Brain Behav Immun *58*, 191-200. doi: 10.1016/j.bbi.2016.07.143.

McQuade, A., and Blurton-Jones, M. (2019). Microglia in Alzheimer's Disease: Exploring How Genetics and Phenotype Influence Risk. Journal of molecular biology *431*, 1805-1817. doi: 10.1016/j.jmb.2019.01.045.

Mildner, A., Huang, H., Radke, J., Stenzel, W., and Priller, J. (2017). P2Y12 receptor is expressed on human microglia under physiological conditions throughout development and is sensitive to neuroinflammatory diseases. Glia *65*, 375-387. doi: 10.1002/glia.23097.

889 Morgan, D., Diamond, D.M., Gottschall, P.E., Ugen, K.E., Dickey, C., Hardy, J., Duff, K., Jantzen,
890 P., DiCarlo, G., Wilcock, D., *et al.* (2000). A beta peptide vaccination prevents memory loss in an
891 animal model of Alzheimer's disease. Nature *408*, 982-985. doi: 10.1038/35050116.
892 Mrdjen, D., Pavlovic, A., Hartmann, F.J., Schreiner, B., Utz, S.G., Leung, B.P., Lelios, I., Heppner,
893 F.L., Kipnis, J., Merkler, D., *et al.* (2018). High-Dimensional Single-Cell Mapping of Central Nervous
894 System Immune Cells Reveals Distinct Myeloid Subsets in Health, Aging, and Disease. Immunity *48*,
895 380-395 e386. doi: 10.1016/j.immuni.2018.01.011.
896 Naj, A.C., Jun, G., Beecham, G.W., Wang, L.S., Vardarajan, B.N., Buros, J., Gallins, P.J., Buxbaum,
897 J.D., Jarvik, G.P., Crane, P.K., *et al.* (2011). Common variants at MS4A4/MS4A6E, CD2AP, CD33
898 and EPHA1 are associated with late-onset Alzheimer's disease. Nat Genet *43*, 436-441. doi:
899 10.1038/ng.801.
900 Nicoll, J.A., Barton, E., Boche, D., Neal, J.W., Ferrer, I., Thompson, P., Vlachouli, C., Wilkinson, D.,
901 Bayer, A., Games, D., *et al.* (2006). Abeta species removal after abeta42 immunization. Journal of
902 neuropathology and experimental neurology *65*, 1040-1048. doi:
903 10.1097/01.jnen.0000240466.10758.ce.
904 Nicoll, J.A., Wilkinson, D., Holmes, C., Steart, P., Markham, H., and Weller, R.O. (2003).
905 Neuropathology of human Alzheimer disease after immunization with amyloid-beta peptide: a case
906 report. Nature medicine *9*, 448-452. doi: 10.1038/nm840.
907 Orre, M., Kamphuis, W., Osborn, L.M., Jansen, A.H., Kooijman, L., Bossers, K., and Hol, E.M.
908 (2014a). Isolation of glia from Alzheimer's mice reveals inflammation and dysfunction. Neurobiology
909 of aging *35*, 2746-2760. doi: 10.1016/j.neurobiolaging.2014.06.004.
910 Orre, M., Kamphuis, W., Osborn, L.M., Melief, J., Kooijman, L., Huitinga, I., Klooster, J., Bossers,
911 K., and Hol, E.M. (2014b). Acute isolation and transcriptome characterization of cortical astrocytes
912 and microglia from young and aged mice. Neurobiology of aging *35*, 1-14. doi:
913 10.1016/j.neurobiolaging.2013.07.008.
914 Parhizkar, S., Arzberger, T., Brendel, M., Kleinberger, G., Deussing, M., Focke, C., Nuscher, B.,
915 Xiong, M., Ghasemigharagoz, A., Katzmarski, N., *et al.* (2019). Loss of TREM2 function increases
916 amyloid seeding but reduces plaque-associated ApoE. Nature neuroscience *22*, 191-204. doi:
917 10.1038/s41593-018-0296-9.
918 Perez-Riverol, Y., Csordas, A., Bai, J., Bernal-Llinares, M., Hewapathirana, S., Kundu, D.J., Inuganti,
919 A., Griss, J., Mayer, G., Eisenacher, M., *et al.* (2019). The PRIDE database and related tools and
920 resources in 2019: improving support for quantification data. Nucleic Acids Res *47*, D442-D450. doi:
921 10.1093/nar/gky1106.
922 Radde, R., Bolmont, T., Kaeser, S.A., Coomaraswamy, J., Lindau, D., Stoltze, L., Calhoun, M.E.,
923 Jaggi, F., Wolburg, H., Gengler, S., *et al.* (2006). Abeta42-driven cerebral amyloidosis in transgenic
924 mice reveals early and robust pathology. EMBO reports *7*, 940-946. doi: 10.1038/sj.embor.7400784.
925 Rangaraju, S., Dammer, E.B., Raza, S.A., Gao, T., Xiao, H., Betarbet, R., Duong, D.M., Webster,
926 J.A., Hales, C.M., Lah, J.J., *et al.* (2018). Quantitative proteomics of acutely-isolated mouse microglia
927 identifies novel immune Alzheimer's disease-related proteins. Molecular neurodegeneration *13*, 34.
928 doi: 10.1186/s13024-018-0266-4.
929 Rappsilber, J., Ishihama, Y., and Mann, M. (2003). Stop and go extraction tips for matrix-assisted
930 laser desorption/ionization, nanoelectrospray, and LC/MS sample pretreatment in proteomics.
931 Analytical chemistry *75*, 663-670. doi:
932 Reddy, P.H., Manczak, M., Zhao, W., Nakamura, K., Bebbington, C., Yarranton, G., and Mao, P.
933 (2009). Granulocyte-macrophage colony-stimulating factor antibody suppresses microglial activity:
934 implications for anti-inflammatory effects in Alzheimer's disease and multiple sclerosis. Journal of
935 neurochemistry *111*, 1514-1528. doi: 10.1111/j.1471-4159.2009.06432.x.

Sadleir, K.R., Kandalepas, P.C., Buggia-Prevot, V., Nicholson, D.A., Thinakaran, G., and Vassar, R. (2016). Presynaptic dystrophic neurites surrounding amyloid plaques are sites of microtubule disruption, BACE1 elevation, and increased Abeta generation in Alzheimer's disease. Acta neuropathologica *132*, 235-256. doi: 10.1007/s00401-016-1558-9.

Saido, T.C. (1998). Alzheimer's disease as proteolytic disorders: anabolism and catabolism of beta-amyloid. Neurobiology of aging *19*, S69-75. doi:

Saito, T., Matsuba, Y., Mihira, N., Takano, J., Nilsson, P., Itohara, S., Iwata, N., and Saido, T.C. (2014). Single App knock-in mouse models of Alzheimer's disease. Nature neuroscience *17*, 661-663. doi: 10.1038/nn.3697.

Sala Frigerio, C., Wolfs, L., Fattorelli, N., Thrupp, N., Voytyuk, I., Schmidt, I., Mancuso, R., Chen, W.T., Woodbury, M.E., Srivastava, G., *et al.* (2019). The Major Risk Factors for Alzheimer's Disease: Age, Sex, and Genes Modulate the Microglia Response to Abeta Plaques. Cell reports *27*, 1293-1306 e1296. doi: 10.1016/j.celrep.2019.03.099.

Schenk, D., Barbour, R., Dunn, W., Gordon, G., Grajeda, H., Guido, T., Hu, K., Huang, J., Johnson-Wood, K., Khan, K., *et al.* (1999). Immunization with amyloid-beta attenuates Alzheimer-disease-like pathology in the PDAPP mouse. Nature *400*, 173-177. doi: 10.1038/22124.

Schilling, S., Rahfeld, J.U., Lues, I., and Lemere, C.A. (2018). Passive Abeta Immunotherapy: Current Achievements and Future Perspectives. Molecules *23*. doi: 10.3390/molecules23051068.

Scholtzova, H., Kascsak, R.J., Bates, K.A., Boutajangout, A., Kerr, D.J., Meeker, H.C., Mehta, P.D., Spinner, D.S., and Wisniewski, T. (2009). Induction of toll-like receptor 9 signaling as a method for ameliorating Alzheimer's disease-related pathology. The Journal of neuroscience : the official journal of the Society for Neuroscience *29*, 1846-1854. doi: 10.1523/JNEUROSCI.5715-08.2009.

Sevigny, J., Chiao, P., Bussiere, T., Weinreb, P.H., Williams, L., Maier, M., Dunstan, R., Salloway, S., Chen, T., Ling, Y., *et al.* (2016). The antibody aducanumab reduces Abeta plaques in Alzheimer's disease. Nature *537*, 50-56. doi: 10.1038/nature19323.

Sharma, K., Schmitt, S., Bergner, C.G., Tyanova, S., Kannaiyan, N., Manrique-Hoyos, N., Kongi, K., Cantuti, L., Hanisch, U.K., Philips, M.A., *et al.* (2015). Cell type- and brain region-resolved mouse brain proteome. Nature neuroscience *18*, 1819-1831. doi: 10.1038/nn.4160.

Shi, Y., and Holtzman, D.M. (2018). Interplay between innate immunity and Alzheimer disease: APOE and TREM2 in the spotlight. Nat Rev Immunol *18*, 759-772. doi: 10.1038/s41577-018-0051-1.

Sims, R., van der Lee, S.J., Naj, A.C., Bellenguez, C., Badarinarayan, N., Jakobsdottir, J., Kunkle, B.W., Boland, A., Raybould, R., Bis, J.C., *et al.* (2017). Rare coding variants in PLCG2, ABI3, and TREM2 implicate microglial-mediated innate immunity in Alzheimer's disease. Nat Genet *49*, 1373-1384. doi: 10.1038/ng.3916.

Solito, E., and Sastre, M. (2012). Microglia function in Alzheimer's disease. Front Pharmacol *3*, 14. doi: 10.3389/fphar.2012.00014.

Thygesen, C., Ilkjaer, L., Kempf, S.J., Hemdrup, A.L., von Linstow, C.U., Babcock, A.A., Darvesh, S., Larsen, M.R., and Finsen, B. (2018). Diverse Protein Profiles in CNS Myeloid Cells and CNS Tissue From Lipopolysaccharide- and Vehicle-Injected APPSWE/PS1DeltaE9 Transgenic Mice Implicate Cathepsin Z in Alzheimer's Disease. Front Cell Neurosci *12*, 397. doi: 10.3389/fncel.2018.00397.

Tusher, V.G., Tibshirani, R., and Chu, G. (2001). Significance analysis of microarrays applied to the ionizing radiation response. Proceedings of the National Academy of Sciences of the United States of America *98*, 5116-5121. doi: 10.1073/pnas.091062498.

Tyanova, S., Temu, T., Sinitcyn, P., Carlson, A., Hein, M.Y., Geiger, T., Mann, M., and Cox, J. (2016). The Perseus computational platform for comprehensive analysis of (prote)omics data. Nat Methods *13*, 731-740. doi: 10.1038/nmeth.3901.

Ulrich, J.D., Ulland, T.K., Mahan, T.E., Nystrom, S., Nilsson, K.P., Song, W.M., Zhou, Y., Reinartz, M., Choi, S., Jiang, H., *et al.* (2018). ApoE facilitates the microglial response to amyloid plaque pathology. J Exp Med *215*, 1047-1058. doi: 10.1084/jem.20171265.

Van Acker, Z.P., Bretou, M., and Annaert, W. (2019). Endo-lysosomal dysregulations and late-onset Alzheimer's disease: impact of genetic risk factors. Molecular neurodegeneration *14*, 20. doi: 10.1186/s13024-019-0323-7.

Wang, Y., Cella, M., Mallinson, K., Ulrich, J.D., Young, K.L., Robinette, M.L., Gilfillan, S., Krishnan, G.M., Sudhakar, S., Zinselmeyer, B.H., *et al.* (2015). TREM2 lipid sensing sustains the microglial response in an Alzheimer's disease model. Cell *160*, 1061-1071. doi: 10.1016/j.cell.2015.01.049.

Wilcock, D.M., Rojiani, A., Rosenthal, A., Levkowitz, G., Subbarao, S., Alamed, J., Wilson, D., Wilson, N., Freeman, M.J., Gordon, M.N., *et al.* (2004). Passive amyloid immunotherapy clears amyloid and transiently activates microglia in a transgenic mouse model of amyloid deposition. The Journal of neuroscience : the official journal of the Society for Neuroscience *24*, 6144-6151. doi: 10.1523/JNEUROSCI.1090-04.2004.

Wildsmith, K.R., Holley, M., Savage, J.C., Skerrett, R., and Landreth, G.E. (2013). Evidence for impaired amyloid beta clearance in Alzheimer's disease. Alzheimer's research & therapy *5*, 33. doi: 10.1186/alzrt187.

Wisniewski, J.R., Zougman, A., Nagaraj, N., and Mann, M. (2009). Universal sample preparation method for proteome analysis. Nat Methods *6*, 359-362. doi: 10.1038/nmeth.1322.

Xiang, X., Werner, G., Bohrmann, B., Liesz, A., Mazaheri, F., Capell, A., Feederle, R., Knuesel, I., Kleinberger, G., and Haass, C. (2016). TREM2 deficiency reduces the efficacy of immunotherapeutic amyloid clearance. EMBO molecular medicine *8*, 992-1004. doi: 10.15252/emmm.201606370.

Yamasaki, A., Eimer, S., Okochi, M., Smialowska, A., Kaether, C., Baumeister, R., Haass, C., and Steiner, H. (2006). The GxGD motif of presenilin contributes to catalytic function and substrate identification of gamma-secretase. The Journal of neuroscience : the official journal of the Society for Neuroscience *26*, 3821-3828. doi: 10.1523/JNEUROSCI.5354-05.2006.

Yin, Z., Raj, D., Saiepour, N., Van Dam, D., Brouwer, N., Holtman, I.R., Eggen, B.J.L., Moller, T., Tamm, J.A., Abdourahman, A., *et al.* (2017). Immune hyperreactivity of Abeta plaque-associated microglia in Alzheimer's disease. Neurobiology of aging *55*, 115-122. doi: 10.1016/j.neurobiolaging.2017.03.021.

Yuan, P., Condello, C., Keene, C.D., Wang, Y., Bird, T.D., Paul, S.M., Luo, W., Colonna, M., Baddeley, D., and Grutzendler, J. (2016). TREM2 Haplodeficiency in Mice and Humans Impairs the Microglia Barrier Function Leading to Decreased Amyloid Compaction and Severe Axonal Dystrophy. Neuron *92*, 252-264. doi: 10.1016/j.neuron.2016.09.016.

Zabala, A., Vazquez-Villoldo, N., Rissiek, B., Gejo, J., Martin, A., Palomino, A., Perez-Samartin, A., Pulagam, K.R., Lukowiak, M., Capetillo-Zarate, E., *et al.* (2018). P2X4 receptor controls microglia activation and favors remyelination in autoimmune encephalitis. EMBO molecular medicine *10*. doi: 10.15252/emmm.201708743.

Zuroff, L., Daley, D., Black, K.L., and Koronyo-Hamaoui, M. (2017). Clearance of cerebral Abeta in Alzheimer's disease: reassessing the role of microglia and monocytes. Cell Mol Life Sci *74*, 2167-2201. doi: 10.1007/s00018-017-2463-7.

Figure Legends

Figure 1. **Quantitative proteomics of acutely isolated microglia.** Volcano plots of APPPS1 and APP-KI *versus* WT microglia at 1 (**A** and **B**), 3 (**C** and **D**), 6 (**E** and **F)** and 12 (**G** and **H)** months of age. The minus log10 transformed p-value is plotted against the log2 transformed LFQ ratios. A permutation based FDR estimation was applied which is visualized as hyperbolic curves. Proteins with log2 LFQ ratio lower than -0.5 or higher than +0.5 with a p-value less than 0.05 which remain significantly changed after FDR correction are indicated as red circles. Non-significantly changed proteins are indicated as blue circles. Individual proteins are marked with their gene names.

Figure 2. APPPS1 microglia display earlier proteomic changes compared to APP-KI microglia. **A**. Profile plots of APPPS1 and APP-KI *versus* WT microglia at 1, 3, 6, and 12 months of age. Lines connect the average log2 fold changes of each protein at the different time points. Regulated proteins were grouped according to three profiles: significantly increased or decreased after FDR correction (log2 FC > 0.5 or < -0.5; $p < 0.05$; FDR significant) at 3, 6, and 12 months, only at 3 and 6 months, or only at 12 months. Proteins that fulfill these criteria are indicated as red and blue lines for increased and decreased abundance, respectively. Selected up- or down-regulated proteins are indicated with magenta and cyan. Proteins that were regulated at 3, 6, and 12 months in APPPS1 mice as well as at 6 and 12, or only at 12 months in APP-KI mice were annotated as early MARPs. Proteins that were regulated at 6 and 12 months in APPPS1 as well as at 6 and 12, or only at 12 months in APP-KI mice were annotated as middle MARPs. Proteins that were regulated at 12 months in APPPS1 and APP-KI mice were annotated as advanced MARPs. Heatmaps show the log2 fold changes of the top 74 up- or down-regulated proteins for early (**B**), middle (**C**) and advanced (**D**) MARPs and are compared to the log2 fold changes of related transcripts of DAM and homeostatic microglia (Keren-Shaul et al., 2017), indicated with K-S. Crosses indicate missing values.

Figure 3. Gene ontology enrichment cluster analysis for biological process (BP) of MARPs. Bar graphs show the clustering of early MARPs (**A**), middle MARPs (**B**) and advanced MARPs (**C**) for BP. Up- and down-regulated proteins were analyzed separately using the web-based software tool DAVID 6.8 with all consistently quantified proteins (5500) as an individual background. Significantly enriched clusters (Enrichment Score > 1.301) for up-and down-regulated proteins are indicated in blue and red, respectively.

Figure 4. Microglial CLEC7a is prominently up-regulated in 3 month old APPPS1 mice. Immunohistochemical analysis of CLEC7a (red) revealed an increased abundance of this early MARP in IBA1 positive (green) APPPS1 microglia surrounding Aβ plaques (magenta) that is less prominent in APP-KI microglia. CLEC7a was barely detected in WT microglia. Hoechst was used for nuclear staining (blue). Boxed regions in upper panels (scale bar: 50 µm) are shown with a higher magnification in lower panels (scale bar: 10 µm).

Figure 5. Microglial CLEC7a is increased in both AD mouse models at 12 months of age. Immunohistochemical analysis showed an up-regulation of CLEC7a (red) in IBA1 positive (green) APPPS1 and APP-KI microglia surrounding Aβ plaques (magenta), compared to WT where CLEC7a was barely detected. Hoechst was used for nuclear staining (blue). Boxed regions in upper panels (scale bar: 50 µm) are shown with a higher magnification in lower panels (scale bar: 10 µm).

Figure 6. Microglial TMEM119 is down-regulated in both AD mouse models at 12 months of age. Immunohistochemical analysis of TMEM119 (red) shows a broad coverage signal of this homeostatic marker in IBA1 positive (green) WT microglia. In the APPPS1 and APP-KI mice, TMEM119 signal is reduced in IBA1 positive microglia surrounding Aβ plaques (magenta). Of note, increased TMEM119 signal was often found in the core of amyloid plaques in APPPS1 and APP-KI mice. Hoechst was used for nuclear staining (blue). Boxed regions in upper panels (scale bar: 50 µm) are shown with a higher magnification in lower panels (scale bar: 10 µm) and illustrate reduced levels of TMEM119 in plaque associated microglia.

Figure 7. **APPPS1 Aβ plaques display a higher content of fibrillar Aβ compared to APP-KI plaques**. **A**. Immunohistochemical analysis showing total Aβ (green), fibrillar Aβ (ThR, red) and microglia (IBA1, magenta) in both mouse models at 3, 6 and 12 months of age. Hoechst was used for nuclear staining (blue). Scale bar: 100 µm **B**. Western blot analysis of insoluble Aβ at 3, 6 and 12 months of age confirms increased levels of fibrillar Aβ in APPPS1 compared to APP-KI mice.

Figure 8. **Fibrillar Aβ triggers higher microglial recruitment in 3 month old APPPS1 mice and correlates with a phagocytic impairment. A**. Representative picture of IBA1 positive (green) microglia polarized towards the fibrillar Aβ core (ThR, red, white arrow), rather than the surrounding

plaque halo (magenta) in 3 month old APPPS1 and APP-KI mice. Hoechst (HOE) was used for nuclear staining (blue). Yellow arrows indicate intracellular fibrillar Aβ within APPPS1 microglia. Scale bar: 10 µm. **B**. Quantification of IBA1 positive cells recruited to amyloid plaques in 3 month old APPPS1 and APP-KI mice. Microglial numbers are normalized to the plaque area. **C**. Quantification of plaque size in 3 month old APPPS1 and APP-KI mice. **D**. Imunohistochemical analysis of IBA1 (green) and CD68 (red) positive microglial cells recruited to Aβ plaques (magenta) in 3 month old APPPS1 and APP-KI mice. Hoechst was used for nuclear staining (blue). Scale bar: 20 µm. **E**. Quantification of CD68 coverage in 3 month old APPPS1 and APP-KI mice. CD68 coverage is normalized to the plaque area. **F**. Quantification of CD68 coverage per microglia in 3 month old APPPS1 and APP-KI mice. CD68 coverage is normalized to the number of IBA1 positive cells recruited to amyloid plaque. **G**. Immunohistochemical analysis of dystrophic neurites detected using an antibody against APP (green) in 3 month old APPPS1 and APP-KI mice. ThR was used to detect fibrillar Aβ plaque core (red) and the whole Aβ plaque was visualized using an antibody against Aβ (magenta). Hoechst was used for nuclear staining (blue). Scale bar: 20 µm. **H**. Quantification of area covered by dystrophic neurites in 3 month old APPPS1 and APP-KI mice. In **B**, **C**, **E**, **F** and **H**, represented values are expressed as the mean of n=3 mice per genotype ± SD (*P < 0.05; **P < 0.01, unpaired two-tailed Student's T-test; n.s: not significant). **I.** Mean Fluorescence Intensity (MFI) of *E.coli*-pHrodo signal within the CD11b positive cells in 3 and 6 month old APPPS1, APP-KI and WT mice. CytoD was used to inhibit phagocytosis and serves as a negative control. a.u.: arbitrary units. **J**. Percentage of CD11b and *E.coli*-pHrodo double positive cells from the total CD11b positive population. In **I** and **J**, values for the 3 month old group are expressed as the mean of n=3 mice per genotype ± SD from three independent experiments and for the 6 month old group as the mean of n=2 mice per genotype ± SD from two independent experiments (***P < 0.001, Two-way ANOVA, Dunnett's multiple comparison test; n.s: not significant).

Supplementary Figure Legends

Suppl. Figure 1. Quality control of microglial isolation using MACS. FACS analysis of the CD11b-enriched (**A**) and CD11b-depleted fraction (**B**). Propidium Iodide (PI) was used to analyze cell viability (PI negative fraction).

Suppl. Figure 2. **Improvement of the data acquisition method for quantitative proteomics of microglia. A**. Workflow of the proteomic analysis. Microglia were acutely isolated using the CD11b MACS system. Protein lysates were subjected to tryptic digestion followed by quantitative LC-MS/MS analysis. APPPS1 microglia samples were first measured using DDA to generate a spectral library required for DIA analysis. Afterwards, both APPPS1 and APPKI microglia were measured using DIA and data was subjected to further bioinformatics analysis. **B**. Distribution of quantified proteins with DDA and DIA. The number of quantified proteins is plotted against the log10 transformed iBAQ (intensity based absolute quantification) values with a bin size of 0.25. The iBAQ values are an estimate of the relative molar abundance of a protein within the sample. The number of consistently quantified proteins per bin for DDA and DIA are indicated in blue and red, respectively. Proteins that were only quantified with DDA or DIA are colored in light blue and orange, respectively. The single values are connected with dashed lines for better visibility. Please note that DIA provides additional quantifications for low abundant proteins. Hereby, DIA extends the dynamic range for protein quantification by almost one order of magnitude. **C**. Number of relatively quantified proteins between APPPS1 and WT microglia for 1, 3, 6, and 12 months with DDA (blue) and DIA (red). Only proteins that were consistently quantified in all APPPS1 and WT samples per age group were counted. Please note that DIA provides between 24 and 35% additional quantifications per age group. **D**. The comparison of relatively quantified proteins of APPPS1 and APP-KI *versus* WT at 12 months shows a large overlap of 93.5% indicating a very consistent quantification.

Suppl. Figure 3. Aβ pathology in 3, 6 and 12 month old APPPS1 and APP-KI mice. Immunohistochemical analysis of Aβ load (NAB228, green) in APPPS1 and APP-KI mice. Hoechst was used for nuclear staining (blue). Scale bar: 400 µm.

Suppl. Figure 4. Comparison of the early, middle and advanced MARPs in APPPS1 and APP-KI mice. A. A Venn diagram illustrates the classification of regulated proteins into early, middle and advanced MARPs. Proteins that were regulated at 3, 6, and 12 months in APPPS1 mice as well as at

6 and 12, or only at 12 months in APP-KI mice were annotated as early MARPs. Proteins that were regulated at 6 and 12 months in APPPS1 as well as at 6 and 12, or only at 12 months in APP-KI mice were annotated as middle MARPs. Proteins that were regulated at 12 months in APPPS1 and APP-KI mice were annotated as advanced MARPs. **B**. Correlation plot of log2 protein fold changes detected at 12 months for APPPS1 and APP-KI *versus* WT. The plot shows a significant correlation of proteomic changes at 12 months. Early, middle, and advanced MARPs are indicated in red, orange, and black circles with yellow filling, respectively. Selected proteins are annotated with their gene names. **C**. Comparison of our proteomic study with the single cell transcriptomics study (Keren-Shaul et al., 2017) reveals a modest overlap. A Venn diagram illustrates the comparison of quantified proteins in APPPS1 and APP-KI *versus* WT at 12 months and DAM and homeostatic microglial transcripts. Overall, 3348 common proteins and related transcripts were quantified. **D**. Biochemical validation of proteomic data was performed using Western blot analysis of microglial lysates from 12 month old mice. This analysis revealed an increased abundance of up-regulated MARPs APOE, TREM2, CD68 and FABP5 as well as a decreased abundance of the down-regulated MARP CSF1R in APPPS1 and APP-KI compared to WT microglia. Arrows indicate antibody-detected specific bands and asterisk indicates unspecific bands.

Suppl. Figure 5. Gene ontology enrichment cluster analysis for cellular component (CC) and molecular function (MF) of MARPs. The bar graphs show the clustering of early MARPs (**A**, **D**), middle MARPs (**B**, **E**) and advanced MARPs (**C**, **F**) for CC and MF. Up- and down-regulated proteins were analyzed separately using the web-based software tool DAVID 6.8 using all consistently quantified proteins (5500) as an individual background. Significantly enriched clusters (Enrichment Score > 1.301) for up- and down-regulated proteins are indicated in blue and red, respectively.

Suppl. Figure 6. Microglial TREM2 is prominently up-regulated in 3 month old APPPS1 mice. Immunohistochemical analysis of TREM2 (red) revealed an increased abundance in IBA1 positive (green) APPPS1 microglia surrounding Aβ plaques (magenta) that is less prominent in APP-KI microglia. Hoechst was used for nuclear staining (blue). Boxed regions in upper panels (scale bar: 50 µm) are shown with a higher magnification in lower panels (scale bar: 10 µm).

Suppl. Figure 7. Microglial APOE is prominently up-regulated in 3 month old APPPS1 mice. Immunohistochemical analysis of APOE (red) revealed an up-regulation in IBA1 positive (green)

APPPS1 microglia surrounding Aβ plaques (magenta) that is less prominent in APP-KI microglia. APOE could not be detected in WT microglia. Hoechst was used for nuclear staining (blue). Of note, astrocytic APOE immunoreactivity was also detected, particularly in the WT, reflecting its physiological expression. Yellow arrows indicate APOE positive microglia. Boxed regions in upper panels (scale bar: 50 µm) are shown with a higher magnification in lower panels (scale bar: 10 µm).

Suppl. Figure 8. Phagocytosis is impaired earlier in APPPS1 compared to APP-KI microglia. A. Histograms represent the fuorescence intensity of uptaken E.coli-pHrodo green particles within the CD11b positive population for every genotype and time point (3 and 6 months). Dashed lines indicate the mean fluorescence intensity (MFI) calculated with the geometric mean for each condition. **B**. FACS analysis representing the percentage of CD11b and E.coli-pHrodo positive cells out of the whole CD11b positive population for every genotype.

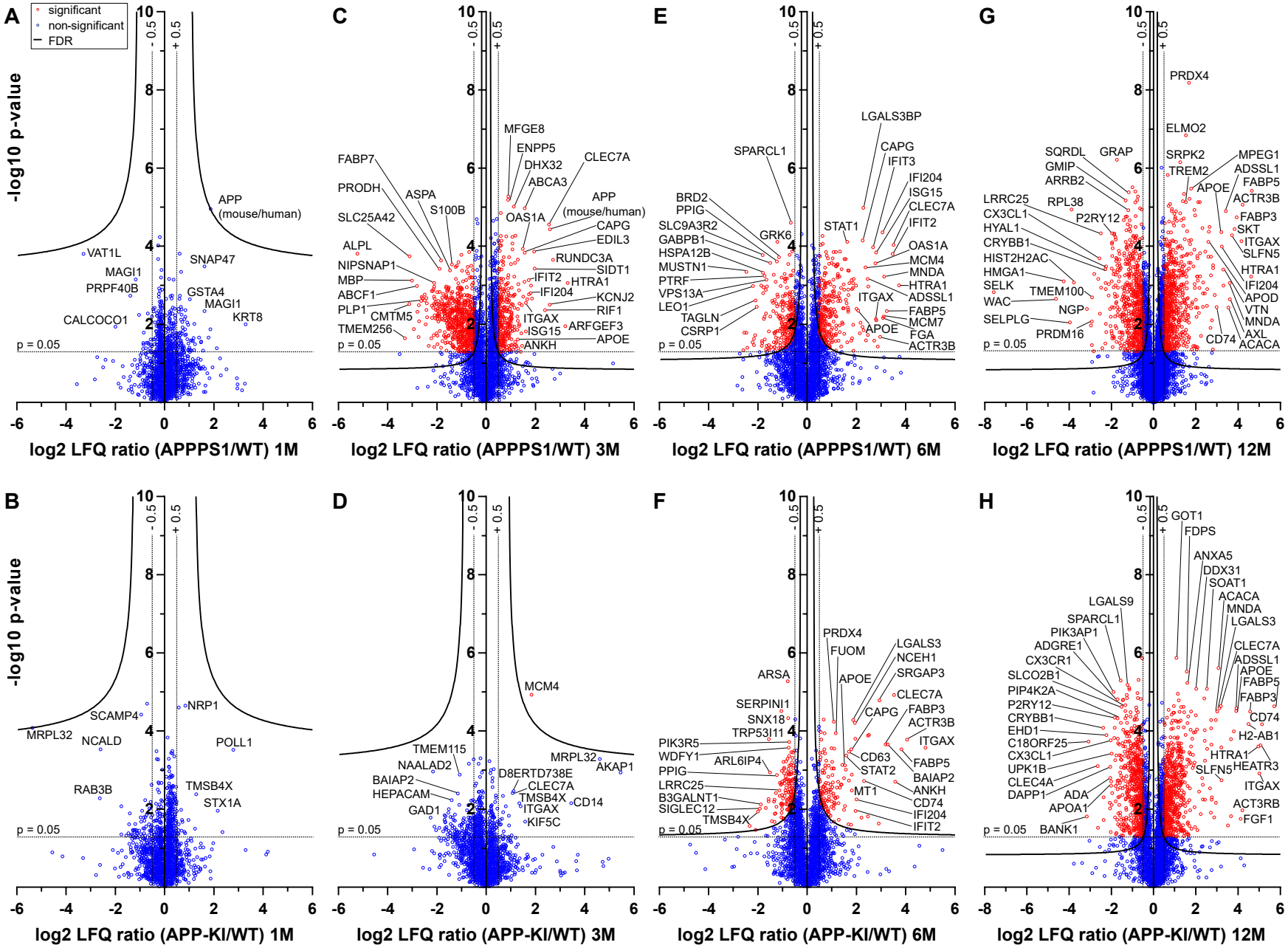
A
B
C
D
E
F
G
H
significant
non-significant
FDR
-log10 p-value
p = 0.05
log2 LFQ ratio (APPPS1/WT) 1M
log2 LFQ ratio (APP-KI/WT) 1M
log2 LFQ ratio (APPPS1/WT) 3M
log2 LFQ ratio (APP-KI/WT) 3M
log2 LFQ ratio (APPPS1/WT) 6M
log2 LFQ ratio (APP-KI/WT) 6M
log2 LFQ ratio (APPPS1/WT) 12M
log2 LFQ ratio (APP-KI/WT) 12M
APP (mouse/human)
VAT1L
MAGI1
PRPF40B
SNAP47
GSTA4
MAGI1
KRT8
CALCOCO1
SCAMP4
MRPL32
NCALD
NRP1
POLL1
RAB3B
TMSB4X
STX1A
FABP7
PRODH
ASPA
S100B
SLC25A42
ALPL
NIPSNAP1
MBP
ABCF1
PLP1
CMTM5
TMEM256
MFGE8
ENPP5
DHX32
CLEC7A
ABCA3
OAS1A
CAPG
EDIL3
RUNDC3A
SIDT1
IFIT2
HTRA1
IFI204
KCNJ2
RIF1
ITGAX
ISG15
ARFGEF3
ANKH
APOE
MCM4
TMEM115
NAALAD2
BAIAP2
HEPACAM
GAD1
D8ERTD738E
CLEC7A
TMSB4X
ITGAX
KIF5C
CD14
MRPL32
AKAP1
SPARCL1
BRD2
PPIG
SLC9A3R2
GABPB1
HSPA12B
MUSTN1
PTRF
VPS13A
LEO1
TAGLN
CSRP1
GRK6
LGALS3BP
CAPG
IFIT3
IFI204
ISG15
CLEC7A
IFIT2
STAT1
OAS1A
MCM4
MNDA
HTRA1
ITGAX
ADSSL1
FABP5
MCM7
FGA
APOE
ACTR3B
PRDX4
FUOM
ARSA
APOE
SERPINI1
SNX18
TRP53I11
PIK3R5
WDFY1
ARL6IP4
PPIG
LRRC25
B3GALNT1
SIGLEC12
TMSB4X
LGALS3
NCEH1
SRGAP3
CLEC7A
FABP3
ACTR3B
CAPG
ITGAX
CD63
FABP5
STAT2
BAIAP2
MT1
ANKH
CD74
IFI204
IFIT2
PRDX4
ELMO2
SQRDL
GRAP
GMIP
ARRB2
SRPK2
TREM2
APOE
MPEG1
ADSSL1
FABP5
ACTR3B
FABP3
SKT
ITGAX
SLFN5
HTRA1
IFI204
APOD
VTN
MNDA
AXL
ACACA
CD74
LRRC25
RPL38
CX3CL1
P2RY12
HYAL1
CRYBB1
HIST2H2AC
HMGA1
SELK
WAC
TMEM100
NGP
SELPLG
PRDM16
GOT1
FDPS
ANXA5
DDX31
SOAT1
ACACA
MNDA
LGALS3
CLEC7A
ADSSL1
APOE
FABP5
FABP3
CD74
H2-AB1
HTRA1
HEATR3
ITGAX
ACT3RB
FGF1
LGALS9
SPARCL1
PIK3AP1
ADGRE1
CX3CR1
SLCO2B1
PIP4K2A
P2RY12
CRYBB1
EHD1
C18ORF25
CX3CL1
UPK1B
CLEC4A
DAPP1
ADA
APOA1
SLFN5
BANK1

Fig 1

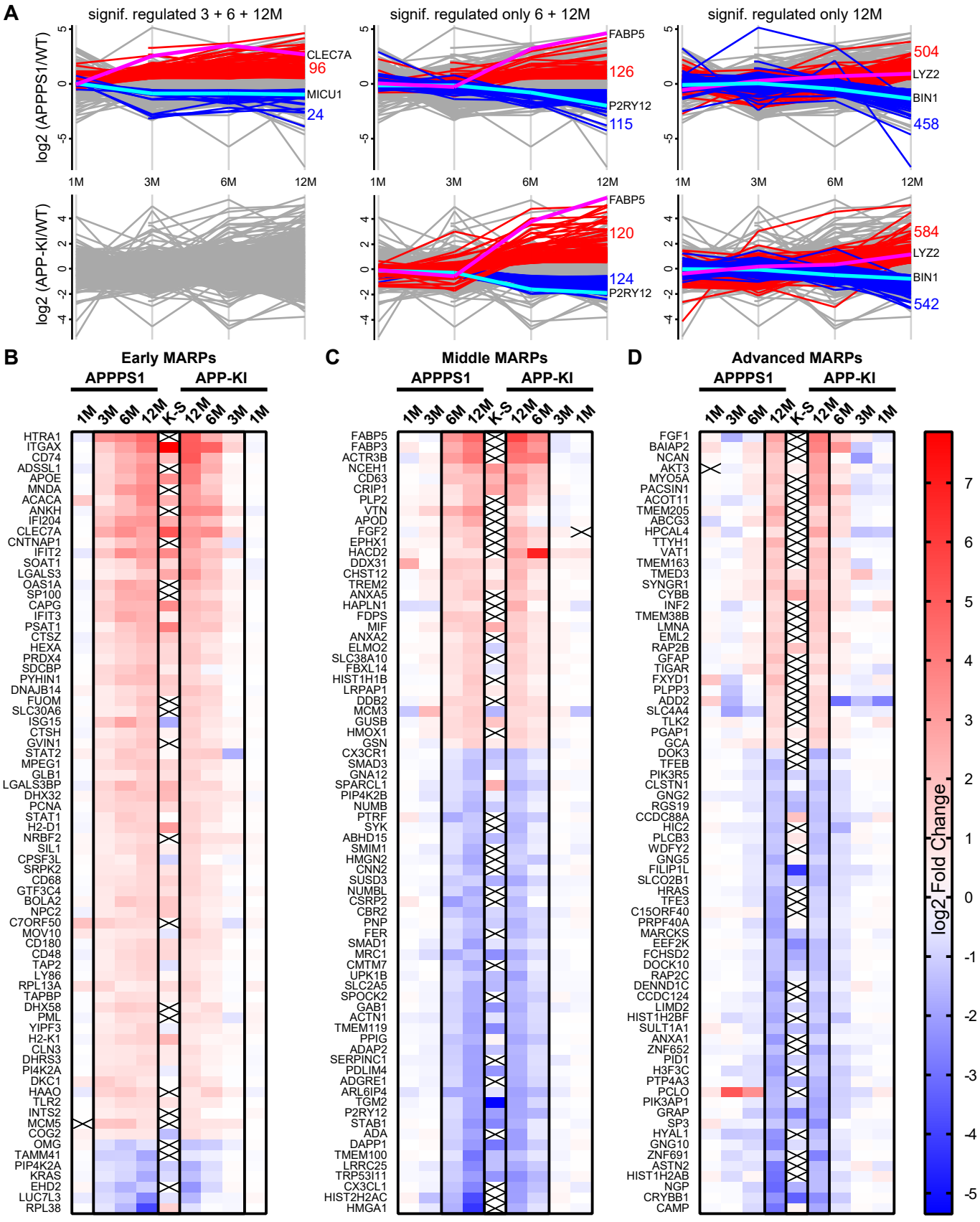

Fig 2

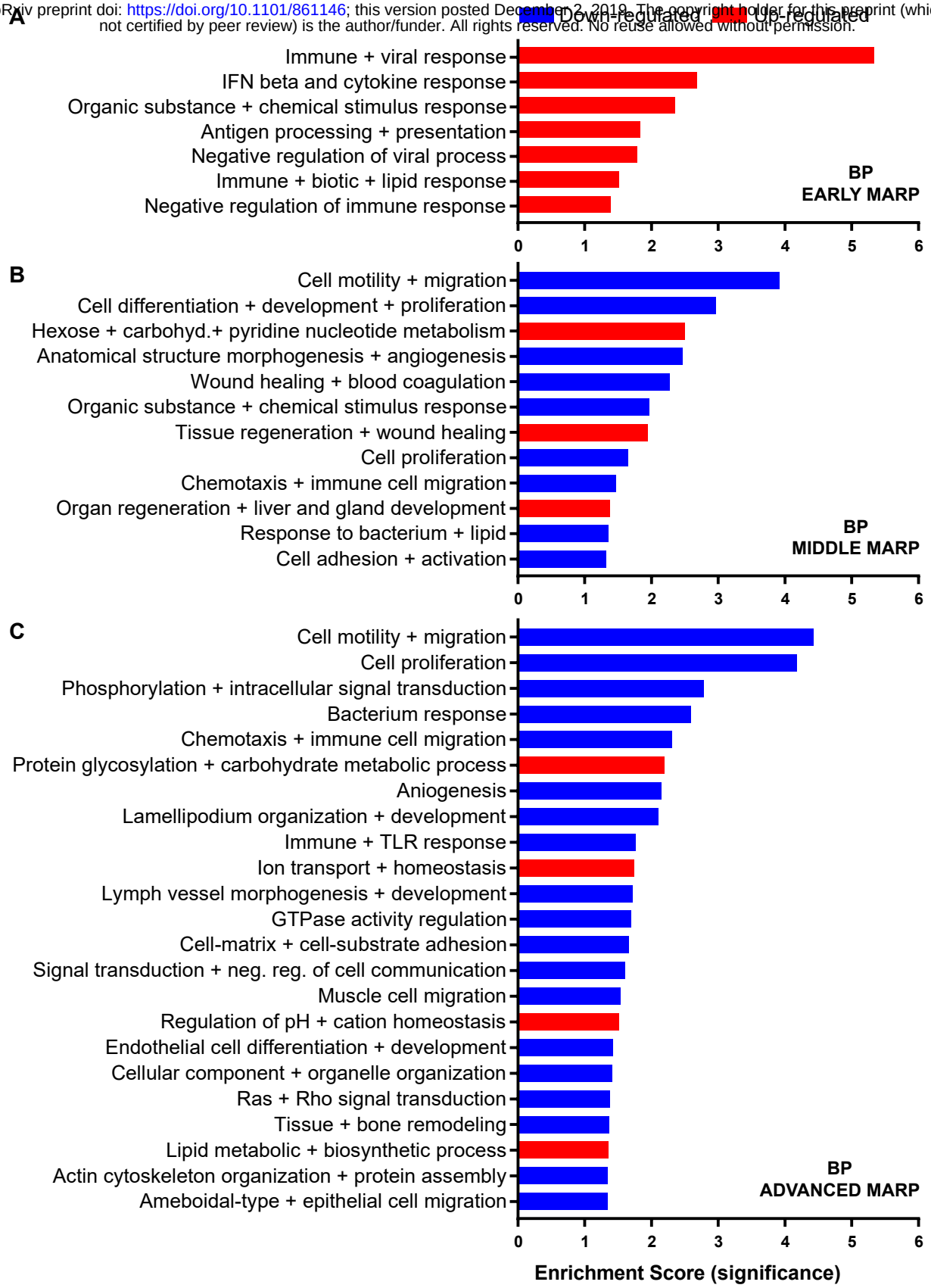

Fig 3

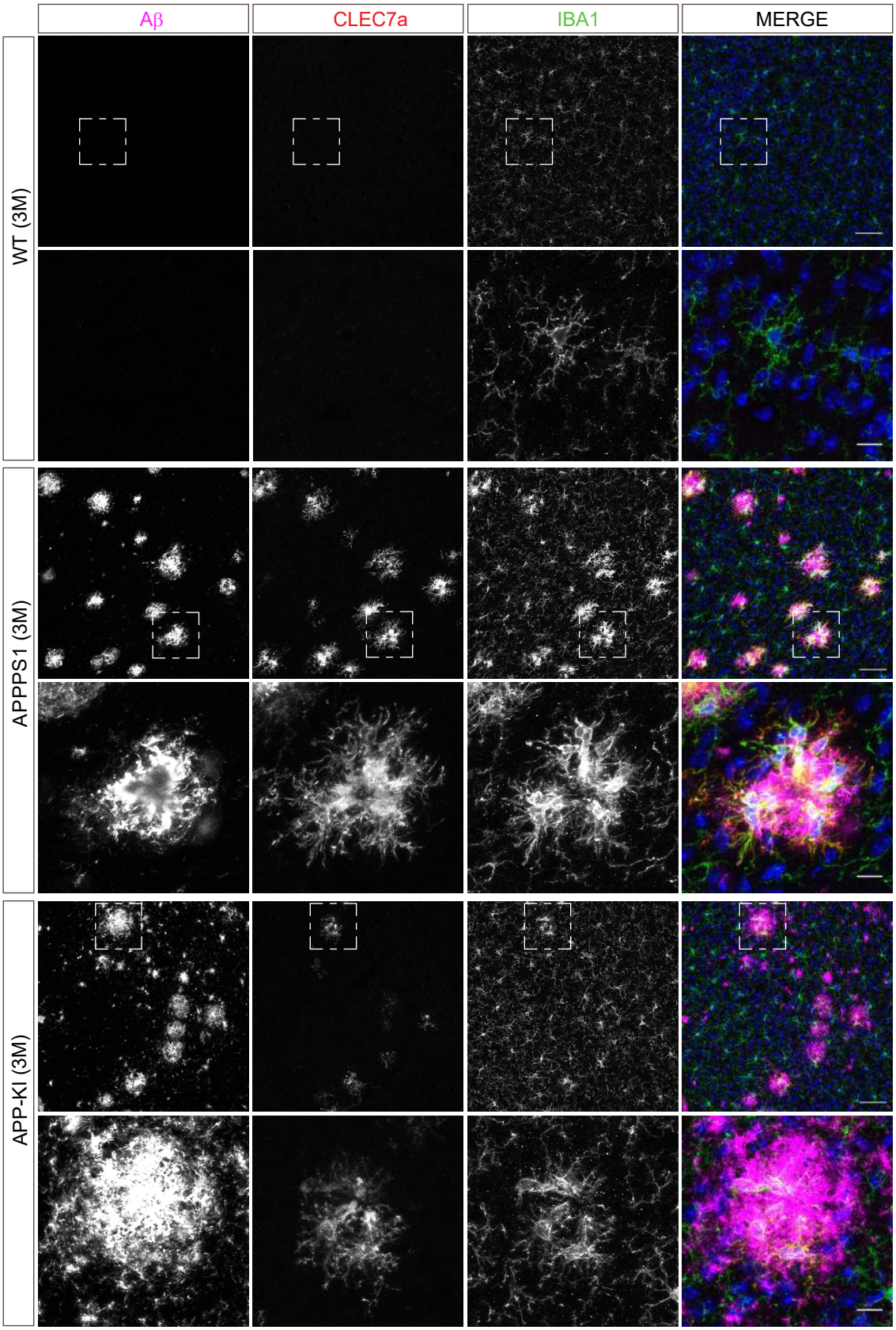

Fig 4

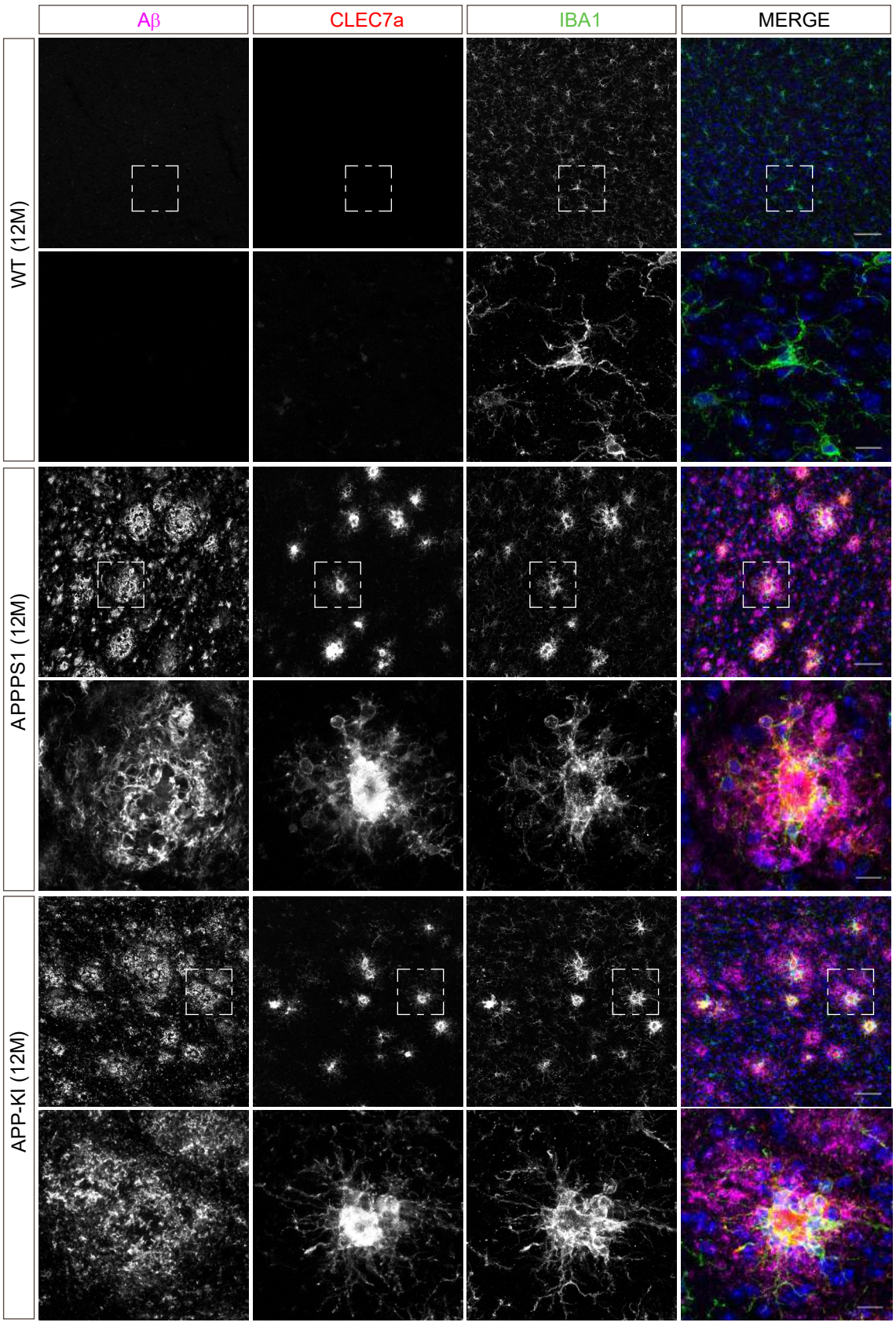

Fig 5

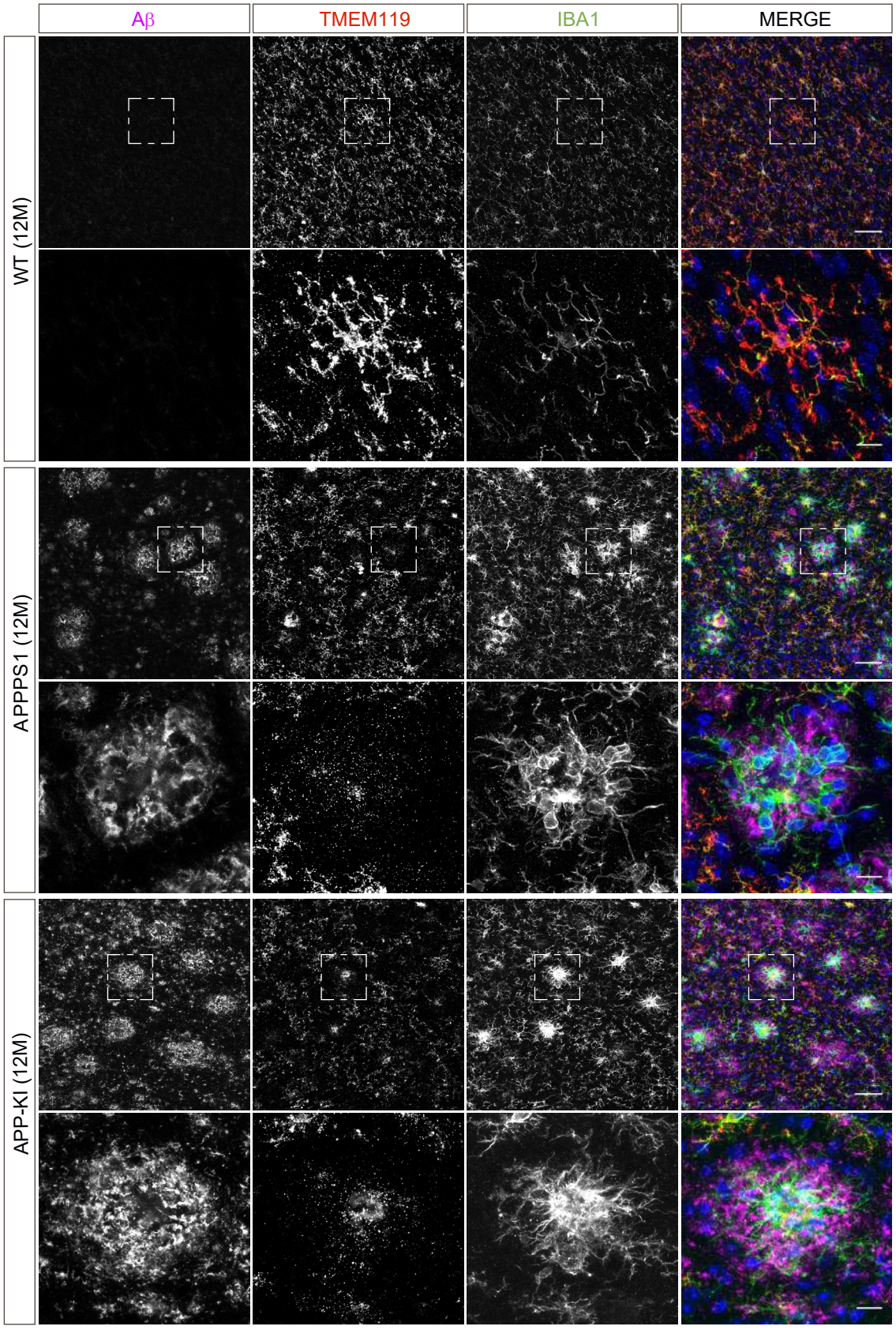

Fig 6

A

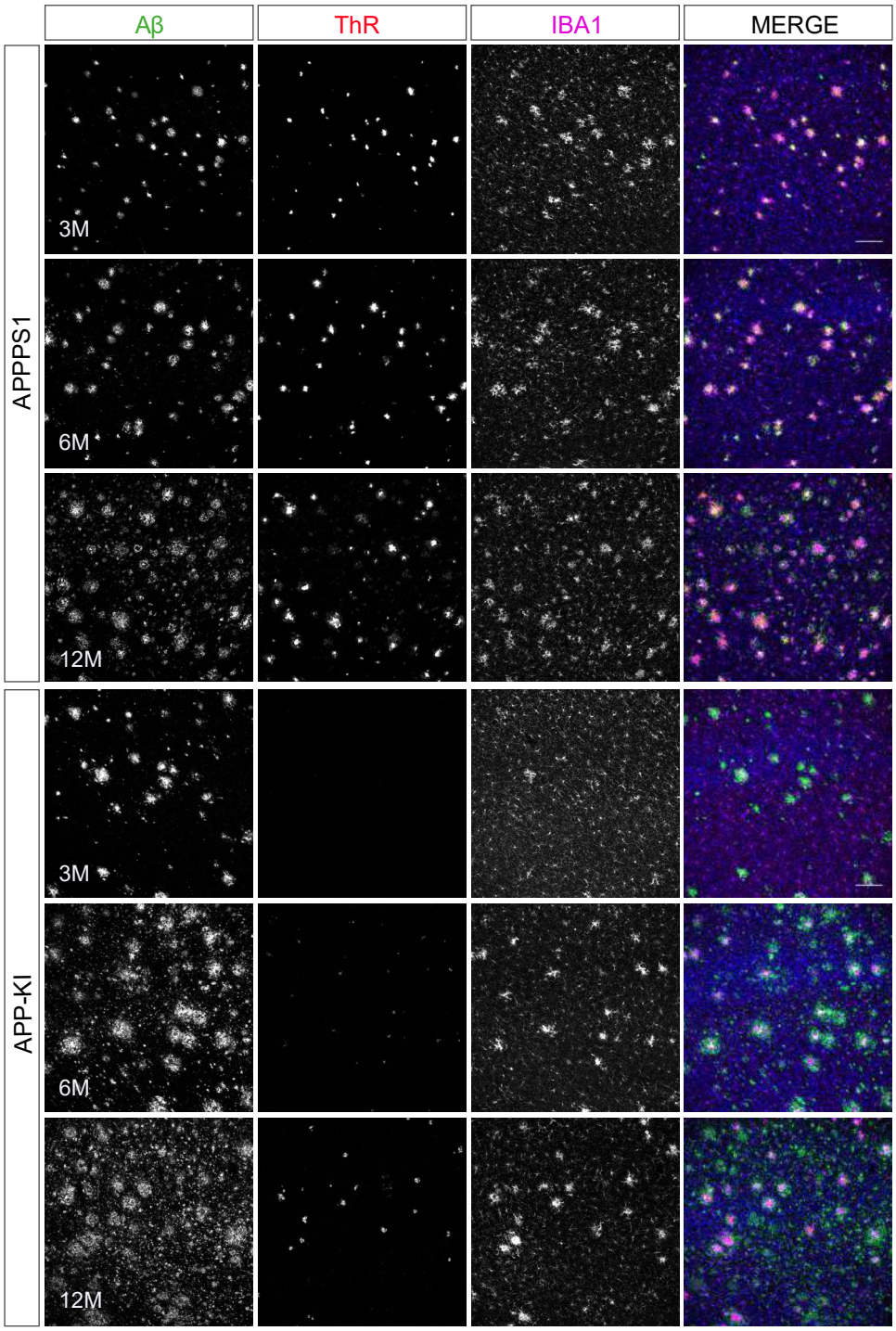

B

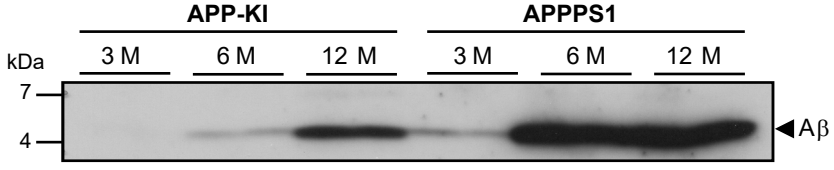

Fig 7

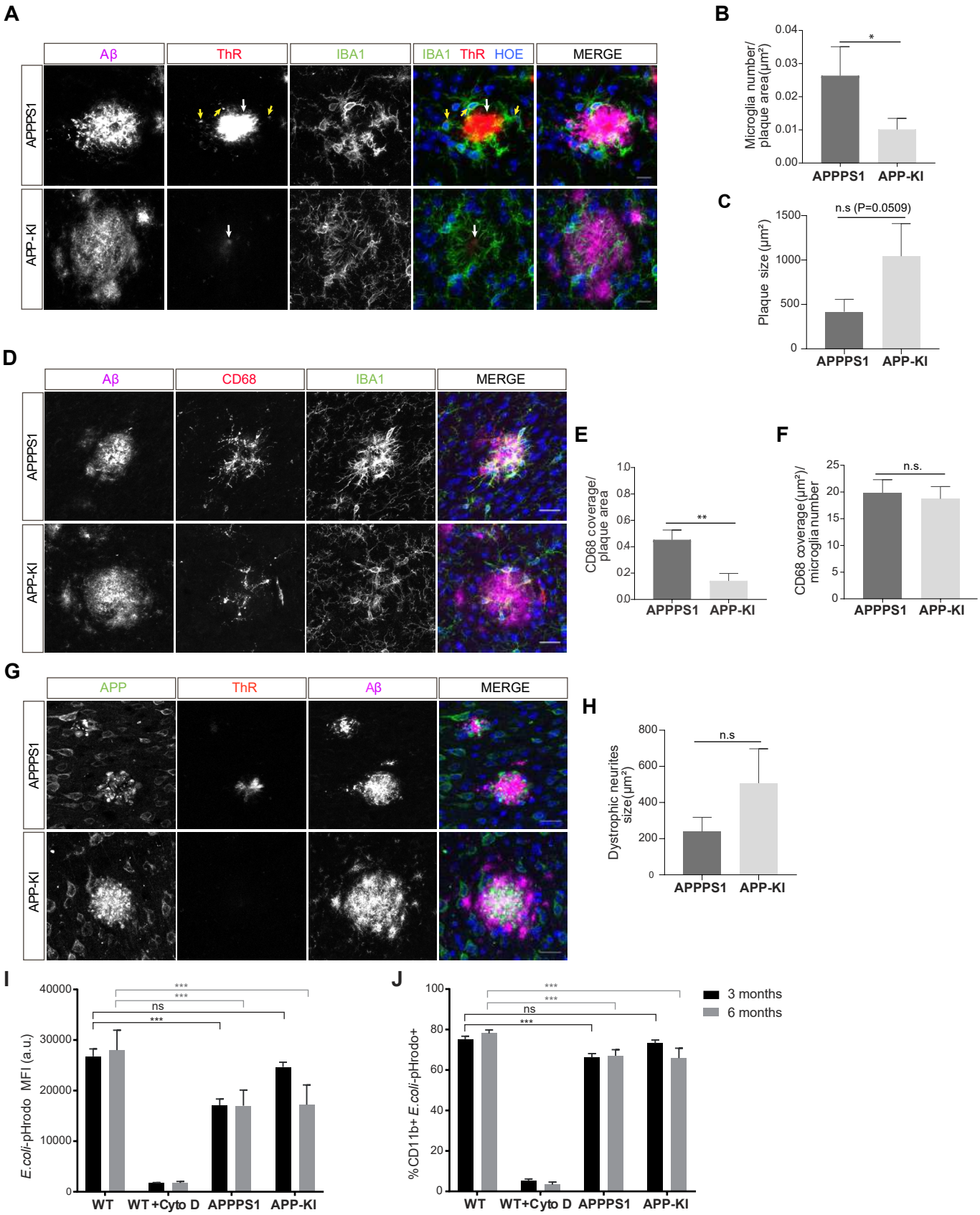

Fig 8

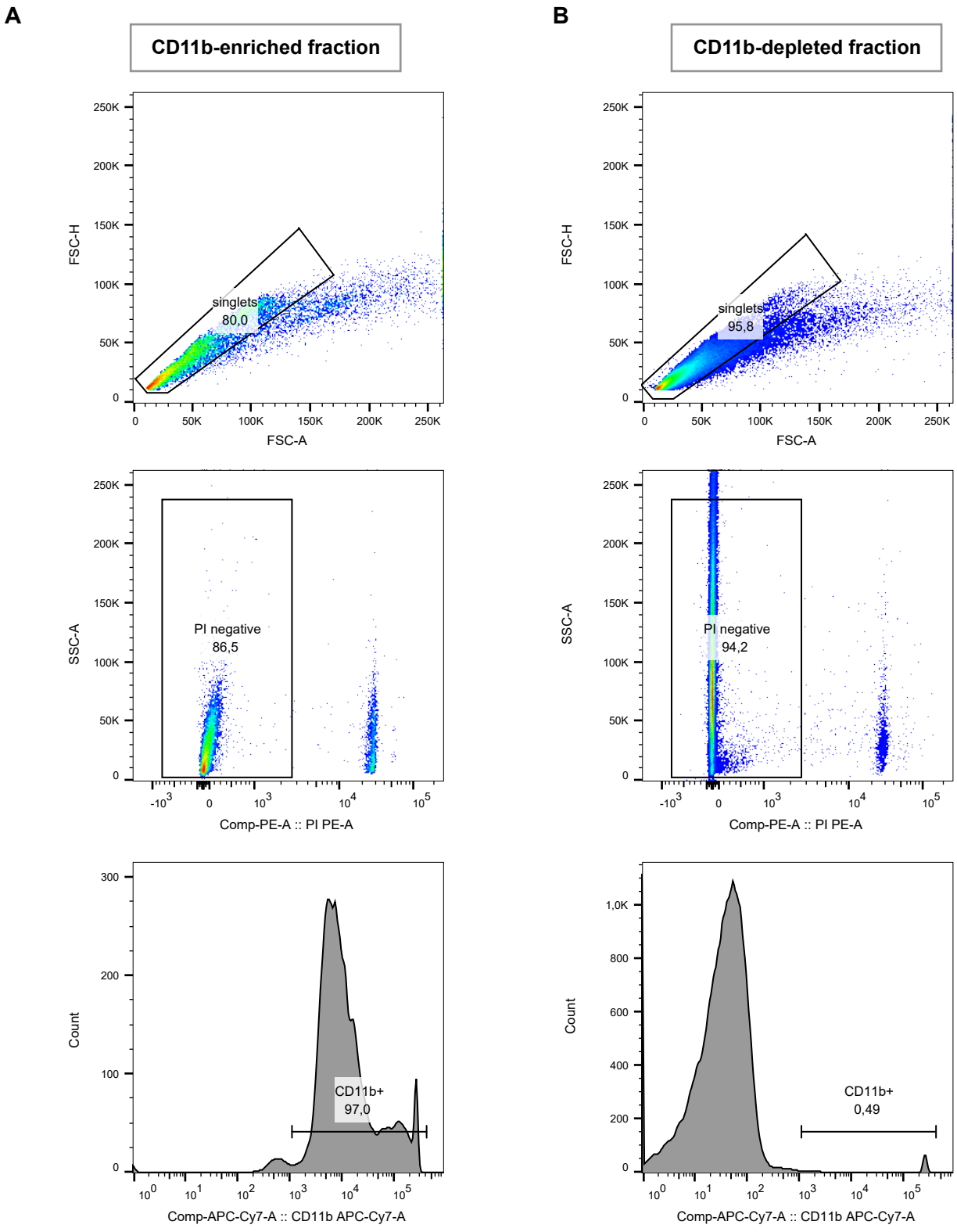

Suppl. Fig 1

A

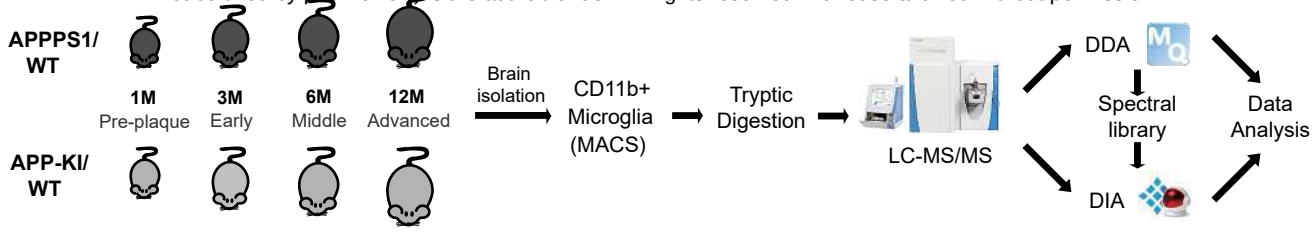

B

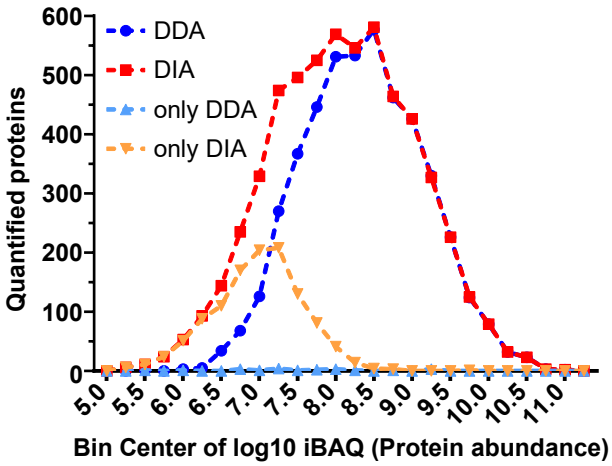

C

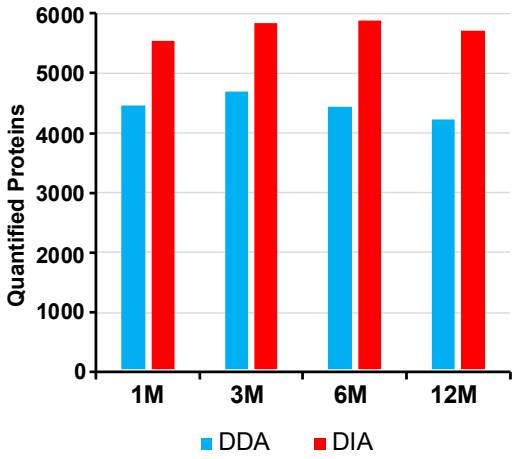

D

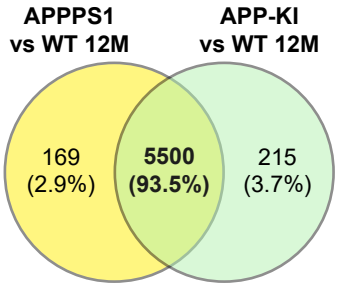

Suppl. Fig 2

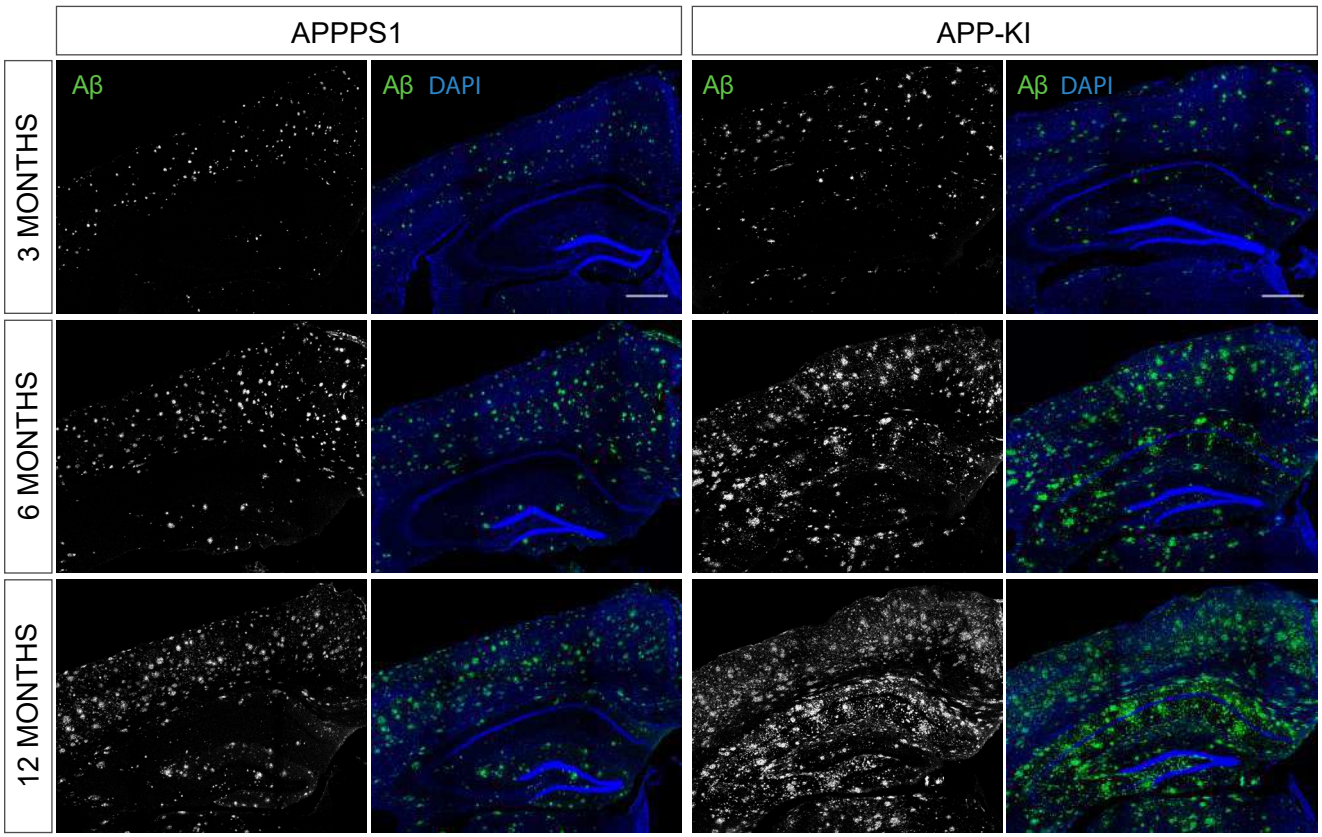

Suppl. Fig 3

A

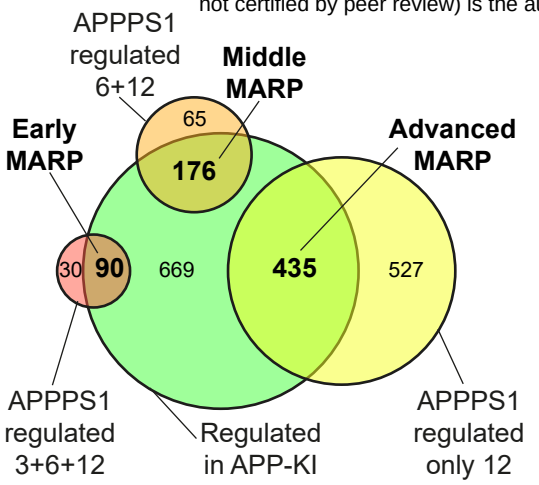

B

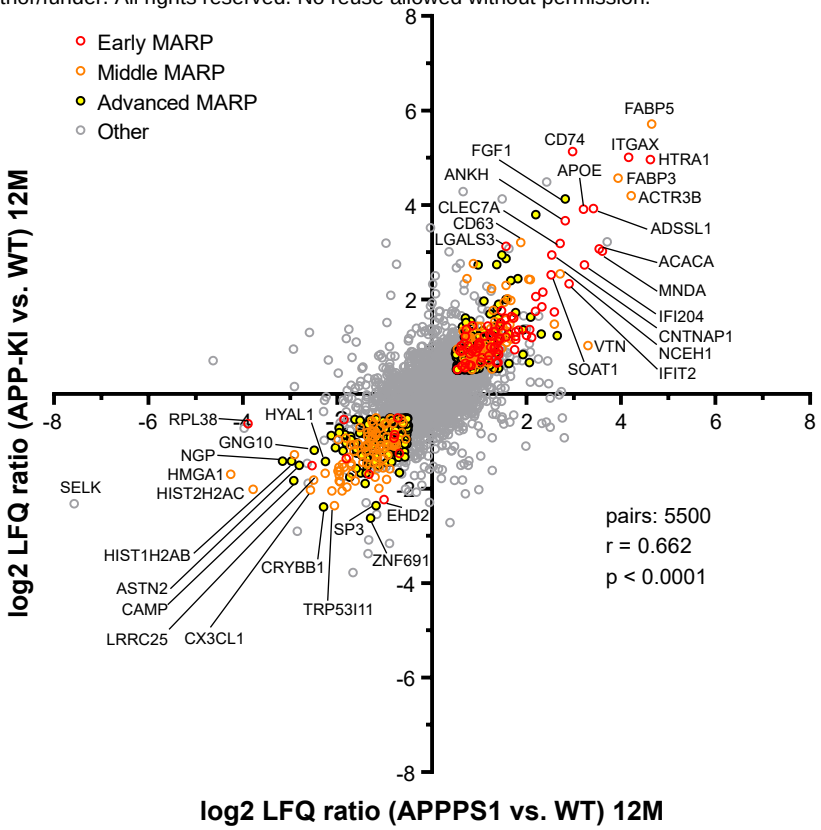

C

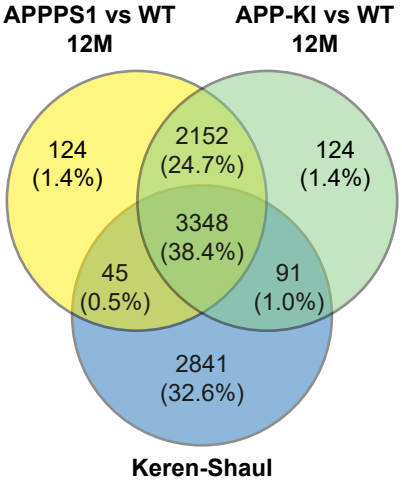

D

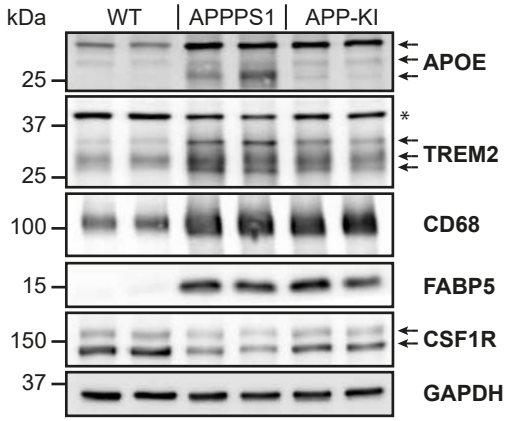

Suppl. Fig 4

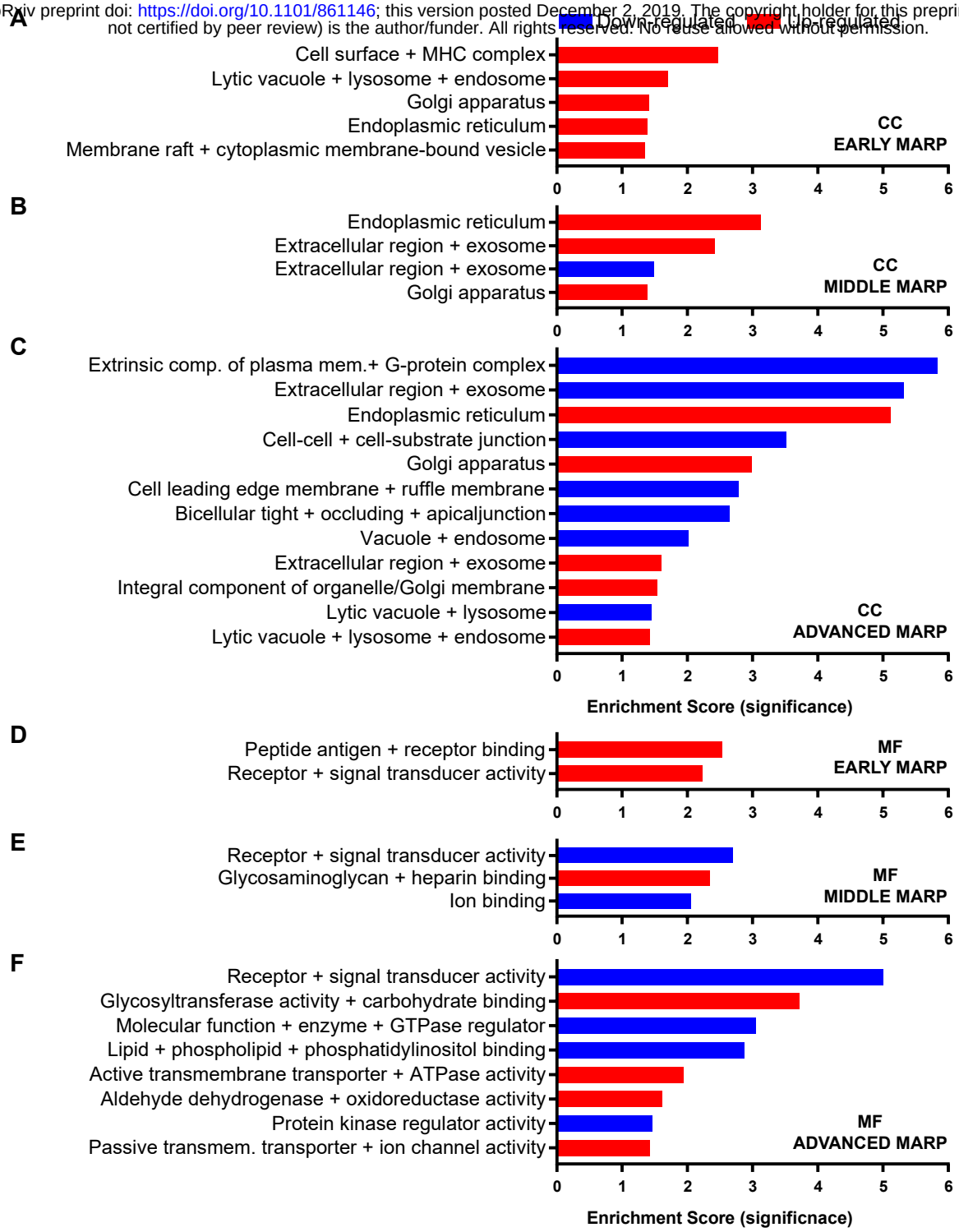

Suppl. Fig 5

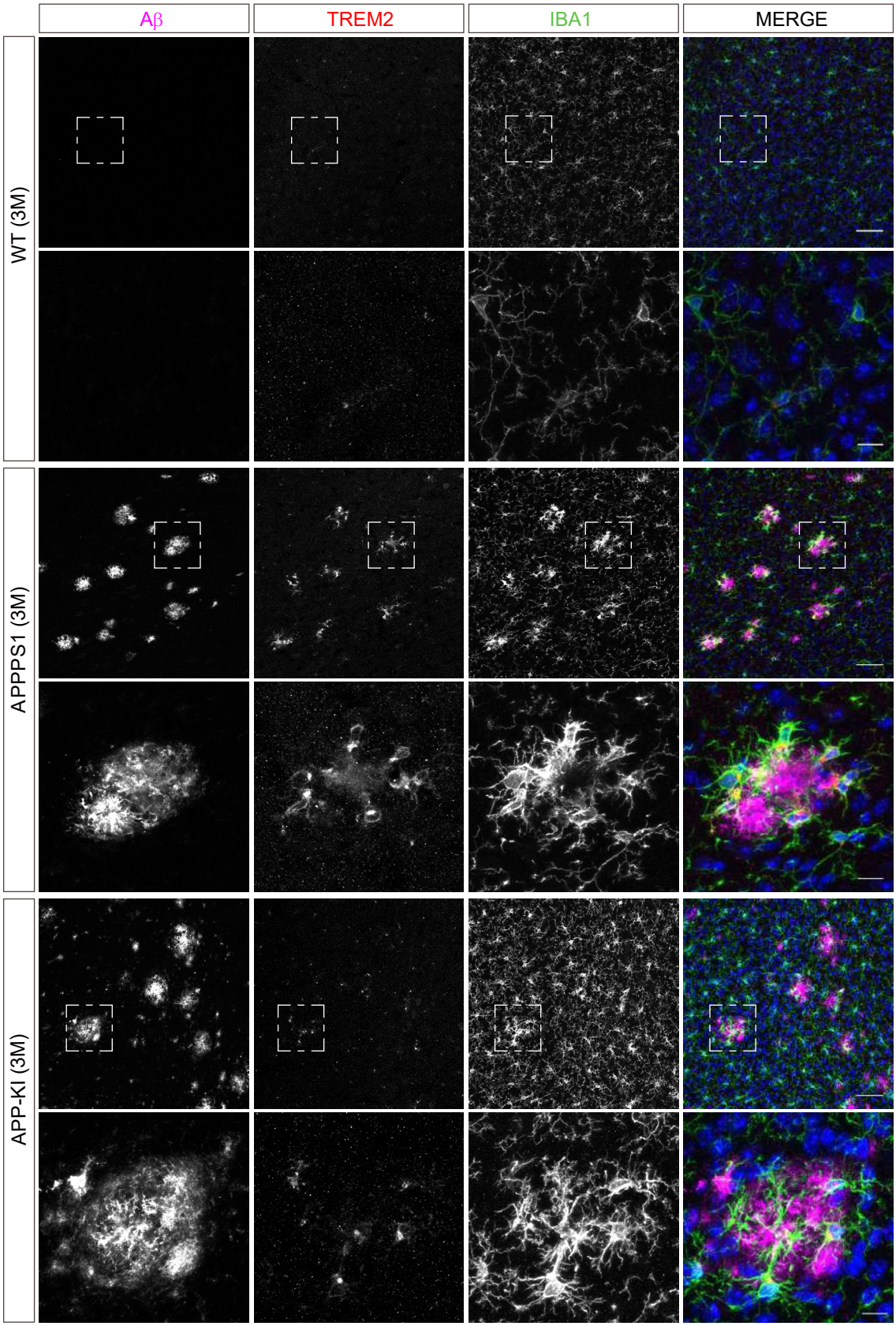

Suppl. Fig 6

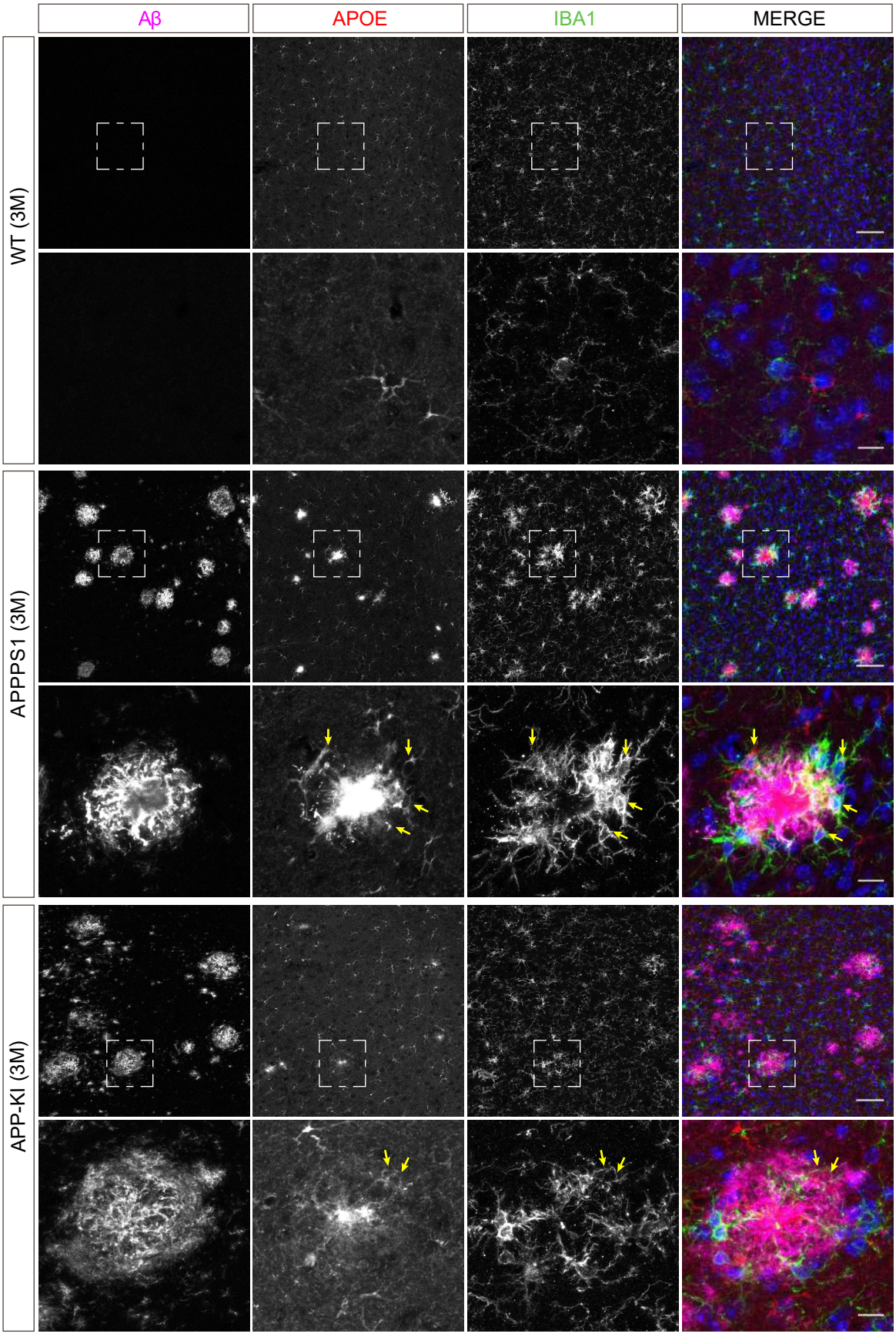

Suppl. Fig 7

A

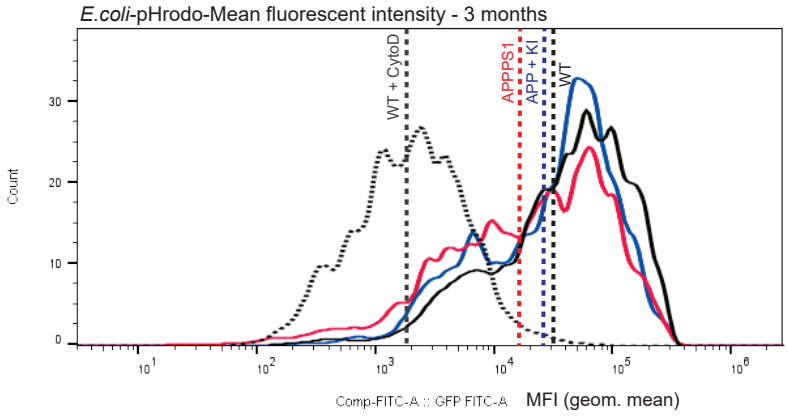

Sample (3M)	MFI (geom. mean)
WT	30298
WT + CytoD	1925
APPPS1	16365
APP + KI	24561

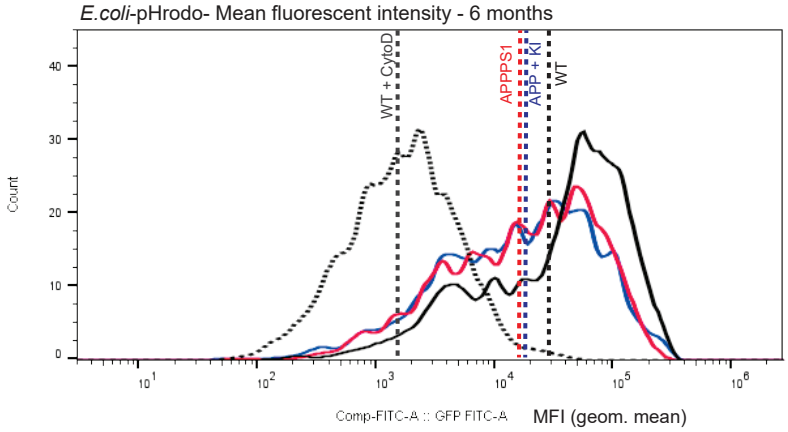

Sample (6M)	MFI (geom. mean)
WT	28836
WT + CytoD	1626
APPPS1	16930
APP + KI	19117

B

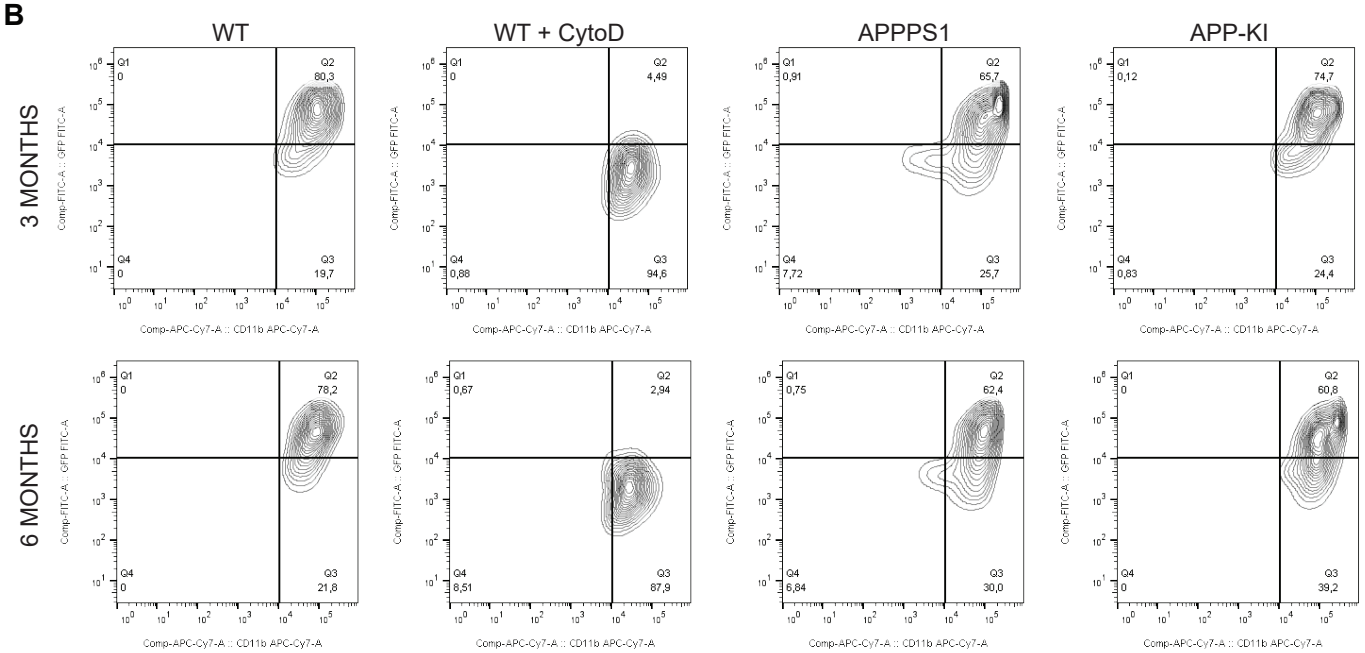

Suppl. Fig 8

Supplementary Tables

Suppl. Table 1: Optimized mass to charge (m/z) window distribution for Sequential Window Acquisition of all theoretical Mass Spectra (SWATH-MS) based on DIA.

Window	m/z start	m/z end	Center	Isolation width [m/z]
1	300	360	330	60
2	359	399	379	40
3	398	428	413	30
4	427	452	439.5	25
5	451	475	463	24
6	474	497	485.5	23
7	496	518	507	22
8	517	539	528	22
9	538	560	549	22
10	559	581	570	22
11	580	602	591	22
12	601	623	612	22
13	622	646	634	24
14	645	669	657	24
15	668	694	681	26
16	693	719	706	26
17	718	746	732	28
18	745	777	761	32
19	776	808	792	32
20	807	839	823	32
21	838	870	854	32
22	869	904	886.5	35
23	903	943	923	40
24	942	1,122	1,032	180
25	1,121	1,401	1,261	280

Suppl. Table 2: Comparison of proteomic results of APPPS1 microglia from DDA and DIA including the average peptide IDs, protein IDs, protein quantifications calculated for all samples**,** numbers of relatively quantified proteins from 1, 3, 6, and 12 months as well as their averages.

	DDA	DIA	DIA vs DDA
Overall Average Peptide IDs	53912	74281	137.8%
Overall Average Protein IDs	5502	5953	108.2%
Overall Average Protein Quantifications	5053	5952	117.8%
Relative quantifications (3 vs 3) APPPS1 vs WT 1M	4425	5491	124.1%
Relative quantifications (3 vs 3) APPPS1 vs WT 3M	4646	5789	124.6%
Relative quantifications (3 vs 3) APPPS1 vs WT 6M	4391	5848	133.2%
Relative quantifications (3 vs 3) APPPS1 vs WT 12M	4185	5669	135.5%
Average of relative quantifications	4412	5699	129.3%

Suppl. Table 3: Quantitative proteomic data analysis of APPPS1 (**A**) and APP-KI (**B**) *versus* WT microglia at 1, 3, 6, and 12 months using DIA. The table shows the number of consistently quantified proteins as well as proteins with a significant up- or down-regulation with and without FDR correction. A log2 fold change > 0.5 or < -0.5 and a p-value of less than 0.05 were applied as regulation thresholds. The amount of up-and down-regulated proteins with FDR correction is shown as percentage from the total number of quantified proteins.

A

	APPPS1 vs WT 1M	APPPS1 vs WT 3M	APPPS1 vs WT 6M	APPPS1 vs WT 12M
Quantifications (3 vs 3)	5491	5789	5848	5669
Regulated	98	1010	679	1409
Up-regulated	76	332	365	776
Down-regulated	22	678	314	633
Up-regulated FDR corrected	0	332	309	776
Down-regulated FDR corrected	0	678	261	633
Up-regulated FDR corrected (%)	0.0%	5.7%	5.3%	13.7%
Down-regulated FDR corrected (%)	0.0%	11.7%	4.5%	11.2%

B

	APP-KI vs WT 1M	APP-KI vs WT 3M	APP-KI vs WT 6M	APP-KI vs WT 12M
Quantifications (3 vs 3)	5713	5711	5653	5715
Regulated	41	700	559	1337
Up-regulated	19	22	245	704
Down-regulated	54	109	267	666
Up-regulated FDR corrected	0	1	140	704
Down-regulated FDR corrected	0	0	151	666
Up-regulated FDR corrected (%)	0.0%	0.0%	2.5%	12.3%
Down-regulated FDR corrected (%)	0.0%	0.0%	2.7%	11.7%

Suppl. Table 4: Identified early, middle, and advanced MARPs. Protein groups are represented by the major UniProt accession.

			MARPs (up: +1; down: -1)		
Gene Name	**UniProt Accession**	**Protein Name**	**Early MARP**	**Middle MARP**	**Advanced MARP**
Aacs	Q9D2R0	Acetoacetyl-CoA synthetase	0	1	0
Aagab	Q8R2R3	Alpha- and gamma-adaptin-binding protein p34	0	0	-1
Aak1	Q3UHJ0	AP2-associated protein kinase 1	0	0	1
Aarsd1	Q3THG9	Alanyl-tRNA editing protein Aarsd1	0	0	1
Abca9	Q8K449	ATP-binding cassette sub-family A member 9	0	-1	0
Abcb1b	P06795	Multidrug resistance protein 1B	0	1	0
Abcd2	Q61285	ATP-binding cassette sub-family D member 2	0	1	0
Abcg3	Q99P81	ATP-binding cassette sub-family G member 3	0	0	1
Abhd15	Q5F2F2	Protein ABHD15	0	-1	0
Abi1	Q8CBW3	Abl interactor 1	0	0	-1
Abi3	Q8BYZ1	ABI gene family member 3	0	0	-1
Acaca	Q5SWU9	Acetyl-CoA carboxylase 1	1	0	0
Acbd3	Q8BMP6	Golgi resident protein GCP60	0	0	1
Acot11	Q8VHQ9	Acyl-coenzyme A thioesterase 11	0	0	1
Acox3	Q9EPL9	Peroxisomal acyl-coenzyme A oxidase 3	0	1	0
Acsbg1	Q99PU5	Long-chain-fatty-acid--CoA ligase ACSBG1	0	0	1
Acss2	Q9QXG4	Acetyl-coenzyme A synthetase, cytoplasmic	0	0	1
Actn1	Q7TPR4	Alpha-actinin-1	0	-1	0
Actn4	P57780	Alpha-actinin-4	0	0	-1
Actr3b	Q641P0	Actin-related protein 3B	0	1	0
Ada	P03958	Adenosine deaminase	0	-1	0
Adam15	O88839	Disintegrin and metalloproteinase domain-containing protein 15	0	0	-1
Adam22	Q9R1V6	Disintegrin and metalloproteinase domain-containing protein 22	0	0	1
Adap2	Q8R2V5	Arf-GAP with dual PH domain-containing protein 2	0	-1	0
Add2	Q9QYB8	Beta-adducin	0	0	1
Adgre1	Q61549	Adhesion G protein-coupled receptor E1	0	-1	0
Adk	P55264	Adenosine kinase	0	0	1
Adss	P46664	Adenylosuccinate synthetase isozyme 2	0	1	0
Adssl1	P28650	Adenylosuccinate synthetase isozyme 1	1	0	0

			MARPs (up: +1; down: -1)		
Gene Name	**UniProt Accession**	**Protein Name**	**Early MARP**	**Middle MARP**	**Advanced MARP**
Ahcy	P50247	Adenosylhomocysteinase	0	0	1
Aif1	O70200	Allograft inflammatory factor 1	0	0	-1
Akap5	D3YVF0	A-kinase anchor protein 5	0	0	1
Akt3	Q9WUA6	RAC-gamma serine/threonine-protein kinase	0	0	1
Alb	P07724	Serum albumin	0	-1	0
Aldh1b1	Q9CZS1	Aldehyde dehydrogenase X, mitochondrial	0	0	1
Aldh1l1	Q8R0Y6	Cytosolic 10-formyltetrahydrofolate dehydrogenase	0	0	1
Aldh1l2	Q8K009	Mitochondrial 10-formyltetrahydrofolate dehydrogenase	0	0	1
Aldh2	P47738	Aldehyde dehydrogenase, mitochondrial	0	0	1
Aldoa	P05064	Fructose-bisphosphate aldolase A	0	1	0
Alg10b	Q3UGP8	Putative Dol-P-Glc:Glc(2)Man(9)GlcNAc(2)-PP-Dol alpha-1,2-glucosyltransferase	0	0	1
Ankh	Q9JHZ2	Progressive ankylosis protein	1	0	0
Anks1a	P59672	Ankyrin repeat and SAM domain-containing protein 1A	0	0	-1
Anxa1	P10107	Annexin A1	0	0	-1
Anxa2	P07356	Annexin A2	0	1	0
Anxa5	P48036	Annexin A5	0	1	0
Ap1s1	P61967	AP-1 complex subunit sigma-1A	0	0	1
Ap4b1	Q9WV76	AP-4 complex subunit beta-1	0	1	0
Apod	P51910	Apolipoprotein D	0	1	0
Apoe	P08226	Apolipoprotein E	1	0	0
Arhgap12	Q8C0D4	Rho GTPase-activating protein 12	0	-1	0
Arhgap22	Q8BL80	Rho GTPase-activating protein 22	0	0	-1
Arhgap30	Q640N3	Rho GTPase-activating protein 30	0	0	-1
Arhgap31	A6X8Z5	Rho GTPase-activating protein 31	0	0	-1
Arhgdib	Q61599	Rho GDP-dissociation inhibitor 2	0	0	-1
Arl6ip4	Q9JM93	ADP-ribosylation factor-like protein 6-interacting protein 4	0	-1	0
Arrb2	Q91YI4	Beta-arrestin-2	0	-1	0
Arsa	P50428	Arylsulfatase A	0	0	-1
Arsg	Q3TYD4	Arylsulfatase G	0	0	-1
Asah1	Q9WV54	Acid ceramidase	0	-1	0

			MARPs (up: +1; down: -1)		
Gene Name	**UniProt Accession**	**Protein Name**	**Early MARP**	**Middle MARP**	**Advanced MARP**
Asph	Q8BSY0	Aspartyl/asparaginyl beta-hydroxylase	0	0	1
Astn2	Q80Z10	Astrotactin-2	0	0	-1
Atg2a	Q6P4T0	Autophagy-related protein 2 homolog A	0	0	1
Atg7	Q9D906	Ubiquitin-like modifier-activating enzyme ATG7	0	0	1
Atp1b2	P14231	Sodium/potassium-transporting ATPase subunit beta-2	0	0	1
Atp1b3	P97370	Sodium/potassium-transporting ATPase subunit beta-3	0	0	1
Atp6v0a1	Q9Z1G4	V-type proton ATPase 116 kDa subunit a isoform 1	0	0	1
Atp6v1a	P50516	V-type proton ATPase catalytic subunit A	0	0	1
Atp6v1b2	P62814	V-type proton ATPase subunit B, brain isoform	0	0	1
Atp6v1c1	Q9Z1G3	V-type proton ATPase subunit C 1	0	0	1
Atp6v1d	P57746	V-type proton ATPase subunit D	0	0	1
Atp6v1e1	P50518	V-type proton ATPase subunit E 1	0	0	1
Atp6v1h	Q8BVE3	V-type proton ATPase subunit H	0	0	1
Atp8a2	P98200	Phospholipid-transporting ATPase IB	0	0	-1
Atxn10	P28658	Ataxin-10	0	0	1
B3galnt1	Q920V1	UDP-GalNAc:beta-1,3-N-acetylgalactosaminyltransferase 1	0	0	-1
B4galt5	Q9JMK0	Beta-1,4-galactosyltransferase 5	0	0	1
Baiap2	Q8BKX1	Brain-specific angiogenesis inhibitor 1-associated protein 2	0	0	1
Baz1b	Q9Z277	Tyrosine-protein kinase BAZ1B	0	0	-1
Bid	P70444	BH3-interacting domain death agonist	0	0	-1
Bin1	O08539	Myc box-dependent-interacting protein 1	0	0	-1
Bin2	D3Z6Q9	Bridging integrator 2	0	-1	0
Blvrb	Q923D2	Flavin reductase (NADPH)	0	0	-1
Bola2	Q8BGS2	BolA-like protein 2	1	0	0
Borcs5	Q9D920	BLOC-1-related complex subunit 5	0	0	-1
Borcs6	Q9D6W8	BLOC-1-related complex subunit 6	0	0	-1
Bri3bp	Q8BXV2	BRI3-binding protein	0	0	1
Brix1	Q9DCA5	Ribosome biogenesis protein BRX1 homolog	0	1	0
Brk1	Q91VR8	Protein BRICK1	0	0	-1
C5ar1	P30993	C5a anaphylatoxin chemotactic receptor 1	0	0	-1

			MARPs (up: +1; down: -1)		
Gene Name	**UniProt Accession**	**Protein Name**	**Early MARP**	**Middle MARP**	**Advanced MARP**
Calr	P14211	Calreticulin	0	0	1
Camp	P51437	Cathelicidin antimicrobial peptide	0	0	-1
Capg	P24452	Macrophage-capping protein	1	0	0
Capn1	O35350	Calpain-1 catalytic subunit	0	1	0
Casd1	Q7TN73	CAS1 domain-containing protein 1	0	0	1
Cask	O70589	Peripheral plasma membrane protein CASK	0	0	-1
Cbr2	P08074	Carbonyl reductase [NADPH] 2	0	-1	0
Cc2d1b	Q8BRN9	Coiled-coil and C2 domain-containing protein 1B	0	-1	0
Ccdc124	Q9D8X2	Coiled-coil domain-containing protein 124	0	0	-1
Ccdc30	Q8BVF4	Coiled-coil domain-containing protein 30	0	0	-1
Ccdc50	Q810U5	Coiled-coil domain-containing protein 50	0	0	-1
Ccdc88a	Q5SNZ0	Girdin	0	0	-1
Ccm2	Q8K2Y9	Cerebral cavernous malformations protein 2 homolog	0	0	-1
Ccnd1	P25322	G1/S-specific cyclin-D1	0	0	-1
Ccnk	O88874	Cyclin-K	0	0	1
Cd180	Q62192	CD180 antigen	1	0	0
Cd48	P18181	CD48 antigen	1	0	0
Cd63	P41731	CD63 antigen	0	1	0
Cd68	P31996	Macrosialin	1	0	0
Cd74	P04441	H-2 class II histocompatibility antigen gamma chain	1	0	0
Cdc42bpb	Q7TT50	Serine/threonine-protein kinase MRCK beta	0	-1	0
Cdk6	Q64261	Cyclin-dependent kinase 6	1	0	0
Cdk7	Q03147	Cyclin-dependent kinase 7	0	1	0
Cep170	Q6A065	Centrosomal protein of 170 kDa	0	0	-1
Cfl1	P18760	Cofilin-1	0	0	-1
Chmp3	Q9CQ10	Charged multivesicular body protein 3	0	0	-1
Chmp6	P0C0A3	Charged multivesicular body protein 6	0	0	-1
Chst12	Q99LL3	Carbohydrate sulfotransferase 12	0	1	0
Ckb	Q04447	Creatine kinase B-type	0	0	-1
Clec5a	Q9R007	C-type lectin domain family 5 member A	0	0	-1

			MARPs (up: +1; down: -1)		
Gene Name	**UniProt Accession**	**Protein Name**	**Early MARP**	**Middle MARP**	**Advanced MARP**
Clec7a	Q6QLQ4	C-type lectin domain family 7 member A	1	0	0
Cln3	Q61124	Battenin	1	0	0
Clstn1	Q9EPL2	Calsyntenin-1	0	0	-1
Cmklr1	P97468	Chemokine-like receptor 1	0	0	-1
Cmtm7	Q9ESD6	CKLF-like MARVEL transmembrane domain-containing protein 7	0	-1	0
Cnih4	Q9CX13	Protein cornichon homolog 4	0	0	1
Cnn2	Q08093	Calponin-2	0	-1	0
Cnpy2	Q9QXT0	Protein canopy homolog 2	0	0	1
Cntnap1	O54991	Contactin-associated protein 1	1	0	0
Cog2	Q921L5	Conserved oligomeric Golgi complex subunit 2	1	0	0
Cog5	Q8C0L8	Conserved oligomeric Golgi complex subunit 5	1	0	0
Cog7	Q3UM29	Conserved oligomeric Golgi complex subunit 7	0	1	0
Cog8	Q9JJA2	Conserved oligomeric Golgi complex subunit 8	0	0	1
Colgalt1	Q8K297	Procollagen galactosyltransferase 1	1	0	0
Commd1	Q8K4M5	COMM domain-containing protein 1	0	0	-1
Commd10	Q8JZY2	COMM domain-containing protein 10	0	0	-1
Commd5	Q8R395	COMM domain-containing protein 5	0	0	-1
Commd8	Q9CZG3	COMM domain-containing protein 8	0	0	-1
Coro1b	Q9WUM3	Coronin-1B	0	0	-1
Cpq	Q9WVJ3	Carboxypeptidase Q	0	-1	0
Cpsf3l	Q9CWS4	Integrator complex subunit 11	1	0	0
Crip1	P63254	Cysteine-rich protein 1	0	1	0
Crlf3	Q9Z2L7	Cytokine receptor-like factor 3	0	0	-1
Crybb1	Q9WVJ5	Beta-crystallin B1	0	0	-1
Csad	Q9DBE0	Cysteine sulfinic acid decarboxylase	0	0	-1
Csf1r	P09581	Macrophage colony-stimulating factor 1 receptor	0	0	-1
Csrp2	P97314	Cysteine and glycine-rich protein 2	0	-1	0
Cst3	P21460	Cystatin-C	0	0	-1
Cstb	Q62426	Cystatin-B	0	1	0
Cstf3	Q99LI7	Cleavage stimulation factor subunit 3	0	0	1

			MARPs (up: +1; down: -1)		
Gene Name	**UniProt Accession**	**Protein Name**	**Early MARP**	**Middle MARP**	**Advanced MARP**
Ctbs	Q8R242	Di-N-acetylchitobiase	0	-1	0
Ctnnb1	Q02248	Catenin beta-1	0	0	1
Ctsa	P16675	Lysosomal protective protein	0	0	1
Ctsd	P18242	Cathepsin D	1	0	0
Ctsh	P49935	Pro-cathepsin H	1	0	0
Ctsz	Q9WUU7	Cathepsin Z	1	0	0
Cttnbp2nl	Q99LJ0	CTTNBP2 N-terminal-like protein	0	0	-1
Cutc	Q9D8X1	Copper homeostasis protein cutC homolog	0	0	1
Cux1	P53564	Homeobox protein cut-like 1	0	0	1
Cx3cl1	O35188	Fractalkine	0	-1	0
Cx3cr1	Q9Z0D9	CX3C chemokine receptor 1	0	-1	0
Cybb	Q61093	Cytochrome b-245 heavy chain	0	0	1
Cyfip1	Q7TMB8	Cytoplasmic FMR1-interacting protein 1	0	0	-1
Cyhr1	Q9QXA1	Cysteine and histidine-rich protein 1	0	1	0
Cyp20a1	Q8BKE6	Cytochrome P450 20A1	0	0	1
Cyth4	Q80YW0	Cytohesin-4	0	0	-1
Dalrd3	Q6PJN8	DALR anticodon-binding domain-containing protein 3	0	0	-1
Dapp1	Q9QXT1	Dual adapter for phosphotyrosine and 3-phosphotyrosine and 3-phosphoinositide	0	-1	0
Dcxr	Q91X52	L-xylulose reductase	0	0	-1
Ddb2	Q99J79	DNA damage-binding protein 2	0	1	0
Ddx31	Q6NZQ2	Probable ATP-dependent RNA helicase DDX31	0	1	0
Ddx5	Q61656	Probable ATP-dependent RNA helicase DDX5	0	0	-1
Dennd1c	Q8CFK6	DENN domain-containing protein 1C	0	0	-1
Dffa	O54786	DNA fragmentation factor subunit alpha	0	0	-1
Dhcr7	O88455	7-dehydrocholesterol reductase	0	1	0
Dhrs3	O88876	Short-chain dehydrogenase/reductase 3	1	0	0
Dhx32	Q8BZS9	Putative pre-mRNA-splicing factor ATP-dependent RNA helicase DHX32	1	0	0
Dhx58	Q99J87	Probable ATP-dependent RNA helicase DHX58	1	0	0
Dip2b	Q3UH60	Disco-interacting protein 2 homolog B	0	0	-1
Dkc1	Q9ESX5	H/ACA ribonucleoprotein complex subunit 4	1	0	0

			MARPs (up: +1; down: -1)		
Gene Name	**UniProtAccession**	**Protein Name**	**EarlyMARP**	**MiddleMARP**	**Advanced MARP**
Dnaja2	Q9QYJ0	DnaJ homolog subfamily A member 2	0	0	-1
Dnajb14	Q149L6	DnaJ homolog subfamily B member 14	1	0	0
Dock10	Q8BZN6	Dedicator of cytokinesis protein 10	0	0	-1
Dock4	P59764	Dedicator of cytokinesis protein 4	0	0	-1
Dok1	P97465	Docking protein 1	0	0	-1
Dok3	Q9QZK7	Docking protein 3	0	0	-1
Dpagt1	P42867	UDP-N-acetylglucosamine--dolichyl-phosphate N-acetylglucosaminephosphotransferase	0	0	1
Dpy19l4	A2AJQ3	Probable C-mannosyltransferase DPY19L4	0	0	1
Dusp3	Q9D7X3	Dual specificity protein phosphatase 3	0	0	1
Dynlt3	P56387	Dynein light chain Tctex-type 3	0	0	1
Echs1	Q8BH95	Enoyl-CoA hydratase, mitochondrial	0	0	1
Eef2k	O08796	Eukaryotic elongation factor 2 kinase	0	0	-1
Ehd2	Q8BH64	EH domain-containing protein 2	-1	0	0
Eif4b	Q8BGD9	Eukaryotic translation initiation factor 4B	0	0	-1
Elmo2	Q8BHL5	Engulfment and cell motility protein 2	0	1	0
Elovl1	Q9JLJ5	Elongation of very long chain fatty acids protein 1	0	0	1
Eml2	Q7TNG5	Echinoderm microtubule-associated protein-like 2	0	0	1
Eno1	P17182	Alpha-enolase	0	0	1
Enpp1	P06802	Ectonucleotide pyrophosphatase/phosphodiesterase family member 1	0	1	0
Enpp4	Q8BTJ4	Bis(5'-adenosyl)-triphosphatase enpp4	0	-1	0
Entpd1	P55772	Ectonucleoside triphosphate diphosphohydrolase 1	0	0	-1
Epb41l2	O70318	Band 4.1-like protein 2	0	0	-1
Epdr1	Q99M71	Mammalian ependymin-related protein 1	0	0	-1
Epha2	Q03145	Ephrin type-A receptor 2	0	0	-1
Ephx1	Q9D379	Epoxide hydrolase 1	0	1	0
Epn1	Q80VP1	Epsin-1	0	0	-1
Ergic2	Q9CR89	Endoplasmic reticulum-Golgi intermediate compartment protein 2	0	0	1
Erlec1	Q8VEH8	Endoplasmic reticulum lectin 1	0	0	1
Ero1a	Q8R180	ERO1-like protein alpha	0	0	1
Erp29	P57759	Endoplasmic reticulum resident protein 29	0	1	0

			MARPs (up: +1; down: -1)		
Gene Name	**UniProt Accession**	**Protein Name**	**Early MARP**	**Middle MARP**	**Advanced MARP**
Erp44	Q9D1Q6	Endoplasmic reticulum resident protein 44	0	0	1
Evi5	P97366	Ecotropic viral integration site 5 protein	0	0	-1
Exoc1	Q8R3S6	Exocyst complex component 1	0	0	-1
F11r	O88792	Junctional adhesion molecule A	0	0	-1
F13a1	Q8BH61	Coagulation factor XIII A chain	0	-1	0
Fabp3	P11404	Fatty acid-binding protein, heart	0	1	0
Fabp5	Q05816	Fatty acid-binding protein, epidermal	0	1	0
Fam160b1	Q8CDM8	Protein FAM160B1	0	0	1
Fam213b	Q9DB60	Prostamide/prostaglandin F synthase	0	0	-1
Fam3c	Q91VU0	Protein FAM3C	0	0	1
Fam45a	Q9D8N2	Protein FAM45A	0	0	-1
Fam49b	Q921M7	Protein FAM49B	0	0	-1
Fasn	P19096	Fatty acid synthase	0	0	1
Fbxl14	Q8BID8	F-box/LRR-repeat protein 14	0	1	0
Fchsd2	Q3USJ8	F-BAR and double SH3 domains protein 2	0	0	-1
Fdps	Q920E5	Farnesyl pyrophosphate synthase	0	1	0
Fer	P70451	Tyrosine-protein kinase Fer	0	-1	0
Fez2	Q6TYB5	Fasciculation and elongation protein zeta-2	0	0	-1
Fgd2	Q8BY35	FYVE, RhoGEF and PH domain-containing protein 2	0	0	-1
Fgf1	P61148	Fibroblast growth factor 1	0	0	1
Fgf2	P15655	Fibroblast growth factor 2	0	1	0
Fhit	O89106	Bis(5'-adenosyl)-triphosphatase	0	-1	0
Filip1l	Q6P6L0	Filamin A-interacting protein 1-like	0	0	-1
Fkbp2	P45878	Peptidyl-prolyl cis-trans isomerase FKBP2	0	1	0
Fmnl1	Q9JL26	Formin-like protein 1	0	0	-1
Fmnl2	A2APV2	Formin-like protein 2	0	-1	0
Fmnl3	Q6ZPF4	Formin-like protein 3	0	-1	0
Fnbp1	Q80TY0	Formin-binding protein 1	0	0	-1
Frmd4a	Q8BIE6	FERM domain-containing protein 4A	0	0	-1
Fry	E9Q8I9	Protein furry homolog	0	0	1

			MARPs (up: +1; down: -1)		
Gene Name	**UniProt Accession**	**Protein Name**	**Early MARP**	**Middle MARP**	**Advanced MARP**
Fscn1	Q61553	Fascin	0	-1	0
Fth1	P09528	Ferritin heavy chain	0	0	1
Fuom	Q8R2K1	Fucose mutarotase	1	0	0
Fxyd1	Q9Z239	Phospholemman	0	0	1
Fyn	P39688	Tyrosine-protein kinase Fyn	0	0	1
Gab1	Q9QYY0	GRB2-associated-binding protein 1	0	-1	0
Gab2	Q9Z1S8	GRB2-associated-binding protein 2	0	0	-1
Galnt1	O08912	Polypeptide N-acetylgalactosaminyltransferase 1	0	0	1
Galnt2	Q6PB93	Polypeptide N-acetylgalactosaminyltransferase 2	0	0	1
Gatm	Q9D964	Glycine amidinotransferase, mitochondrial	0	0	-1
Gca	Q8VC88	Grancalcin	0	0	1
Gcat	O88986	2-amino-3-ketobutyrate coenzyme A ligase, mitochondrial	0	0	1
Gcc2	Q8CHG3	GRIP and coiled-coil domain-containing protein 2	0	0	1
Gde1	Q9JL56	Glycerophosphodiester phosphodiesterase 1	0	0	1
Get4	Q9D1H7	Golgi to ER traffic protein 4 homolog	0	0	1
Gfap	P03995	Glial fibrillary acidic protein	0	0	1
Gfpt1	P47856	Glutamine--fructose-6-phosphate aminotransferase [isomerizing] 1	0	1	0
Gja1	P23242	Gap junction alpha-1 protein	0	0	1
Glb1	P23780	Beta-galactosidase	1	0	0
Glg1	Q61543	Golgi apparatus protein 1	0	0	1
Glmn	Q8BZM1	Glomulin	0	0	1
Gmip	Q6PGG2	GEM-interacting protein	0	0	-1
Gna12	P27600	Guanine nucleotide-binding protein subunit alpha-12	0	-1	0
Gna15	P30678	Guanine nucleotide-binding protein subunit alpha-15	0	0	-1
Gnai1	B2RSH2	Guanine nucleotide-binding protein G(i) subunit alpha-1	0	0	-1
Gnai2	P08752	Guanine nucleotide-binding protein G(i) subunit alpha-2	0	0	-1
Gnb1	P62874	Guanine nucleotide-binding protein G(I)/G(S)/G(T) subunit beta-1	0	0	-1
Gnb2	P62880	Guanine nucleotide-binding protein G(I)/G(S)/G(T) subunit beta-2	0	0	-1
Gng10	Q9CXP8	Guanine nucleotide-binding protein G(I)/G(S)/G(O) subunit gamma-10	0	0	-1
Gng2	P63213	Guanine nucleotide-binding protein G(I)/G(S)/G(O) subunit gamma-2	0	0	-1

			MARPs (up: +1; down: -1)		
Gene Name	**UniProt Accession**	**Protein Name**	**Early MARP**	**Middle MARP**	**Advanced MARP**
Gng5	Q80SZ7	Guanine nucleotide-binding protein G(I)/G(S)/G(O) subunit gamma-5	0	0	-1
Gngt2	Q61017	Guanine nucleotide-binding protein G(I)/G(S)/G(O) subunit gamma-T2	0	0	-1
Gns	Q8BFR4	N-acetylglucosamine-6-sulfatase	0	0	1
Golga3	P55937	Golgin subfamily A member 3	0	0	1
Golga4	Q91VW5	Golgin subfamily A member 4	0	1	0
Golga5	Q9QYE6	Golgin subfamily A member 5	0	0	1
Golt1b	Q9CR60	Vesicle transport protein GOT1B	0	0	1
Got1	P05201	Aspartate aminotransferase, cytoplasmic	0	0	1
Gpd1	P13707	Glycerol-3-phosphate dehydrogenase [NAD(+)], cytoplasmic	-1	0	0
Gpi	P06745	Glucose-6-phosphate isomerase	0	0	1
Gpld1	O70362	Phosphatidylinositol-glycan-specific phospholipase D	0	-1	0
Gpm6a	P35802	Neuronal membrane glycoprotein M6-a	0	0	1
Gpr84	Q8CIM5	G-protein coupled receptor 84	1	0	0
Grap	Q9CX99	GRB2-related adapter protein	0	0	-1
Gsdmdc1	Q9D8T2	Gasdermin-D	0	0	-1
Gsn	P13020	Gelsolin	0	1	0
Gtf3c4	Q8BMQ2	General transcription factor 3C polypeptide 4	1	0	0
Gusb	P12265	Beta-glucuronidase	0	1	0
Gvin1	Q80SU7	Interferon-induced very large GTPase 1	1	0	0
Gyg1	Q9R062	Glycogenin-1	0	0	1
Gys1	Q9Z1E4	Glycogen [starch] synthase, muscle	0	0	1
H2afz	P0C0S6	Histone H2A.Z;Histone H2A.V	0	-1	0
H2-D1	P01899	H-2 class I histocompatibility antigen, D-B alpha chain	1	0	0
H2-K1	P01901	H-2 class I histocompatibility antigen, K-B alpha chain	1	0	0
H2-T23	P06339	H-2 class I histocompatibility antigen, D-37 alpha chain	0	1	0
H3f3c	P02301	Histone H3.3C;Histone H3.3	0	0	-1
Haao	Q78JT3	3-hydroxyanthranilate 3,4-dioxygenase	1	0	0
Hacd2	Q9D3B1	Very-long-chain (3R)-3-hydroxyacyl-CoA dehydratase 2	0	1	0
Hapln1	Q9QUP5	Hyaluronan and proteoglycan link protein 1	0	1	0
Hck	P08103	Tyrosine-protein kinase HCK	0	0	-1

			MARPs (up: +1; down: -1)		
Gene Name	**UniProt Accession**	**Protein Name**	**Early MARP**	**Middle MARP**	**Advanced MARP**
Hepacam	Q640R3	Hepatocyte cell adhesion molecule	0	0	1
Hexa	P29416	Beta-hexosaminidase subunit alpha	1	0	0
Hexb	P20060	Beta-hexosaminidase subunit beta	0	0	1
Hic2	Q9JLZ6	Hypermethylated in cancer 2 protein	0	0	-1
Hist1h1a	P43275	Histone H1.1	0	1	0
Hist1h1b	P43276	Histone H1.5	0	1	0
Hist1h2ab	P22752	Histone H2A type 1	0	0	-1
Hist1h2bf	P10853	Histone H2B type 1-F/J/L	0	0	-1
Hist2h2ac	Q64523	Histone H2A type 2-C	0	-1	0
Hmga1	P17095	High mobility group protein HMG-I/HMG-Y	0	-1	0
Hmgn2	P09602	Non-histone chromosomal protein HMG-17	0	-1	0
Hmha1	Q3TBD2	Minor histocompatibility protein HA-1	0	0	-1
Hmox1	P14901	Heme oxygenase 1	0	1	0
Hpca	P84075	Neuron-specific calcium-binding protein hippocalcin	0	0	1
Hpcal1	P62748	Hippocalcin-like protein 1	0	0	1
Hpcal4	Q8BGZ1	Hippocalcin-like protein 4	0	0	1
Hpf1	Q8CFE2	Histone PARylation factor 1	0	0	1
Hpgd	Q8VCC1	15-hydroxyprostaglandin dehydrogenase [NAD(+)]	0	0	-1
Hpgds	Q9JHF7	Hematopoietic prostaglandin D synthase	0	0	-1
Hras	Q61411	GTPase HRas	0	0	-1
Hsd17b12	O70503	Very-long-chain 3-oxoacyl-CoA reductase	0	1	0
Hspa5	P20029	78 kDa glucose-regulated protein	0	0	1
Htra1	Q9R118	Serine protease HTRA1	1	0	0
Hyal1	Q91ZJ9	Hyaluronidase-1	0	0	-1
Idh2	P54071	Isocitrate dehydrogenase [NADP], mitochondrial	0	-1	0
Ier3ip1	Q9CR20	Immediate early response 3-interacting protein 1	0	0	1
Ifi204	P0DOV2	Interferon-activable protein 204	1	0	0
Ifit2	Q64112	Interferon-induced protein with tetratricopeptide repeats 2	1	0	0
Ifit3	Q64345	Interferon-induced protein with tetratricopeptide repeats 3	1	0	0
Ifitm3	Q9CQW9	Interferon-induced transmembrane protein 3	0	1	0

			MARPs (up: +1; down: -1)		
Gene Name	**UniProt Accession**	**Protein Name**	**Early MARP**	**Middle MARP**	**Advanced MARP**
Igfbp7	Q61581	Insulin-like growth factor-binding protein 7	0	-1	0
Il16	O54824	Pro-interleukin-16	0	0	-1
Il6st	Q00560	Interleukin-6 receptor subunit beta	0	0	-1
Ilf2	Q9CXY6	Interleukin enhancer-binding factor 2	0	0	1
Inf2	Q0GNC1	Inverted formin-2	0	0	1
Inpp4b	Q6P1Y8	Type II inositol 3,4-bisphosphate 4-phosphatase	0	0	-1
Ints1	Q6P4S8	Integrator complex subunit 1	0	0	1
Ints2	Q80UK8	Integrator complex subunit 2	1	0	0
Ints3	Q7TPD0	Integrator complex subunit 3	0	0	1
Ints5	Q8CHT3	Integrator complex subunit 5	0	0	1
Ints7	Q7TQK1	Integrator complex subunit 7	0	0	1
Ipo4	Q8VI75	Importin-4	0	1	0
Irak1	Q62406	Interleukin-1 receptor-associated kinase 1	0	0	-1
Isg15	Q64339	Ubiquitin-like protein ISG15	1	0	0
Ist1	Q9CX00	IST1 homolog	0	1	0
Itga9	B8JK39	Integrin alpha-9	0	-1	0
Itgav	P43406	Integrin alpha-V	0	0	-1
Itgax	Q9QXH4	Integrin alpha-X	1	0	0
Itgb6	Q9Z0T9	Integrin beta-6	0	0	-1
Itpr2	Q9Z329	Inositol 1,4,5-trisphosphate receptor type 2	0	-1	0
Itpr3	P70227	Inositol 1,4,5-trisphosphate receptor type 3	0	-1	0
Ivns1abp	Q920Q8	Influenza virus NS1A-binding protein homolog	0	0	-1
Jak1	P52332	Tyrosine-protein kinase JAK1	0	0	-1
Kif1a	P33173	Kinesin-like protein KIF1A	0	0	1
Kras	P32883	GTPase KRas	-1	0	0
Krtcap2	Q5RL79	Keratinocyte-associated protein 2	0	0	1
Ldhb	P16125	L-lactate dehydrogenase B chain	0	0	-1
Lgals3	P16110	Galectin-3	1	0	0
Lgals3bp	Q07797	Galectin-3-binding protein	1	0	0
Lgals9	O08573	Galectin-9	0	0	-1

			MARPs (up: +1; down: -1)		
Gene Name	**UniProt Accession**	**Protein Name**	**Early MARP**	**Middle MARP**	**Advanced MARP**
Limd2	Q8BGB5	LIM domain-containing protein 2	0	0	-1
Llgl1	Q80Y17	Lethal(2) giant larvae protein homolog 1	-1	0	0
Lman1	Q9D0F3	Protein ERGIC-53	0	1	0
Lman2	Q9DBH5	Vesicular integral-membrane protein VIP36	0	0	1
Lmna	P48678	Prelamin-A/C	0	0	1
Lmnb2	P21619	Lamin-B2	0	0	1
Lpcat2	Q8BYI6	Lysophosphatidylcholine acyltransferase 2	0	0	-1
Lrp1	Q91ZX7	Prolow-density lipoprotein receptor-related protein 1	0	0	-1
Lrpap1	P55302	Alpha-2-macroglobulin receptor-associated protein	0	1	0
Lrrc20	Q8CI70	Leucine-rich repeat-containing protein 20	0	0	1
Lrrc25	Q8K1T1	Leucine-rich repeat-containing protein 25	0	-1	0
Lrrc8d	Q8BGR2	Volume-regulated anion channel subunit LRRC8D	0	0	1
Ltc4s	Q60860	Leukotriene C4 synthase	0	0	-1
Luc7l3	Q5SUF2	Luc7-like protein 3	-1	0	0
Ly86	O88188	Lymphocyte antigen 86	1	0	0
Lyn	P25911	Tyrosine-protein kinase Lyn	0	0	-1
Lyplal1	Q3UFF7	Lysophospholipase-like protein 1	0	0	1
Lyz2	P08905	Lysozyme C-2	0	0	1
Magt1	Q9CQY5	Magnesium transporter protein 1	0	0	1
Manf	Q9CXI5	Mesencephalic astrocyte-derived neurotrophic factor	0	0	1
Map1s	Q8C052	Microtubule-associated protein 1S	0	0	-1
Map3k3	Q61084	Mitogen-activated protein kinase kinase kinase 3	0	0	-1
Map4	P27546	Microtubule-associated protein 4	0	0	-1
Map4k4	P97820	Mitogen-activated protein kinase kinase kinase kinase 4	0	-1	0
Map7d1	A2AJI0	MAP7 domain-containing protein 1	0	-1	0
Mapre1	Q61166	Microtubule-associated protein RP/EB family member 1	0	0	-1
Marcks	P26645	Myristoylated alanine-rich C-kinase substrate	0	0	-1
Marcksl1	P28667	MARCKS-related protein	0	0	-1
Mcm2	P97310	DNA replication licensing factor MCM2	0	1	0
Mcm3	P25206	DNA replication licensing factor MCM3	0	1	0

			MARPs (up: +1; down: -1)		
Gene Name	**UniProt Accession**	**Protein Name**	**Early MARP**	**Middle MARP**	**Advanced MARP**
Mcm5	P49718	DNA replication licensing factor MCM5	1	0	0
Med15	Q924H2	Mediator of RNA polymerase II transcription subunit 15	0	0	1
Mgat2	Q921V5	Alpha-1,6-mannosyl-glycoprotein 2-beta-N-acetylglucosaminyltransferase	0	0	1
Mgst3	Q9CPU4	Microsomal glutathione S-transferase 3	0	0	1
Mif	P34884	Macrophage migration inhibitory factor	0	1	0
Milr1	Q3TB92	Allergin-1	1	0	0
Mnda	P0DOV1	Interferon-activable protein 205-B	1	0	0
Mospd2	Q9CWP6	Motile sperm domain-containing protein 2	0	1	0
Mov10	P23249	Putative helicase MOV-10	1	0	0
Mpeg1	A1L314	Macrophage-expressed gene 1 protein	1	0	0
Mpi	Q924M7	Mannose-6-phosphate isomerase	0	0	-1
Mras	O08989	Ras-related protein M-Ras	0	0	-1
Mrc1	Q61830	Macrophage mannose receptor 1	0	-1	0
Mrpl40	Q9Z2Q5	39S ribosomal protein L40, mitochondrial	0	0	1
Msmo1	Q9CRA4	Methylsterol monooxygenase 1	0	0	1
Mthfs	Q9D110	5-formyltetrahydrofolate cyclo-ligase	0	0	1
Mto1	Q923Z3	Protein MTO1 homolog, mitochondrial	0	0	1
Mtr	A6H5Y3	Methionine synthase	0	0	-1
Mvb12b	Q6KAU4	Multivesicular body subunit 12B	0	0	-1
Myo1b	P46735	Unconventional myosin-Ib	0	0	-1
Myo1g	Q5SUA5	Unconventional myosin-Ig	0	0	-1
Myo5a	Q99104	Unconventional myosin-Va	0	0	1
Myo9a	Q8C170	Unconventional myosin-IXa	0	0	-1
Naa25	Q8BWZ3	N-alpha-acetyltransferase 25, NatB auxiliary subunit	0	0	1
Naaa	Q9D7V9	N-acylethanolamine-hydrolyzing acid amidase	0	-1	0
Nampt	Q99KQ4	Nicotinamide phosphoribosyltransferase	0	1	0
Ncan	P55066	Neurocan core protein	0	0	1
Nceh1	Q8BLF1	Neutral cholesterol ester hydrolase 1	0	1	0
Ncl	P09405	Nucleolin	0	0	1
Ndrg2	Q9QYG0	Protein NDRG2	0	0	1

			MARPs (up: +1; down: -1)		
Gene Name	**UniProt Accession**	**Protein Name**	**Early MARP**	**Middle MARP**	**Advanced MARP**
Nenf	Q9CQ45	Neudesin	0	0	1
Neu4	Q8BZL1	Sialidase-4	0	0	-1
Nfatc1	O88942	Nuclear factor of activated T-cells, cytoplasmic 1	0	0	-1
Nfatc2	Q60591	Nuclear factor of activated T-cells, cytoplasmic 2	0	0	-1
Nfkbib	Q60778	NF-kappa-B inhibitor beta	0	0	-1
Ngp	O08692	Neutrophilic granule protein	0	0	-1
Nipsnap3b	Q9CQE1	Protein NipSnap homolog 3B	0	0	1
Nit1	Q8VDK1	Nitrilase homolog 1	0	0	-1
Nkiras2	Q9CR56	NF-kappa-B inhibitor-interacting Ras-like protein 2	0	0	1
No66	Q9JJF3	Bifunctional lysine-specific demethylase and histidyl-hydroxylase NO66	0	0	1
Nop10	Q9CQS2	H/ACA ribonucleoprotein complex subunit 3	1	0	0
Npc2	Q9Z0J0	Epididymal secretory protein E1	1	0	0
Nras	P08556	GTPase NRas	0	0	-1
Nrbf2	Q8VCQ3	Nuclear receptor-binding factor 2	1	0	0
Nsdhl	Q9R1J0	Sterol-4-alpha-carboxylate 3-dehydrogenase, decarboxylating	0	0	1
Nucb1	Q02819	Nucleobindin-1	0	0	1
Nucb2	P81117	Nucleobindin-2	1	0	0
Numb	Q9QZS3	Protein numb homolog	0	-1	0
Numbl	O08919	Numb-like protein	0	-1	0
Nup155	Q99P88	Nuclear pore complex protein Nup155	0	0	1
Oas1a	P11928	2'-5'-oligoadenylate synthase 1A	1	0	0
Olfml3	Q8BK62	Olfactomedin-like protein 3	0	0	-1
Omg	Q63912	Oligodendrocyte-myelin glycoprotein	-1	0	0
Ophn1	Q99J31	Oligophrenin-1	0	0	-1
ORF11	Q9ERY9	Probable ergosterol biosynthetic protein 28	0	0	1
Os9	Q8K2C7	Protein OS-9	0	1	0
Osbpl3	Q9DBS9	Oxysterol-binding protein-related protein 3	0	0	1
Osbpl8	B9EJ86	Oxysterol-binding protein-related protein 8	0	0	1
P2rx4	Q9JJX6	P2X purinoceptor 4	0	0	1
P2rx7	Q9Z1M0	P2X purinoceptor 7	0	0	-1

			MARPs (up: +1; down: -1)		
Gene Name	**UniProt Accession**	**Protein Name**	**Early MARP**	**Middle MARP**	**Advanced MARP**
P2ry12	Q9CPV9	P2Y purinoceptor 12	0	-1	0
P2yr13	Q9D8I2	P2Y purinoceptor 13	0	0	-1
Pacsin1	Q61644	Protein kinase C and casein kinase substrate in neurons protein 1	0	0	1
Pacsin2	Q9WVE8	Protein kinase C and casein kinase substrate in neurons protein 2	0	0	-1
Paf1	Q8K2T8	RNA polymerase II-associated factor 1 homolog	0	0	1
Pclo	Q9QYX7	Protein piccolo	0	0	-1
Pcna	P17918	Proliferating cell nuclear antigen	1	0	0
Pde3b	Q61409	cGMP-inhibited 3',5'-cyclic phosphodiesterase B	0	-1	0
Pdia4	P08003	Protein disulfide-isomerase A4	0	0	1
Pdlim4	P70271	PDZ and LIM domain protein 4	0	-1	0
Pdlim5	Q8CI51	PDZ and LIM domain protein 5	0	-1	0
Pdxdc1	Q99K01	Pyridoxal-dependent decarboxylase domain-containing protein 1	0	1	0
Pfkl	P12382	ATP-dependent 6-phosphofructokinase, liver type	0	1	0
Pgam1	Q9DBJ1	Phosphoglycerate mutase 1	0	0	1
Pgam2	O70250	Phosphoglycerate mutase 2	0	1	0
Pgap1	Q3UUQ7	GPI inositol-deacylase	0	0	1
Pgk1	P09411	Phosphoglycerate kinase 1	0	1	0
Pgm1	Q9D0F9	Phosphoglucomutase-1	0	0	1
Phf11	A6H5X4	PHD finger protein 11	1	0	0
Phyhd1	Q9DB26	Phytanoyl-CoA dioxygenase domain-containing protein 1	0	0	-1
Pi4k2a	Q2TBE6	Phosphatidylinositol 4-kinase type 2-alpha	1	0	0
Pid1	Q3UBG2	PTB-containing, cubilin and LRP1-interacting protein	0	0	-1
Pik3ap1	Q9EQ32	Phosphoinositide 3-kinase adapter protein 1	0	0	-1
Pik3r5	Q5SW28	Phosphoinositide 3-kinase regulatory subunit 5	0	0	-1
Pik3r6	Q3U6Q4	Phosphoinositide 3-kinase regulatory subunit 6	0	0	-1
Pikfyve	Q9Z1T6	1-phosphatidylinositol 3-phosphate 5-kinase	0	0	1
Pip4k2a	O70172	Phosphatidylinositol 5-phosphate 4-kinase type-2 alpha	-1	0	0
Pip4k2b	Q80XI4	Phosphatidylinositol 5-phosphate 4-kinase type-2 beta	0	-1	0
Pkm	P52480	Pyruvate kinase PKM	0	1	0
Pkn1	P70268	Serine/threonine-protein kinase N1	0	0	-1

			MARPs (up: +1; down: -1)		
Gene Name	**UniProt Accession**	**Protein Name**	**Early MARP**	**Middle MARP**	**Advanced MARP**
Plcb3	P51432	1-phosphatidylinositol 4,5-bisphosphate phosphodiesterase beta-3	0	0	-1
Plcl2	Q8K394	Inactive phospholipase C-like protein 2	0	0	-1
Pld4	Q8BG07	Phospholipase D4	0	0	-1
Plekha1	Q8BUL6	Pleckstrin homology domain-containing family A member 1	0	0	1
Plekho1	Q9JIY0	Pleckstrin homology domain-containing family O member 1	0	0	-1
Plgrkt	Q9D3P8	Plasminogen receptor (KT)	0	1	0
Plp2	Q9R1Q7	Proteolipid protein 2	0	1	0
Plpp3	Q99JY8	Phospholipid phosphatase 3	0	0	1
Plrg1	Q922V4	Pleiotropic regulator 1	0	0	1
Plscr3	Q9JIZ9	Phospholipid scramblase 3	0	-1	0
Plxnb2	B2RXS4	Plexin-B2	0	0	-1
Pml	Q60953	Protein PML	1	0	0
Pnp	P23492	Purine nucleoside phosphorylase	0	-1	0
Pofut2	Q8VHI3	GDP-fucose protein O-fucosyltransferase 2	0	1	0
Ppig	A2AR02	Peptidyl-prolyl cis-trans isomerase G	0	-1	0
Ppp1r18	Q8BQ30	Phostensin	0	0	-1
Praf2	Q9JIG8	PRA1 family protein 2	0	0	1
Prdx1	P35700	Peroxiredoxin-1	0	0	1
Prdx4	O08807	Peroxiredoxin-4	1	0	0
Prdx6	O08709	Peroxiredoxin-6	0	0	1
Prkab1	Q9R078	5'-AMP-activated protein kinase subunit beta-1	0	0	-1
Prkcd	P28867	Protein kinase C delta type	0	-1	0
Prpf40a	Q9R1C7	Pre-mRNA-processing factor 40 homolog A	0	0	-1
Prpf8	Q99PV0	Pre-mRNA-processing-splicing factor 8	0	0	-1
Psat1	Q99K85	Phosphoserine aminotransferase	1	0	0
Ptp4a2	O70274	Protein tyrosine phosphatase type IVA 2	0	0	-1
Ptp4a3	Q9D658	Protein tyrosine phosphatase type IVA 3	0	0	-1
Ptprj	Q64455	Receptor-type tyrosine-protein phosphatase eta	0	0	-1
Ptrf	O54724	Polymerase I and transcript release factor	0	-1	0
Pts	Q9R1Z7	6-pyruvoyl tetrahydrobiopterin synthase	0	0	-1

			MARPs (up: +1; down: -1)		
Gene Name	**UniProt Accession**	**Protein Name**	**Early MARP**	**Middle MARP**	**Advanced MARP**
Pxk	Q8BX57	PX domain-containing protein kinase-like protein	0	-1	0
Pxn	Q8VI36	Paxillin	0	0	-1
Pyhin1	Q8BV49	Pyrin and HIN domain-containing protein 1	1	0	0
Rab39a	Q8BHD0	Ras-related protein Rab-39A	0	0	-1
Rab3d	P35276	Ras-related protein Rab-3D	0	0	1
Rab3il1	Q8VDV3	Guanine nucleotide exchange factor for Rab-3A	0	0	-1
Rac2	Q05144	Ras-related C3 botulinum toxin substrate 2	0	0	-1
Rala	P63321	Ras-related protein Ral-A	0	-1	0
Ralgapb	Q8BQZ4	Ral GTPase-activating protein subunit beta	0	0	1
Rap1b	Q99JI6	Ras-related protein Rap-1b	0	0	-1
Rap2b	P61226	Ras-related protein Rap-2b	0	0	1
Rap2c	Q8BU31	Ras-related protein Rap-2c	0	0	-1
Rassf2	Q8BMS9	Ras association domain-containing protein 2	0	0	-1
Rbbp9	O88851	Putative hydrolase RBBP9	0	0	-1
Rbm39	Q8VH51	RNA-binding protein 39	0	-1	0
Rcc1	Q8VE37	Regulator of chromosome condensation	0	-1	0
Rcsd1	Q3UZA1	CapZ-interacting protein	0	0	-1
Rer1	Q9CQU3	Protein RER1	0	1	0
Rgs10	Q9CQE5	Regulator of G-protein signaling 10	0	0	-1
Rgs19	Q9CX84	Regulator of G-protein signaling 19	0	0	-1
Rhoc	Q62159	Rho-related GTP-binding protein RhoC	0	1	0
Rhog	P84096	Rho-related GTP-binding protein RhoG	0	0	-1
Rhoq	Q8R527	Rho-related GTP-binding protein RhoQ	0	0	-1
Rnaseh2a	Q9CWY8	Ribonuclease H2 subunit A	0	0	1
Rnaseh2c	Q9CQ18	Ribonuclease H2 subunit C	0	1	0
Rnf130	Q8VEM1	E3 ubiquitin-protein ligase RNF130	0	0	-1
Rp2	Q9EPK2	Protein XRP2	0	0	-1
Rpl13a	P19253	60S ribosomal protein L13a	1	0	0
Rpl38	Q9JJI8	60S ribosomal protein L38	-1	0	0
Rpl7	P14148	60S ribosomal protein L7	1	0	0

			MARPs (up: +1; down: -1)		
Gene Name	**UniProt Accession**	**Protein Name**	**Early MARP**	**Middle MARP**	**Advanced MARP**
Rps15	P62843	40S ribosomal protein S15	1	0	0
Rps27a	P62983	Ubiquitin-40S ribosomal protein S27a	0	0	1
Rps6ka1	P18653	Ribosomal protein S6 kinase alpha-1	0	-1	0
Rps6ka3	P18654	Ribosomal protein S6 kinase alpha-3	0	0	-1
Rras2	P62071	Ras-related protein R-Ras2	0	0	-1
Rtn4	Q99P72	Reticulon-4	0	-1	0
Scly	Q9JLI6	Selenocysteine lyase	0	0	1
Scpep1	Q920A5	Retinoid-inducible serine carboxypeptidase	0	0	1
Sdcbp	O08992	Syntenin-1	1	0	0
Sec14l2	Q99J08	SEC14-like protein 2	0	0	1
Sec23ip	Q6NZC7	SEC23-interacting protein	0	1	0
Sec61a1	P61620	Protein transport protein Sec61 subunit alpha isoform 1	0	0	1
Sel1l	Q9Z2G6	Protein sel-1 homolog 1	0	0	1
Serpinc1	P32261	Antithrombin-III	0	-1	0
Serpini1	O35684	Neuroserpin	0	0	-1
Sf3b5	Q923D4	Splicing factor 3B subunit 5	0	0	-1
Sh3bgrl	Q9JJU8	SH3 domain-binding glutamic acid-rich-like protein	0	0	1
Sh3bp1	P55194	SH3 domain-binding protein 1	0	0	-1
Sil1	Q9EPK6	Nucleotide exchange factor SIL1	1	0	0
Sirpa	P97797	Tyrosine-protein phosphatase non-receptor type substrate 1	0	0	-1
Slc16a1	P53986	Monocarboxylate transporter 1	0	0	1
Slc17a7	Q3TXX4	Vesicular glutamate transporter 1	0	0	1
Slc23a2	Q9EPR4	Solute carrier family 23 member 2	0	1	0
Slc2a5	Q9WV38	Solute carrier family 2, facilitated glucose transporter member 5	0	-1	0
Slc30a3	P97441	Zinc transporter 3	0	0	1
Slc30a6	Q8BJM5	Zinc transporter 6	1	0	0
Slc35b1	P97858	Solute carrier family 35 member B1	0	0	1
Slc35b2	Q91ZN5	Adenosine 3'-phospho 5'-phosphosulfate transporter 1	0	1	0
Slc35e1	Q8CD26	Solute carrier family 35 member E1	0	1	0
Slc37a2	Q9WU81	Glucose-6-phosphate exchanger SLC37A2	0	0	1

			MARPs (up: +1; down: -1)		
Gene Name	**UniProt Accession**	**Protein Name**	**Early MARP**	**Middle MARP**	**Advanced MARP**
Slc38a10	Q5I012	Putative sodium-coupled neutral amino acid transporter 10	0	1	0
Slc4a4	O88343	Electrogenic sodium bicarbonate cotransporter 1	0	0	1
Slc9a1	Q61165	Sodium/hydrogen exchanger 1	0	0	-1
Slco2b1	Q8BXB6	Solute carrier organic anion transporter family member 2B1	0	0	-1
Slmap	Q3URD3	Sarcolemmal membrane-associated protein	0	0	-1
Smad1	P70340	Mothers against decapentaplegic homolog 1	0	-1	0
Smad2	Q62432	Mothers against decapentaplegic homolog 2	0	0	-1
Smad3	Q8BUN5	Mothers against decapentaplegic homolog 3	0	-1	0
Smim1	P0C8K7	Small integral membrane protein 1	0	-1	0
Smox	Q99K82	Spermine oxidase	0	0	-1
Smpdl3a	P70158	Acid sphingomyelinase-like phosphodiesterase 3a	0	-1	0
Smpdl3b	P58242	Acid sphingomyelinase-like phosphodiesterase 3b	0	-1	0
Snx17	Q8BVL3	Sorting nexin-17	0	0	-1
Snx18	Q91ZR2	Sorting nexin-18	0	0	-1
Snx9	Q91VH2	Sorting nexin-9	0	0	-1
Soat1	Q61263	Sterol O-acyltransferase 1	1	0	0
Soga1	E1U8D0	Protein SOGA1	0	0	-1
Sort1	Q6PHU5	Sortilin	0	0	-1
Sp100	O35892	Nuclear autoantigen Sp-100	1	0	0
Sp3	O70494	Transcription factor Sp3	0	0	-1
Sparc	P07214	SPARC	0	0	-1
Sparcl1	P70663	SPARC-like protein 1	0	-1	0
Spg20	Q8R1X6	Spartin	0	0	-1
Spg21	Q9CQC8	Maspardin	1	0	0
Spock2	Q9ER58	Testican-2	0	-1	0
Sqrdl	Q9R112	Sulfide:quinone oxidoreductase, mitochondrial	0	-1	0
Srbd1	Q497V5	S1 RNA-binding domain-containing protein 1	0	1	0
Srgap2	Q91Z67	SLIT-ROBO Rho GTPase-activating protein 2	0	-1	0
Srpk2	O54781	SRSF protein kinase 2	1	0	0
Ssr1	Q9CY50	Translocon-associated protein subunit alpha	0	1	0

			MARPs (up: +1; down: -1)		
Gene Name	**UniProt Accession**	**Protein Name**	**Early MARP**	**Middle MARP**	**Advanced MARP**
Ssr4	Q62186	Translocon-associated protein subunit delta	0	0	1
Stab1	Q8R4Y4	Stabilin-1	0	-1	0
Stard3nl	Q9DCI3	MLN64 N-terminal domain homolog	0	0	-1
Stat1	P42225	Signal transducer and activator of transcription 1	1	0	0
Stat2	Q9WVL2	Signal transducer and activator of transcription 2	1	0	0
Stk10	O55098	Serine/threonine-protein kinase 10	0	0	-1
Stk26	Q99JT2	Serine/threonine-protein kinase 26	0	0	-1
Sts	P50427	Steryl-sulfatase	0	0	1
Stt3b	Q3TDQ1	Dolichyl-diphosphooligosaccharide--protein glycosyltransferase subunit STT3B	0	0	1
Sult1a1	P52840	Sulfotransferase 1A1	0	0	-1
Susd3	Q9D176	Sushi domain-containing protein 3	0	-1	0
Syk	P48025	Tyrosine-protein kinase SYK	0	-1	0
Syngr1	O55100	Synaptogyrin-1	0	0	1
Tamm41	Q3TUH1	Phosphatidate cytidylyltransferase, mitochondrial	-1	0	0
Taok1	Q5F2E8	Serine/threonine-protein kinase TAO1	0	0	-1
Tap2	P36371	Antigen peptide transporter 2	1	0	0
Tapbp	Q9R233	Tapasin	1	0	0
Tbc1d10b	Q8BHL3	TBC1 domain family member 10B	-1	0	0
Tbc1d22a	Q8R5A6	TBC1 domain family member 22A	0	0	1
Tbc1d4	Q8BYJ6	TBC1 domain family member 4	0	0	1
Tfap2a	P34056	Transcription factor AP-2-alpha	0	0	-1
Tfe3	Q64092	Transcription factor E3	0	0	-1
Tfeb	Q9R210	Transcription factor EB	0	0	-1
Tgfbr1	Q64729	TGF-beta receptor type-1	0	0	-1
Tgm2	P21981	Protein-glutamine gamma-glutamyltransferase 2	0	-1	0
Them6	Q80ZW2	Protein THEM6	0	0	1
Tigar	Q8BZA9	Fructose-2,6-bisphosphatase TIGAR	0	0	1
Tjp1	P39447	Tight junction protein ZO-1	0	0	-1
Tkt	P40142	Transketolase	0	1	0
Tlk2	O55047	Serine/threonine-protein kinase tousled-like 2	0	0	1

			MARPs (up: +1; down: -1)		
Gene Name	**UniProt Accession**	**Protein Name**	**Early MARP**	**Middle MARP**	**Advanced MARP**
Tlr2	Q9QUN7	Toll-like receptor 2	1	0	0
Tlr3	Q99MB1	Toll-like receptor 3	0	0	-1
Tlr9	Q9EQU3	Toll-like receptor 9	0	-1	0
Tm6sf1	P58749	Transmembrane 6 superfamily member 1	0	-1	0
Tm9sf1	Q9DBU0	Transmembrane 9 superfamily member 1	0	1	0
Tm9sf3	Q9ET30	Transmembrane 9 superfamily member 3	0	1	0
Tm9sf4	Q8BH24	Transmembrane 9 superfamily member 4	0	0	1
Tmed10	Q9D1D4	Transmembrane emp24 domain-containing protein 10	0	1	0
Tmed3	Q78IS1	Transmembrane emp24 domain-containing protein 3	0	0	1
Tmed4	Q8R1V4	Transmembrane emp24 domain-containing protein 4	0	1	0
Tmed9	Q99KF1	Transmembrane emp24 domain-containing protein 9	0	1	0
Tmem100	Q9CQG9	Transmembrane protein 100	0	-1	0
Tmem119	Q8R138	Transmembrane protein 119	0	-1	0
Tmem163	Q8C996	Transmembrane protein 163	0	0	1
Tmem167a	Q9CR64	Protein kish-A	0	0	1
Tmem173	Q3TBT3	Stimulator of interferon genes protein	0	0	-1
Tmem205	Q91XE8	Transmembrane protein 205	0	0	1
Tmem214	Q8BM55	Transmembrane protein 214	0	0	1
Tmem38b	Q9DAV9	Trimeric intracellular cation channel type B	0	0	1
Tmsb10	Q6ZWY8	Thymosin beta-10	0	0	1
Tnfaip8l2	Q9D8Y7	Tumor necrosis factor alpha-induced protein 8-like protein 2	0	-1	0
Top2b	Q64511	DNA topoisomerase 2-beta	0	0	1
Tpcn1	Q9EQJ0	Two pore calcium channel protein 1	0	0	-1
Tpd52	Q62393	Tumor protein D52	0	1	0
Tpi1	P17751	Triosephosphate isomerase	0	1	0
Tpmt	O55060	Thiopurine S-methyltransferase	0	0	-1
Trem2	Q99NH8	Triggering receptor expressed on myeloid cells 2	0	1	0
Trim3	Q9R1R2	Tripartite motif-containing protein 3	0	0	-1
Trim47	Q8C0E3	Tripartite motif-containing protein 47	0	0	-1
Trim65	Q8BFW4	Tripartite motif-containing protein 65	0	0	-1

			MARPs (up: +1; down: -1)		
Gene Name	**UniProt Accession**	**Protein Name**	**Early MARP**	**Middle MARP**	**Advanced MARP**
Trio	Q0KL02	Triple functional domain protein	0	0	-1
Triobp	Q99KW3	TRIO and F-actin-binding protein	0	1	0
Trp53i11	Q4QQM4	Tumor protein p53-inducible protein 11	0	-1	0
Tsc22d1	P62500	TSC22 domain family protein 1	0	0	1
Ttc38	A3KMP2	Tetratricopeptide repeat protein 38	0	0	-1
Ttc39b	Q8BYY4	Tetratricopeptide repeat protein 39B	0	0	1
Ttyh1	Q9D3A9	Protein tweety homolog 1	0	0	1
Tubb5	P99024	Tubulin beta-5 chain	0	0	-1
Ube2d1	P61080	Ubiquitin-conjugating enzyme E2 D1	0	0	-1
Ubl4a	P21126	Ubiquitin-like protein 4A	0	0	1
Upk1b	Q9Z2C6	Uroplakin-1b	0	-1	0
Usp24	B1AY13	Ubiquitin carboxyl-terminal hydrolase 24	0	0	-1
Vamp4	O70480	Vesicle-associated membrane protein 4	0	0	1
Vasp	P70460	Vasodilator-stimulated phosphoprotein	0	0	-1
Vat1	Q62465	Synaptic vesicle membrane protein VAT-1 homolog	0	0	1
Vav2	Q60992	Guanine nucleotide exchange factor VAV2	0	0	-1
Vim	P20152	Vimentin	0	0	1
Vps13c	Q8BX70	Vacuolar protein sorting-associated protein 13C	0	1	0
Vrk1	Q80X41	Serine/threonine-protein kinase VRK1	0	-1	0
Vtn	P29788	Vitronectin	0	1	0
Was	P70315	Wiskott-Aldrich syndrome protein homolog	0	0	-1
Wasf2	Q8BH43	Wiskott-Aldrich syndrome protein family member 2	0	0	-1
Wdfy2	Q8BUB4	WD repeat and FYVE domain-containing protein 2	0	0	-1
Wdr37	Q8CBE3	WD repeat-containing protein 37	0	-1	0
Wls	Q6DID7	Protein wntless homolog	0	0	1
Wnk1	P83741	Serine/threonine-protein kinase WNK1	0	0	-1
Xdh	Q00519	Xanthine dehydrogenase/oxidase	0	0	1
Xpo5	Q924C1	Exportin-5	0	0	1
Yes1	Q04736	Tyrosine-protein kinase Yes	0	0	-1
Yif1a	Q91XB7	Protein YIF1A	0	0	1

			MARPs (up: +1; down: -1)		
Gene Name	**UniProt Accession**	**Protein Name**	**Early MARP**	**Middle MARP**	**Advanced MARP**
Yipf3	Q3UDR8	Protein YIPF3	1	0	0
Zadh2	Q8BGC4	Prostaglandin reductase-3	1	0	0
Zfpl1	Q9DB43	Zinc finger protein-like 1	0	0	1
Znf335	A2A5K6	Zinc finger protein 335	0	0	1
Znf652	Q5DU09	Zinc finger protein 652	0	0	-1
Znf691	Q3TDE8	Zinc finger protein 691	0	0	-1
Zyx	Q62523	Zyxin	0	0	-1
	Q91V76	Ester hydrolase C11orf54 homolog	0	0	-1
	Q9CRC3	UPF0235 protein C15orf40 homolog	0	0	-1
	Q99K99	Uncharacterized protein C4orf19 homolog	0	0	-1
	P01864	Ig gamma-2A chain C region secreted form	0	-1	0
	Q9CXL3	Uncharacterized protein C7orf50 homolog	1	0	0

Suppl. Table 5: Relative quantification of proteins from seven AD risk genes in APPPS1 (**A**) or APP-KI (**B**) *versus* WT microglia. The protein LFQ ratios and p-values of AD risk genes are presented. P-values less than 0.05 are indicated in red.

A

	Ratio APPPS1 vs WT				p-value APPPS1 vs WT			
Gene Name	**1 month**	**3 months**	**6 months**	**12 months**	**1 month**	**3 months**	**6 months**	**12 months**
APOE	1.01	2.44	4.20	9.25	8.59E-01	2.45E-02	4.47E-03	4.37E-05
TREM2	0.94	1.40	2.20	2.88	1.50E-01	1.09E-02	4.82E-03	7.36E-06
CLU	1.15	0.97	1.07	1.87	5.70E-03	6.81E-01	6.36E-01	1.11E-03
INPP5D	1.10	1.38	1.80	1.71	2.66E-02	4.91E-04	2.86E-03	9.29E-05
PLCG2	0.99	1.05	0.99	0.86	7.01E-01	2.27E-01	8.45E-01	1.39E-01
ABI3	1.00	1.05	0.90	0.52	9.56E-01	4.72E-01	4.39E-01	1.44E-03
BIN1	0.95	1.03	0.74	0.40	3.93E-01	7.08E-01	7.62E-02	2.85E-04

B

	Ratio APP-KI vs WT				p-value APP-KI vs WT			
Gene Name	**1 month**	**3 months**	**6 months**	**12 months**	**1 month**	**3 months**	**6 months**	**12 months**
APOE	1.06	1.22	2.88	15.03	3.29E-01	3.04E-02	7.66E-04	3.09E-05
TREM2	0.99	1.12	1.44	3.85	9.16E-01	5.55E-01	6.38E-03	6.40E-04
CLU	0.84	1.10	0.76	0.72	2.84E-01	3.95E-01	1.80E-01	8.13E-02
INPP5D	0.94	1.08	1.26	1.34	1.68E-01	4.30E-01	2.43E-02	5.14E-05
PLCG2	0.97	0.99	0.74	0.66	2.33E-01	9.27E-01	1.31E-01	1.12E-02
ABI3	0.95	0.95	0.67	0.53	6.55E-01	6.83E-01	1.08E-02	1.78E-03
BIN1	0.99	0.97	0.72	0.59	7.39E-01	7.90E-01	5.49E-03	1.05E-03